POLITECNICO
MILANO 1863

SCUOLA DI INGEGNERIA INDUSTRIALE
E DELL'INFORMAZIONE

Control of panel stiffness through inflatable elements

Tesi di Laurea Magistrale in
Aeronautical Engineering - Ingegneria Aeronautica

Author: **Jacopo Lissoni**

Student ID: 245503
Advisor: Prof. Chiara Bisagni
Co-advisors: Prof. Antonio Raimondo
Academic Year: 2024-2025

Abstract

Inflatable structures provide a lightweight and easy solution in several applications, due to their ability to gain stiffness when inflated. These structures function by using internal pressure to tension a flexible membrane, transforming a compact material into a rigid, load-bearing shape. In this thesis, first, an inflatable tube is modeled and finite element analyses are conducted to investigate the response to bending and compressive loads. Inflatable tubes are then implemented as reinforcing elements in a composite panel and an investigation on its load response is conducted. The panel is reinforced by either one or three inflatable tubes, arranged in horizontal or diagonal configurations, and is subjected to compression and shear loading. Overall, the inflatable tubes improve the stiffness of the panel. The results show that, for a panel reinforced with three tubes and compressed along the tubes direction, the load bearing capabilities increase up to 60.9% at 0.20 MPa inflation pressure; in shear analyses, the inflatable elements provide improvements up to 57.1%. Additional analyses investigate the effect of regulating the pressure during the loading process or when the panel is in a pre-loaded state. In both cases, varying the inflation pressure of the tubes can successfully control the stiffness of the panel. Furthermore, an example of implementation of inflatable elements as actuator an adaptive flap is presented. The actuator, consisting of a composite panel reinforced by three inflatable tubes, is compressed on the trailing edge by pre-strained rubber flap surfaces. When the inflatable tubes are pressurized, they introduce an additional compressive force on the panel that initiates the buckling of the actuator, rotating the flap. The pre-strain of the flap surfaces is found using a semi-analytical model, developed around the equilibrium equations on the trailing edge when the flap is totally deployed and totally retracted. A numerical analysis on the deployment of the adaptive flap is conducted and a 9.95° trailing edge angle variation is obtained with an inflation pressure of 0.50 MPa.

Keywords: inflatable tubes, panel buckling, morphing actuator

Abstract in lingua italiana

Le strutture gonfiabili offrono una soluzione leggera e facile da implementare in diverse applicazioni, grazie alla loro capacità di acquisire rigidezza quando gonfiate. Queste strutture funzionano utilizzando la pressione interna per tendere una membrana flessibile, trasformando un materiale compatto in una forma rigida e portante. In questa tesi, inizialmente, un tubo gonfiabile viene modellato e vengono condotte analisi agli elementi finiti per studiarne la risposta a carichi di flessione e compressione. I tubi gonfiabili vengono quindi implementati come elementi di rinforzo in un pannello in composito e viene studiata la sua risposta al carico. Il pannello è rinforzato da uno o tre tubi gonfiabili, disposti in configurazioni orizzontali o diagonali, ed è sottoposto a carichi di compressione e taglio. Nel complesso, i tubi gonfiabili aumentano la rigidezza del pannello. I risultati mostrano che, per un pannello rinforzato con tre tubi e compresso lungo la direzione dei tubi, il carico massimo aumenta fino al 60.9% con una pressione interna di 0.20 MPa; nelle analisi di taglio, gli elementi gonfiabili forniscono miglioramenti fino al 57.1%. Ulteriori analisi indagano l'effetto della regolazione di pressione durante il processo di carico o quando il pannello è in stato di precarico. In entrambi i casi, la variazione della pressione interna dei tubi può controllare la rigidezza del pannello. Inoltre, viene riportato un esempio di implementazione di elementi gonfiabili in un attuatore per dispiegare un flap flessibile. L'attuatore, costituito da un pannello composito rinforzato da tre tubi gonfiabili, viene compresso sul bordo d'uscita dalle superfici in gomma pre-deformate del flap. Quando i tubi gonfiabili vengono pressurizzati, introducono una forza di compressione aggiuntiva sul pannello che innesca il buckling dell'attuatore, dispiegando il flap. La pre-deformazione delle superfici del flap viene calcolata utilizzando un modello semi-analitico, sviluppato attorno alle equazioni di equilibrio sul bordo d'uscita quando il flap è completamente dispiegato e completamente retratto. Infine, un'analisi ad elementi finiti è condotta per studiare il dispiegamento del flap e mostra una variazione dell'angolo del bordo d'uscita di 9.95°, con una pressione di gonfiaggio di 0.50 MPa.

Parole chiave: tubi gonfiabili, buckling pannello, attuatore morphing

Contents

1 | State of the Art

From the early stages of aviation to the present day, lightness has always covered an essential role in aircraft design. Nowadays, the effort towards reducing weight is extremely relevant, not only due to the financial benefits it brings, but also in the perspective of sustainability and environmental consciousness. The pursuit of lightness was the cause of many technological advancements that made possible the design and production of lighter and more efficient aircraft. One of the main topics that is still discussed today is adaptive wings. In the last two decades, the use of compliant mechanisms and smart material actuators in adaptive wing technologies has been thoroughly investigated, and the weight and aerodynamic benefits of these solutions became evident. However, they are not without their downsides, and new, alternative solutions, like inflatable devices and post-buckled panels, are one of the subjects of investigation.

1.1. Morphing: an Overview

Due to the ever-changing flight conditions an aircraft has to endure, the implementation of morphing mechanisms to increase aerodynamic performance is a pivotal part of wing design. In a broad sense, morphing refers to all those mechanisms that modify the geometry of the wing to adapt to different flight conditions. The improvement of aerodynamic efficiency provided by morphing structures comes at the cost of weight and fuel penalties, introduced by control systems and actuation devices. However, if reasonably sized[1], morphing configurations are utterly beneficial in terms of fuel consumption [1].

The concept of morphing is as old as aviation. On the very first aircraft, the Wright Flyer (1903), roll control was provided by wing twist [2]. In order to facilitate takeoff and landing phases, lift enhancement devices were introduced as early as in the 1920s [3]. Such mechanisms, like flaps and slats, gained over time in performance and complexity, and are still used today on the vast majority of aircrafts. After World War II, as aviation began to break into the supersonic realm, the concept of variable-sweep wings became

[1]The overall aerodynamic benefits are cancelled out by the weight and fuel penalties if the morphing wing configuration is too heavy or too energy demanding.

subject of investigation. Morphing wings able to control the sweep angle could reduce wave drag during supersonic cruise while guaranteeing maneuverability at low speed and facilitating takeoff and landing phases [4]. Variable-sweep wings are mainly employed for military applications; some notorious examples are the General Dynamics F-111 (1967), Grumman F-14 Tomcat (1974) and Rockwell B-1 Lancer (1985), shown in Figure 1.1.

Figure 1.1: Rockwell B-1 Lancer [5].

Historically, morphing devices relied on discrete surfaces driven by mechanical actuation [2]. This design provides the stiffness required to sustain all ranges of aerodynamic loads, but introduces a weight penalty caused by complementary components, like servo actuators, mechanical interfaces, linkages and rods. Conventional mechanisms can also suffer from load transmission issues, as part of the energy introduced in the system is lost due to friction at the interfaces and deformation of the supports [6].

Research on lighter morphing solutions is still ongoing and is spacing through several technologies [7]. Smart materials, like Shape Memory Alloys (SMAs) and piezoelectrics, are the main alternatives to conventional servo actuators [8]. Flexible skins can be used to control the flow over the airfoil in order to delay boundary layer separation at low Reynolds numbers, thus improving aerodynamic performance [9]. Yokozeki and Sugiura [10] obtained an improvement on lift coefficient curves by implementing corrugated structures in an adaptive aileron design. Corrugated structures were also employed in a later study, conducted by Henry et al. [11], aimed at finding the optimal distribution of piezoelectric actuators that maximized rolling and dive performances. De Gasperi [12] proposed the design of a morphing aileron mounted on a 24-meter fixed wing, based on the optimization of the actuation energy and compliant to structural and aerodynamic constraints. The presented design proved to be lighter, more energy efficient, and more aerodynamically efficient than the hinged counterpart. Another adaptive aileron design, presented by Li et al. [13], employed a honeycomb filling actuated by SMA wires to deflect the trailing edge downwards.

Of the several solutions presented in the last decades [2, 7, 8] almost all of them are employed in small, light vehicles. As adaptive wing structures rely on large deformations, compliance is obtained at the expense of stiffness. This trade-off is acceptable in smaller aircraft, like Unmanned Aerial Vehicles (UAV) and Micro Air Vehicles (MAV), where the aerodynamic loads are usually contained, but becomes problematic as the wing structure grows in size and complexity. Scalability, which is directly connected to the difficulty in balancing compliance and stiffness, is still an open issue in adaptive wings research [6]. For this reason, alternative solutions able to maintain stiffness while experiencing large deformations are being investigated, and among others, inflatable structures and post-buckled panels.

1.2. Inflatable Structures: Behavior and Applications

From a hiker in need of a lightweight, packable and comfortable camping mattress, to satellites requiring easy to deploy, low storage volume antennas, inflatable structures provide the answer to an extremely wide range of demands. Inflatable structures can consist of two thin layers of textile material sealed together, tubes or pouches that, when filled with pressurized gas, inflate into a predetermined shape. Due to their intrinsic qualities, such types of structures are not only widely common in several aspects of everyday life (tires, bouncy castles, inflatable boats, life jackets, air mattresses, etc...), but are also extremely appealing to engineering applications. Extensive research was conducted on the behavior of inflatable beams. Several papers were released investigating the topic [14–16], focusing on two issues specifically: how deflection is affected by pressure and wrinkling loads.

Due to the non-linearity of the problem, predicting the overall behavior of inflatable beams subjected to bending loads is complicated; however, the relation between pressure and maximum deflection can be oversimplified by stating that they are inversely proportional [14]. In other words, stiffness increases as pressure does. Wielgosz et al. [17] investigated the behavior of inflatable beams at medium pressure (up to 4 bars) and found promising results, as the beams were able to carry hundreds of times their own weight. Subsequent research at higher pressures highlighted the importance of employing high strength materials in order to improve the performance of inflatable beams [14]. Materials like elastomers offer good strength, low gas permeability and good elasticity, while maintaining a relatively low density. Polyurethane Rubbers (PU) offer the best properties for aeronautical implementation, being able to withstand a wide temperature range, -65°C to 220°C, and having the highest tensile strength out of all the elastomers, up to 40 MPa; all while maintaining a low density, 1.0 to 1.4 g/cc [18].

The second issue is wrinkling, a limit state caused by the inability of textile materials to carry compressive loads. When compressive axial stress (caused by bending or compressive loads) overcomes the tension produced by the pressurization, local buckling appears and the overall beam performance starts dropping. It is relevant to state that, although the appearance of the first wrinkle defines the limit load, the pneumatic collapse[2] of the structure happens only when half of the section is affected by wrinkling [19]. It was proven analytically that the wrinkling loads are dependent only on the geometry of the beam and on the pressure [14]. Since the appearance of wrinkling is delayed as the internal pressure increases, the advantages of implementing high strength materials for high-pressure beams become even more apparent. Figure 1.2 is taken from the 2016 study conducted by Thomas and Bloch [19] on the limit states of inflatable beams. The figure shows the pneumatic collapse of an inflatable beam subject to a three-point bending test. In the third image a wrinkle appears because the fabric lost tensioning due to the compressive force introduced by the bending load. As the beam is further loaded, the wrinkle grows in size and eventually the beam collapses.

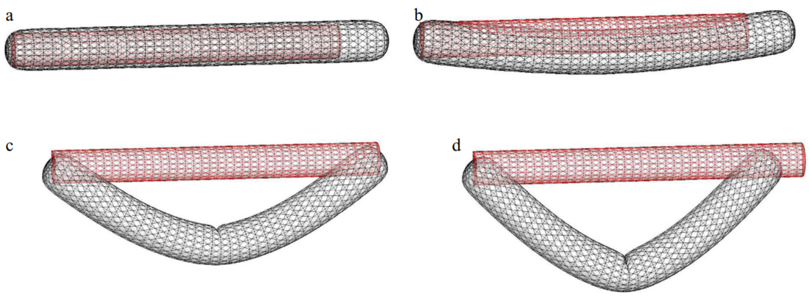

Figure 1.2: Pneumatic collapse in bending test [19].

Due to the novelty of the topic introduced, validation between analytical, numerical and experimental results was required. The correlation between numerical and theoretical results was verified by Le van and Wielgosz [16]. After developing a linearized analytical

[2]Since the terminology for collapse refers to an irreversible failure, the term "pneumatic collapse" is introduced to take into account the reversible behavior of inflatable beams after collapse due to wrinkling [19].

model for a cantilever inflatable beam, it was proven that finite element computations could provide accurate results with, at most, a 2.2% and 1.0% discrepancy for bending and buckling loads, respectively. Three and four-point bending tests were carried out in 2008 by Malm et al. [20] and were later compared with three dimensional finite element models constructed with membrane elements. The results were in agreement, and it was proven that FE codes could accurately reproduce the behavior of inflated structures, including the effects of wrinkling.

As briefly introduced before, inflatable structures are widely employed for various purposes. In space applications, inflatable structures are found in the design of antennas, habitable modules and decelerators, due to their portability, lightness and fast deployment [21]. Antennas are one of the most common device in which inflatable structures are used; the first implementation trace back to 1960 with the Echo 1 Mission [22], as a way to minimize weight due to the lack of powerful launchers. Since the gain in transmitting and receiving signals is proportional to the size of the antenna, inflatable structures are essential to pack large antennas while maintaining low weights and compact volumes. Research on this topic has gone as far as presenting solutions for CubeSats [23], where an antenna with a 1-meter diameter could be deployed from a 10 cm $\times$ 10 cm $\times$ 30 cm satellite. The structure of the antenna is composed of inflatable tubes and gains stiffness from the internal pressurization. An example of an antenna with inflatable structure is shown in Figure 1.3.

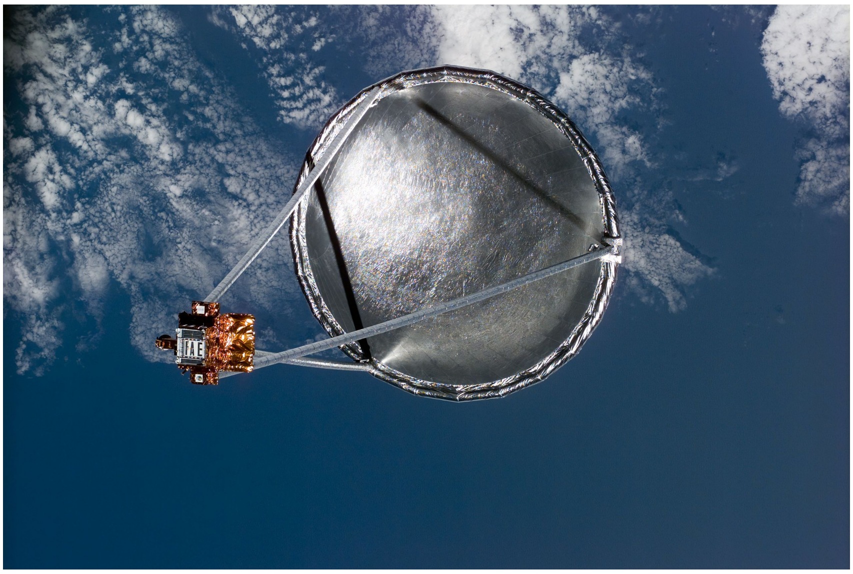

Figure 1.3: Inflatable Antenna [24].

In civil engineering, inflatable structures, which are usually referred to as pneumatic tensioned membrane structures, are often used for temporary housing, shelters, pavilions or military barracks. In these solutions, often employed in situations where quick assembly is required, the inflatable structure acts as the frame and directly sustains all the loads. New hybrid solutions have been investigated in the civil field. Xu et al. [25] studied the compressive behavior of a pressurized steel column. The study aimed at increasing the critical buckling load of a thin-walled column by inserting a pressurized air pouch in the internal cavity. The specimen consisted of a thin-walled steel pipe with a rubber bladder inside; the structure was placed vertically and tested under axial compression loads. The main effect of internal pressurization was to reduce the influence of the imperfections of the thin-walled cylindrical shell on the critical buckling load. Furthermore, a parametric analysis was presented in order to determine the optimal inflation pressure: in fact, in this type of structure, having too high of a pressure can induce Elephant's foot buckling [26]. This buckling form appears when the horizontal stress from the internal pressurization causes local bending that can initiate a buckling failure. In the end, the results of the tests on the pressurized column were positive and the critical buckling load was raised by more than twice that of the hollow specimen.

Although research on inflatable structures for aeronautical applications is still at an early stage, promising solutions have already been presented. Significant results in the employment of inflatable air pouches as means of actuation were reported by Vos and Barrett [27] in 2010. The mechanism was composed by an honeycomb whose cells are filled with air pouches. The air pouches can be inflated, thus expanding inside the cells and changing the shape of the honeycomb itself. The pressurization of the air pouches also increased the stiffness of the honeycomb. This mechanism was implemented in an adaptive flap connected to a makeshift wing; the expansion of the honeycomb due to the pressurization deformed the flexible skin of the adaptive flap, obtaining a 25-degree trailing edge angle variation with a cell differential pressure of 40 kPa. Figure 1.4 shows the activation and deactivion of the adaptive flap.

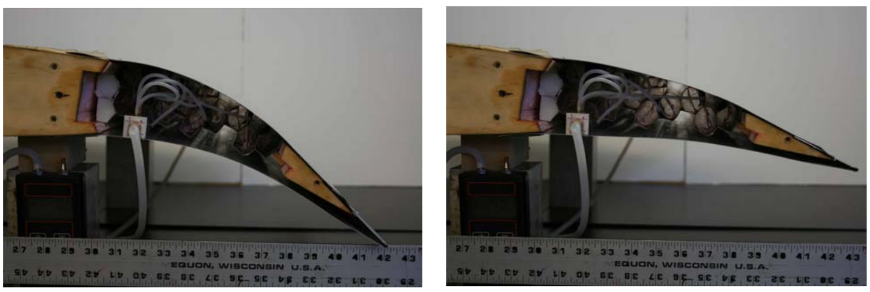

(a) 0.40 MPa (b) 0.0 MPa

Figure 1.4: Activation and deactivation of the adaptive honeycomb flap [27].

The pressure adaptive honeycomb could be used in two ways, either as an active or passive control system. The former would connect the mechanism to a pneumatic system and therefore act as an active control system, where the trailing edge angle is directly proportional to the pressure in the pouches. The latter is obtained by inflating the pouches and then sealing them; the deformation of the honeycomb would be dependent on the pressure differential between the inside and the outside of the pouches and, consequentially, on the altitude. The aileron would then provide higher lift when at lower altitudes, in conjunction with take-off and landing phases, while it would reduce the trailing edge angle at higher altitudes, during cruise for example.

A new development in the research of inflatable structure was introduced by Cremaschi [28] who presented an analytical formulation and numerical analysis of a pressurized air pouch, aiming at inserting it in a sandwich panel to increase structural properties. The air pouch was modeled as an independent material and the traction and buckling behavior were studied. Overall, stiffness and critical buckling load increased with the internal pressure. This thesis also laid the foundation for future implementation of pressurized panels in morphing mechanisms: buckling could be induced and controlled by varying the internal pressure, and the panel would effectively function as an active control device.

1.3. Post-Buckling: Behavior and Control

Due to their ability to obtain large out-of-plane deformation, while still being able to maintain stiffness and load-bearing capabilities, post-buckled plates became the subject of various investigations, either to enhance the performances of smart material actuators or as a means of actuation themselves.

Buckling is an instability phenomenon that produces large, sudden deformation of a structural component. Buckling is not destructive per se, as the component can maintain its load-bearing capability after snapping to the new deformed state; however, the post-buckled configuration is highly non-linear and directly affects the internal load distribution, leading to local stress build-ups. If the material is not able to withstand the stress accumulation, then failure occurs.

Post-buckling behavior can be difficult to predict in complex structures, but analytical formulations are available for simpler elements. Consider, for example, a simply supported panel under unidirectional axial compressive load. The panel width is W, the length is L and the thickness is t. The x direction is aligned with the panel length, the y direction with the width. The number of half-waves of the buckling mode in the y direction is m and A is the amplitude of the buckle. On the panel is applied a compressive distributed line force $\hat{N}_x$ in direction x. If the material is linear, elastic and isotropic and its Young's modulus is E, the internal axial load distribution $N_x(y)$ along the width in the post-buckled configuration is described by the following equation [29]:

$$N_x(y) = A^2 \frac{Et}{32} \left(\frac{W}{Lm}\right)^2 \left(\frac{2m\pi}{W}\right)^2 \left(-\cos\left(\frac{2m\pi y}{W}\right)\right) + \hat{N}_x \tag{1.1}$$

The sinusoidal distribution causes an internal load accumulation towards the edges, while the buckled portion of the plate becomes progressively discharged from loads. This disparity keeps increasing with the external load, until material limits are reached and failure occurs. For more complicated structures, analytical models become difficult to formulate and post-buckling analysis must rely on finite element models.

In the context of aeronautical structures, stiffened panels can delay global instabilities, however local buckling can appear in between the stringers [30–32]. Local buckling may not cause the failure of the plate but can be detrimental to the overall structural integrity as the internal load redistribution leads to stress build-ups in riveted joints and stringers [33]. These side effects are generally accounted for and, with a few exceptions, tolerated in aircraft design. Figure 1.5 shows the appearance of skin buckling caused by shear loads on the fuselage of a B-52.

Figure 1.5: Skin buckling on the fuselage of a B-52 [34].

Controlling the post-buckling response of a plate was initially introduced as a solution to delay the instability rather than exploiting it. Thompson and Loughlan [35] implemented pre-strained SMA wires in a composite plate and were able to alleviate the effects of buckling by redistributing the internal axial loads uniformly along the plate width.

As the interest towards adaptive wings grew, post-buckling control began to be investigated as a form of actuation. Post-buckled precompressed (PBP) actuators exploit a compressive axial force acting on a plate onto which is laid a piezoelectric element. As a result, the bending deflection caused by the piezoelectric element is magnified by the applied force. Vos et al. [36] implemented a PBP actuator in the design of an adaptive flap. The mechanism was installed on an airfoil whose front portion was formed by a D-Beam, while the rear portion consisted of an adaptive flap made of flexible rubber skin The PBP actuator was constrained to the D-Beam and extended to the trailing edge, where it was connected to the upper and lower rubber skin of the rear portion of the airfoil. As the PBP actuator was activated, the trailing edge deflected downward. The PBP actuator proved to be not only lighter than its mechanical counterpart, but also more energy efficient and with higher control performances. The result was successful, however, it could be applied only to small UAVs, as the rubber skin could not sustain the load generated by larger wings.

Another way to exploit buckling to achieve actuation purposes is to use bistable panels. Bistable panels are plates that present two stable equilibrium configurations, which can be switched by applying a low activation force. Once in the new equilibrium state, the panel does not require any additional force to maintain its shape. The snap-through often causes large displacements in the plate; for this reason, bistable panels provide a valid actuation solution, especially for morphing applications. Daynes et al. [37] designed and tested a Bistable Flap, consisting of twenty bistable prestressed composite plates placed inside a trailing edge flap, shown in Figure 1.6. The snap-through between the two equilibrium states of the bistable plates was initiated by a high strength cord connected to an actuator. The two equilibrium configuration of the bistable panel corresponded to either a 0° or 10° trailing edge angle. The Bistable Flap was tested in a wind tunnel and provided a 0.2 increase in the lift coefficient when deflected, a quick activation time and an overall robust design.

A novel approach to post-buckling control was introduced by Bisagni and Zhang [38] by exploiting the built-in instability of panels in a wing box. As the wing box twists, shear loads are applied onto the panels; the buckling response can then be controlled by specially constraining the out-of-plane displacements. This solution has potential to be employed for morphing mechanisms' actuation.

1.4. Future Applications

Stiffened panels are one of the most common structures employed in aeronautical projects. The buckling behavior of a stiffened panel is highly dependent on the configuration, sec-

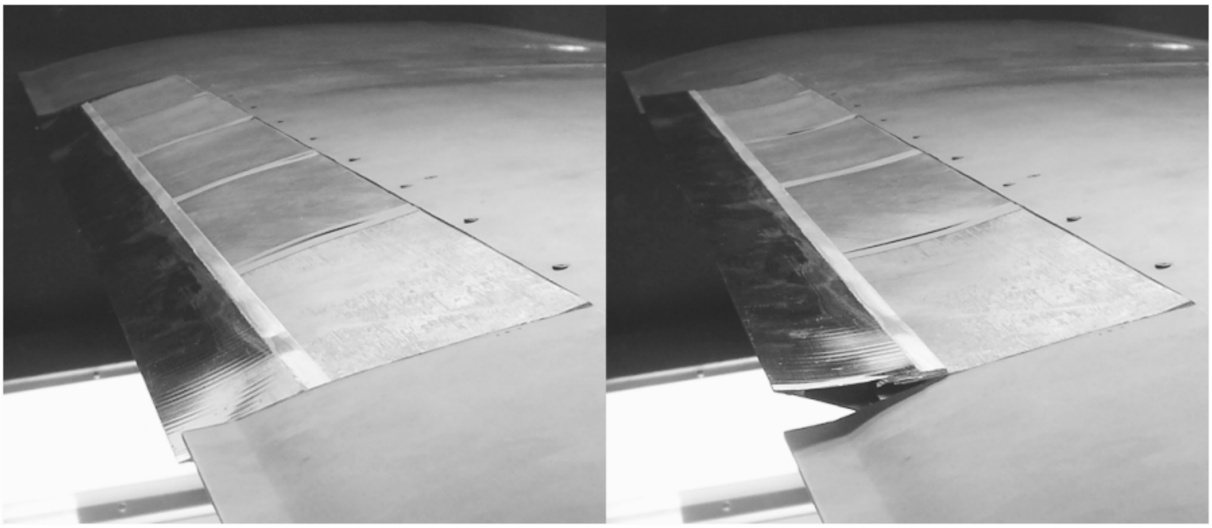

Figure 1.6: Bistable Flap [37].

tion shape and size of the stringers. The stiffness of the stringers plays a key role in the buckling behavior of a panel but is a fixed parameter, which cannot be actively modified during flight. Therefore, controlling the post-buckling behavior of the panel can only rely either on the applied load or on the boundary conditions. For this reason, actively controlling the stiffness of the stringers could introduce a new and reliable form of control for post-buckled panels. This approach would be impossible to implement with conventional stiffeners, but, as introduced in section 1.2, employing inflatable elements as panel reinforcements could be a solution to control the post-buckling behavior by specially varying the internal pressure. The possible configurations are numerous, and so is the nature of the inflatable elements employed, which can be beams but also pouches, as presented by M. Cremaschi [28]. This type of solution could be beneficial for two main reasons: firstly, stiffened panels are already part of the wing structure and employing them to control morphing mechanisms would remove the need for other types of actuators. Secondly, the pressurization of the inflatable elements would be carried out by the pneumatic system, which is already on board a large number of aircraft. For smaller aircraft, where a pneumatic system is not present, the same approach would work passively, adapting to the change of atmospheric pressure. For these reasons, the study of inflatable structures in post-buckled plates for morphing application is extremely relevant nowadays and the benefits they could bring are definitely worth an in-depth investigation.

2 | Inflatable Tube: Model and Verification

This chapter covers the modeling of the inflatable beam and validates its behavior by comparing it to previous studies. In the paper *Bending and buckling of inflatable beams: Some new theoretical results* [16] by Le Van and Wielgosz, the authors develop an analytical formulation for inflatable beams behavior, and compare the results with finite element analyses. In the paper, several beams of different length and radius are tested to bending and compression loads. The geometric and material properties are provided. Each test is carried out at four inflation pressures p_ϕ: 0.05 MPa, 0.10 MPa, 0.15 MPa, 0.20MPa. Although the original scope of the reference paper was the formulation of an inflatable beam analytical model, the authors provided a significant set of data that made it suitable for a validation study.

2.1. Inflatable Tube: Geometry and Material

The inflatable beam is modeled as a cylinder of length $l = 650$ mm and radius $r = 40$mm, as shown in Figure 2.1. The material properties, reported in Table 2.1, are provided by the reference paper and resemble that of an elastic rubber fabric. The thickness of the fabric is $h = 0.125$ mm.

Material properties	
Thickness, h	0.125 mm
Young Modulus, E	2500 MPa
Poisson's Ratio, ν	0.3
Density, ρ	1×10^{-6} kg/mm^3

Table 2.1: Material properties of the inflatable tube.

The reference paper investigates the behavior of the tube subjected to bending and com-

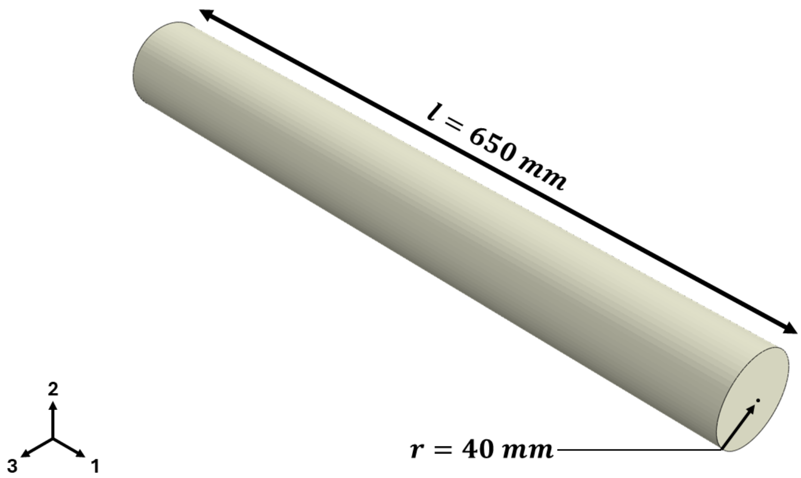

Figure 2.1: Geometry of the inflatable tube

pression loads. In the bending tests, the tube is fully constrained on one end and loaded with a 1 N shear force on the opposite end. The value of interest is the tip displacement of the free end. In the compressive tests, one end is still fully constrained while the other is loaded with a compressive force. The value of interest is the collapse load of the tube. Each test is conducted with the tubes inflated at four inflation pressures p_ϕ: 0.05 MPa, 0.10 MPa, 0.15 MPa, 0.20MPa.

2.2. Inflatable Tube: Analytical model

The equations obtained from the development of the analytical model[16] can be useful to understand the behavior of the tubes and their limit states.

The formulation employs a membrane material, meaning that it cannot sustain compressive load. The inflation process is therefore required to establish a pre-stressed state that can guarantee the stiffening of the beam. The hypothesis of membrane material is fundamental in defining the limit states of the inflatable beam.

Bending formulation

Consider an inflated cantilever beam of length l_ϕ, radius r_ϕ, cross section area S_ϕ and second moment of area I_ϕ. The values marked with the index ϕ refer to the inflated configuration and are therefore affected by the inflation pressure p_ϕ. The index ϕ refers to the inflated configuration, since the pressurization changes the geometry of the beam. The cantilever beam is fully constrained on one end, and a transversal force F is applied on the opposite end. The axial force generated by pressure is defined as:

$$P = p_\phi \cdot \pi r_\phi^2 \tag{2.1}$$

The material is considered isotropic and linear, the Young's modulus is E and the shear modulus is G. A shear correction factor k is considered. Figure 2.2 shows the load condition, the vertical displacement $V(x)$ and the cross section rotation $\theta(x)$. The deflection along the beam axis and the cross section rotation are reported in Equations 2.2 and 2.3:

$$V(x) = \frac{F}{(E + P/S_\phi)I_\phi}\left(\frac{l_\phi x^2}{2} - \frac{x^3}{6}\right) + \frac{Fx}{P + kGS_\phi} \tag{2.2}$$

$$\theta(x) = \frac{F}{(E + P/S_\phi)I_\phi}\left(l_\phi x - \frac{x^2}{2}\right) \tag{2.3}$$

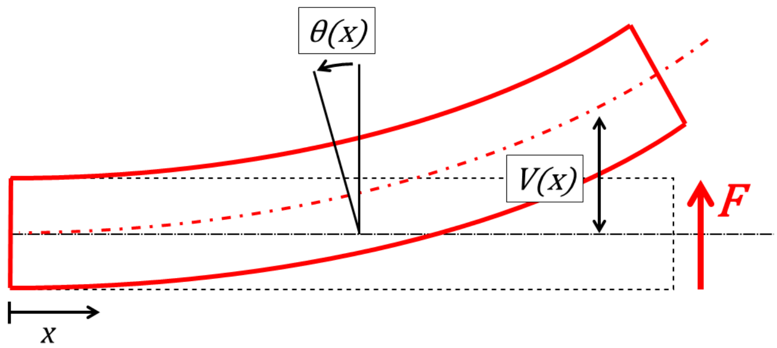

Figure 2.2: Bending deformation.

The influence of pressure is non-linear and affects geometric values as well. When the inflation pressure goes to 0, the beam formulation resembles Timoshenko's beam theory. However, due to the hypothesis of membrane material, the load bearing capabilities of the beam would be null when totally deflated. Due to the inability of membrane to carry compressive loads, a limit state is reached when negative axial stress appears. Therefore, stress must be positive everywhere. Since the contribution of bending to the stress distribution is the highest at the root of the beam, the condition that must be satisfied is reported in Equation 2.4:

$$F \leq \frac{\pi r_\phi^3 p_\phi}{2I_\phi} \tag{2.4}$$

When the condition is not satisfied, the bending force is high enough to counteract the tensioning of the membrane and wrinkling appears, thus making the formulation no longer valid.

Buckling formulation

Consider now the same beam presented in the previous section, but loaded in compression with a force F. Figure 2.3 shows the compressive load condition. When the critical buckling load is reached the tube folds on itself and collapses. The critical buckling load F_{cr} of the inflatable beam can be found by solving the differential equation reported in Equation 2.5:

$$\frac{d^2\theta}{dx^2} + \Omega^2\theta = 0 \tag{2.5}$$

where the quantity Ω^2 is:

$$\Omega^2 = \frac{F(P + kGS_\phi)}{(E + (P - F)/S_\phi)I_\phi(P - F + kGS_\phi)} \tag{2.6}$$

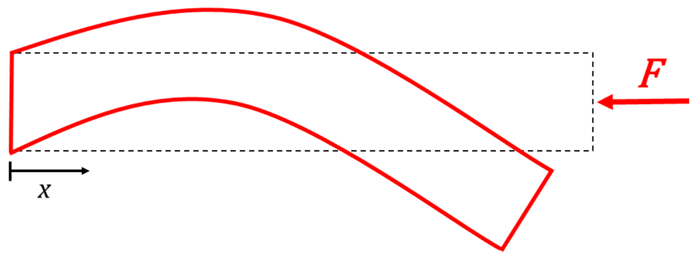

Figure 2.3: Bending deformation.

By numerically solving the equation for F, one root is finite and acceptable while the other tends towards infinity and should not be considered. In order for this solution to be valid, the applied force F must be lower than the axial force P provided by the pressurization. Otherwise, the applied force would overcome the tensioning of the beam and crush it. The condition that must be respected in order for the formulation to be valid is:

$$F < p_\phi \cdot \pi r_\phi^2 \tag{2.7}$$

2.3. Inflatable Tube: Finite element model

The finite elements analyses of the inflatable tube is conducted using ABAQUS. The tube is modeled using a mix of quadrilateral 4-node M4D3R and triangular 3-node M3D3 membrane elements, as shown in Figure 2.4. The mesh size l_e provides a ratio $\gamma = \frac{R}{l_e} = 10$, which is used to pick the mesh size of the tubes reinforcing the panels presented in Chapter

3.

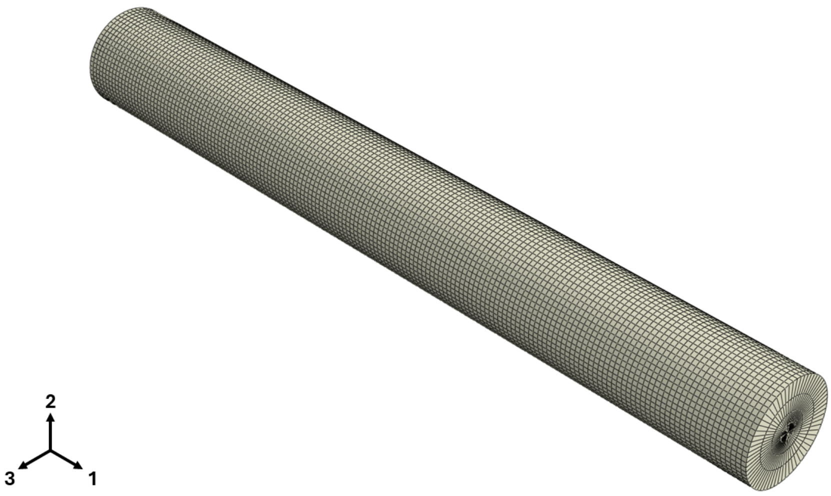

Figure 2.4: FE model of the study.

The central axis of the beam is aligned with Direction 1 of the reference system, while the section plane is defined by Direction 2 and Direction 3. The extremities of the beam are referred to as Extremity A and Extremity B. Each extremity of the tube is kinematically coupled to its own reference point, respectively named `RP-A` and `RP-B`. Therefore, each node of the extremity surfaces has the same displacements and rotations as the reference points. The extremities effectively act as rigid surfaces, as shown in Figure 2.5.

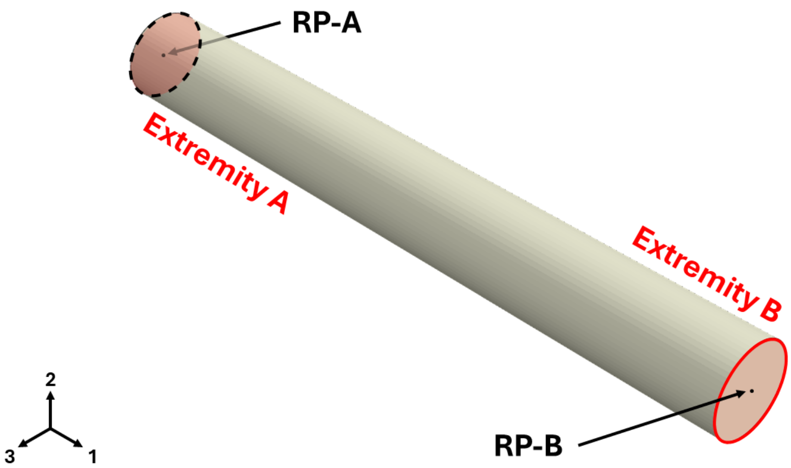

Figure 2.5: The extremities of the beam and the reference point to which are coupled.

The numerical computations employ Implicit Dynamic Quasi-Static analyses in order to

avoid any inertial effect.
The pressurization of the beam is simulated by the Fluid Cavity Interaction. The interaction requires a totally enclosed surface and a cavity reference node placed inside of it. The inflation pressure is the only degree of freedom of the reference node, which can be controlled to pressurize the cavity, thus allowing the modeling of fluid-filled structures [39]. The fluid used in the computation is air, and it is treated as a perfect gas. The molar mass used is $m_{mol} = 2.9 \times 10^{-5} \frac{t}{mol}$ and the Universal Gas Constant is $R = 8.314 \times 10^{3} \frac{mJ}{mol \cdot K}$.

Load and Boundary Conditions

Due to the coupling at the extremities, boundary conditions and loads can be applied just on the reference points and they are transferred to the entirety of the extremity surfaces. On `RP-A`, an encastre boundary condition is applied, thus constraining every degree of freedom of every node of Extremity A.

The analysis is divided into two steps in which the pressure and the load are applied. Figure 2.6 reports the pressure and load trends during the two steps.

- Step 1 - Inflation Step. In the first step the beam is inflated to the nominal pressure p_ϕ. There are four pressure levels of interest: 0.05 MPa, 0.10 MPa, 0.15 MPa and 0.20 MPa. During the inflation Extremity B is kept unconstrained. Due to the high flexibility of the material of the beam, the pressurization inevitably affects the geometry of the beam. In order to evaluate the correct behavior of the Fluid Cavity Interaction, the radius r_ϕ and length l_ϕ of the inflated beam are compared to the reference paper.

- Step 2 - Loading Step. In this step the beam is loaded with either a bending force or a compressive force. The load is applied gradually on `RP-B` and the internal pressure is kept constant.

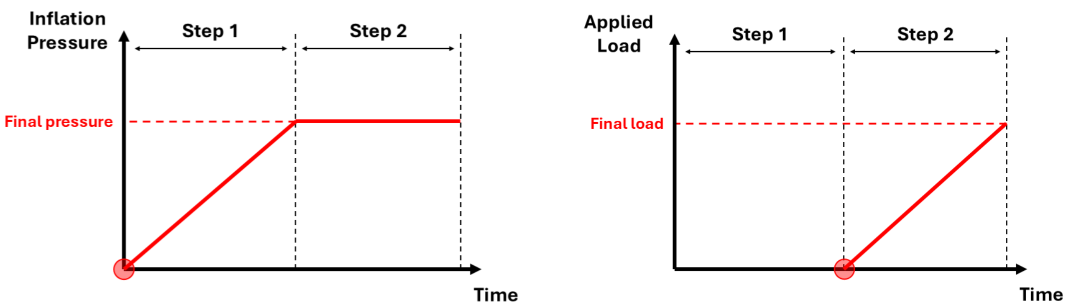

(a) Pressure trend (b) Applied load trend

Figure 2.6: Pressure and load application

The load cases presented in the reference paper, aimed at evaluating the bending and compressive response of the inflatable beam, are set up as follows:

- Bending: a transversal concentrated force $F_S = 1$ N is applied on `RP-B`, in Direction 2.
- Compression: an increasingly larger compressive force is applied on `RP-B` in Direction 1, until the beam itself collapses.

A graphic representation of the load application is shown in Figure 2.7.

(a) Bending Test

(b) Compression Test

Figure 2.7: Load application for bending and compression validation tests.

After the completion of the loading step, the output values of interest are the tip displacement for the bending test, and the collapse load for the compression test .

Convergence

A convergence study on both the bending and compressive cases is carried out to verify the correct behavior of the model with respect to its mesh size, and to choose an appropriate mesh size which provides negligible errors while maintaining relatively low computational times. The numerical computations are carried out on the beam model inflated at $p_\phi = 0.10$ MPa. The value of reference is the tip displacement for the bending test, and the collapse load for the compression test; these values are obtained from the model with a mesh size of $l_e = 1$ mm. The same analysis is repeated with larger mesh sizes; the error with respect to the values of reference and the computational time is evaluated.

As shown in Table 2.2, the computational time is higher for the compression analyses. The analyses are run on a system with 4 Intel Xeon Gold 6252N CPUs, each equipped with 24 cores and a total of 48 threads, and 1TB of RAM. Although such values, even for the finest mesh, are not high, a mesh size of $l_e = 4$ mm is chosen in the perspective

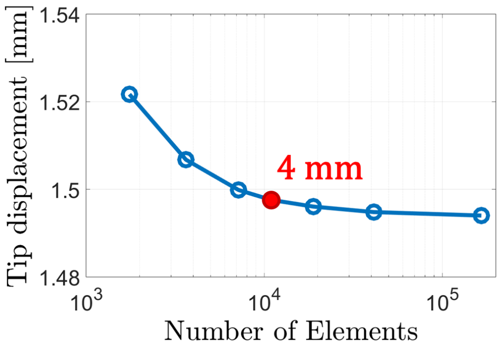

(a) Bending

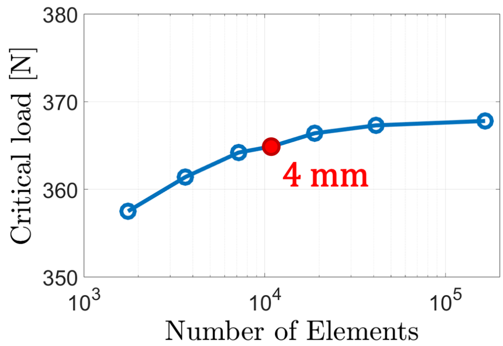

(b) Compression

Figure 2.8: Convergence trends.

of implementing the beam in more complex models. The trade-off however is minimal, since the error with respect to the finer $l_e = 1$ mm mesh is kept well below 1% while the duration of the analyses is reduced by more than 90%.

Element Size	Number of elements	Bending	Compression
1 mm	165816	1.99×10^3 s	7.01×10^3 s
2 mm	41292	4.96×10^2 s	1.85×10^3 s
3 mm	18900	2.06×10^2 s	8.90×10^2 s
4 mm	**10944**	**1.25×10^2 s**	**4.89×10^2 s**
5 mm	7176	73 s	3.53×10^2 s
7 mm	3636	41 s	1.95×10^2 s
10 mm	1752	20 s	1.01×10^2 s

Table 2.2: Computational times for convergence analyses.

2.4. Validation: Results

The results of the validation study are in good agreement with the reference values both in bending and compression. Some discrepancies can be noticed, however the reference paper lacked information regarding how boundary conditions and loads are applied on the model. The modeling of the beam's extremities was also not described in the reference paper. Table 2.3 and 2.4 respectively show the values of the radius r_ϕ and length l_ϕ after the inflation of the tube; the results are in good agreement with the reference [16]. The radius value is taken from the cross section halfway between the two extremities. The length value is obtained from the center node of Extremity B. The reference values are obtained from the reference paper [16].

Radius after inflation, r_ϕ			
Infl. pressure	**Analysis result**	**Reference value [16]**	**Error**
0.05 MPa	40.22 mm	40.22 mm	0.0%
0.10 MPa	40.44 mm	40.44 mm	0.0%
0.15 MPa	40.67 mm	40.65 mm	0.049%
0.20 MPa	40.91 mm	40.87 mm	0.098%

Table 2.3: Radius values after inflation.

Length after inflation, l_ϕ			
Infl. pressure	**Analysis result**	**Reference value [16]**	**Error**
0.05 MPa	650.8 mm	650.8 mm	0.0%
0.10 MPa	651.7 mm	651.7 mm	0.0%
0.15 MPa	652.5 mm	652.5 mm	0.0%
0.20 MPa	653.4 mm	653.3 mm	0.015%

Table 2.4: Length values after inflation.

Table 2.5 reports the tip displacement values and compares them with the reference values from the reference [16]. In the reference paper, the results of both the analytical formulation and finite element computations are presented. The values of tip displacement are taken from the node in the center of the free extremity.

Tip displacement, V_{tip}					
	Analysis Result	**Numerical[16]**		**Analytical [16]**	
Infl. pressure	**Value**	**Value**	**Error**	**Value**	**Error**
0.05 MPa	1.504 mm	1.487 mm	1.14%	1.481 mm	1.55%
0.10 MPa	1.497 mm	1.461 mm	2.46%	1.462 mm	2.39%
0.15 MPa	1.490 mm	1.436 mm	3.76%	1.443 mm	3.26%
0.20 MPa	1.482 mm	1.413 mm	4.88%	1.425 mm	4.00%

Table 2.5: Results of the bending analyses.

The magnitude of the tip displacement in the bending assessment is also aligned with the reference values, reporting errors not larger than 5%. The deformed shape, magnified by a factor 10, of the beam inflated at $p_\phi = 0.10$ MPa is reported in Figure 2.9.

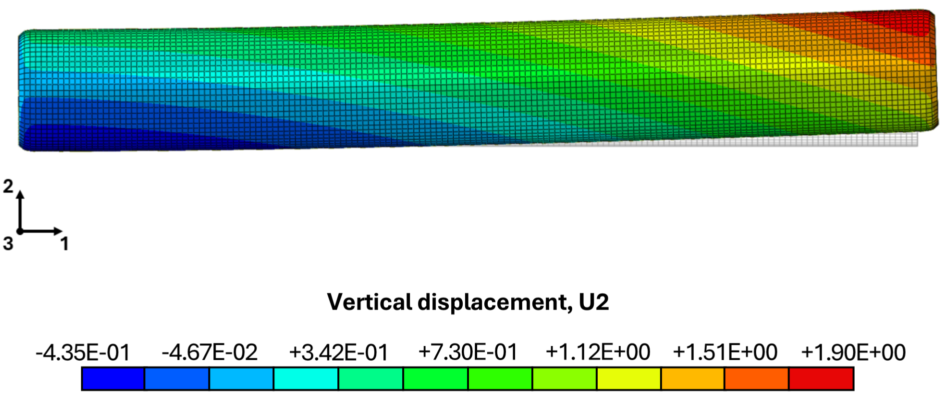

Figure 2.9: Bending shape at $p_\phi = 0.10$ MPa.

The compressive analyses were particularly useful to assess both pneumatic and buckling collapse. Pneumatic collapse is the failure caused by the loss of tensioning of the membrane, which happens when the compressive load counteracts the axial force generated by the pressure on the extremity surface. Amongst the cases investigated, pneumatic collapse happens only when the inflation pressure is $p_\phi = 0.05$ MPa, because the critical load is coherent with the limit state reported in Equation 2.7. As shown in Table 2.6, the differences are minimal and the results are in good agreement with the reference paper.

Critical compressive load, F_{cr}					
	Analysis Result	Numerical [16]		Analytical [16]	
Infl. pressure	**Value**	**Value**	**Error**	**Value**	**Error**
0.05 MPa	246.5 N	×	×	253.8 N	2.88%
0.10 MPa	364.9 N	366.9 N	0.55%	366.1 N	0.33%
0.15 MPa	372.1 N	372.0 N	0.02%	371.4 N	0.19%
0.20 MPa	376.9 N	377.3 N	0.11%	377.2 N	0.07%

Table 2.6: Results of the compression analyses.

Figure 2.10 shows the collapse sequence of the beam inflated at $p_\phi = 0.10$ MPa. The collapse is caused by buckling. When the compressive force approaches the critical load, the beam begins to bend without being affected by wrinkles as shown in Figure 2.10a. As the deformation increases, the upper surface of the beam is compressed further until the tensioning of the membrane is lost. Figure 2.10b of the sequence shows the development of local wrinkling, while in Figure 2.10c the beam has completely lost any structural capability. The wrinkling is caused by local stress build-ups caused by the large buckling deformations.

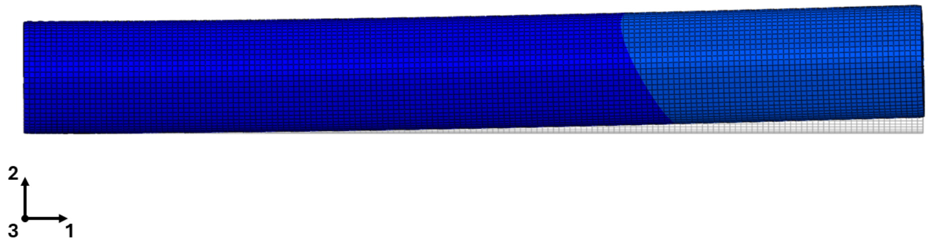

(a) $F_C = 364.3$ N

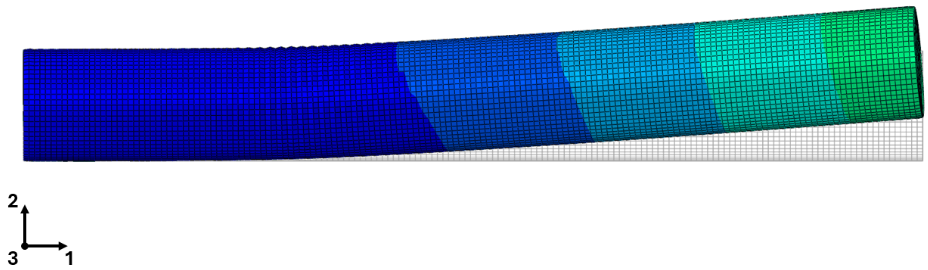

(b) $F_C = 364.8$ N

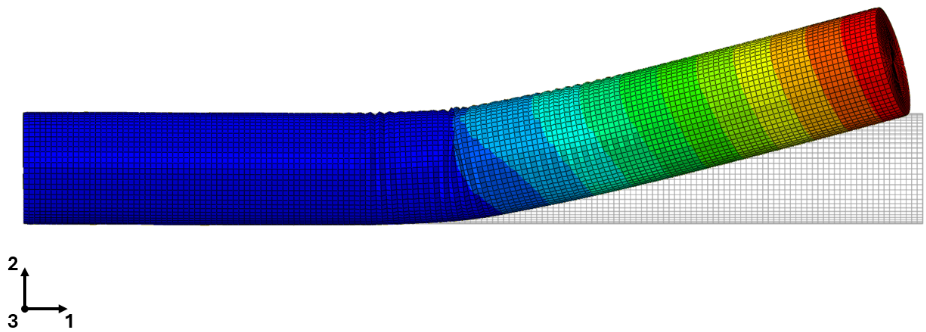

(c) $F_C = 364.9$ N

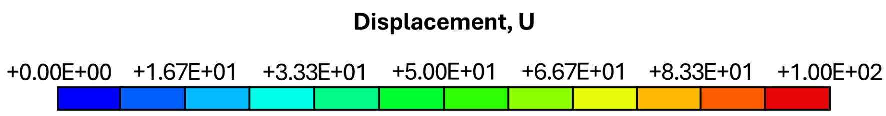

Figure 2.10: Collapse sequence at $p_\phi = 0.10$ MPa.

3 | Panel Stiffened with Inflatable Tubes: Modeling

The potential of inflatable beams as reinforcing elements in panels is now investigated. The possible configurations are several; however, due to the novelty of the topic and the necessity to show the basic behavior of such type of structures, this work is restricted to a small set of simple models. The main focus is to determine the relation between stiffness and inflation pressure, and how pressure influences the buckling load and shape of the panel.

In this chapter, the models of the panels used for the numerical analyses are thoroughly explained. The study takes into account two main variants of the panel, differing in the orientation of the inflatable reinforcing tubes. Each configuration is tested to different types of loading conditions and boundary conditions, in order to evaluate the complete and all-around behavior of the structure. Before presenting the configurations, the modeling of the two main features, the inflatable beam and the panel, is explained.

3.1. Design of a Panel Stiffened with Inflatable Tubes

The main structure studied in this work is a composite panel stiffened with cylindrical inflatable tubes. As stated previously, different configurations are presented. However, the model used for the inflatable beam and for the panel is same throughout every structure analyzed.

Panel Modeling

The panel is composed of four IM7-8552 composite plies, laid up in a $[0/90]_S$ pattern. The panel is square-shaped, its size is 440mm $\times$ 440 mm and each ply is $t_{ply} = 0.125$mm thick, bringing the total thickness up to t = 0.5 mm. The material properties are relative to a single ply of IM7-8552 unidirectional prepreg.

The mesh size of the panel is $l_e = 5$ mm and employs linear quadrilateral shell S4R elements. In order to facilitate the comprehension of the boundary conditions and loads, the edges of the panel are labeled from A to D, as shown in Figure 3.1. In the employed reference system, the panel is placed in the plane created by Direction 1 and Direction 2, while the out of plane direction is aligned with Direction 3.

Material properties	
Ply thickness, t_{ply}	0.125 mm
Ply Lay-up	$[0/90]_S$
E_{11}	161000 MPa
$E_{22} = E_{33}$	11400 MPa
$G_{12} = E_{13}$	5170 MPa
G_{23}	3980 MPa
$\nu_{12} = \nu_{13}$	0.32
ν_{23}	0.435
Density, ρ	1.25×10^{-6}kg/mm^3

Table 3.1: Material properties of the composite panel.

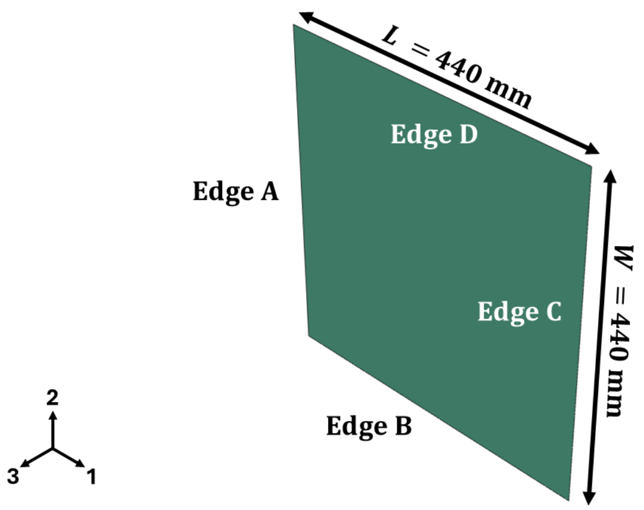

Figure 3.1: Sizing and nomenclature of the panel.

Tube Modeling

The modeling of the inflatable beam resembles almost entirely that used in the validation study explained in Section 2.3 with the exception of a few geometric parameters. The length of the tube varies, depending on the placing and orientation, between 311 mm, 440 mm and 622 mm; the radius is $r = 10$ mm and the thickness is set at $h = 1$ mm. The mesh size of the tube is $l_e = 1$ mm, which provides a mesh size to radius ratio of $\gamma = \frac{r}{l_e} = 10$, like in the validation study. This value proved to be accurate with respect to finer mesh sizes and its behavior was validated. The material properties do not change and are reported in Table 2.1.

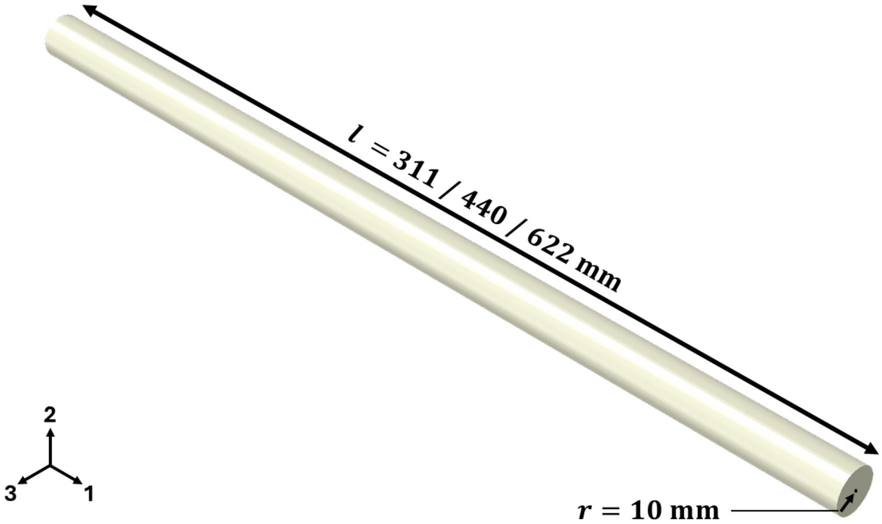

Figure 3.2: Inflatable tube geometry

Tube and panel Interactions

Panel and tubes are attached together with a TIE constraint; the panel is set as the master surface because of the coarser mesh, a single line of nodes on the tube is set as the slave surface. In order to avoid any penetration between the tubes and the panel, a contact interaction is defined as well. The beams are inflated using the Fluid Cavity Interaction. The inflation pressures p_ϕ of interest are 0.05 MPa, 0.10 MPa and 0.20 MPa. The pressure inside each tube can be controlled independently. The results are compared with the response of the panel without tubes.

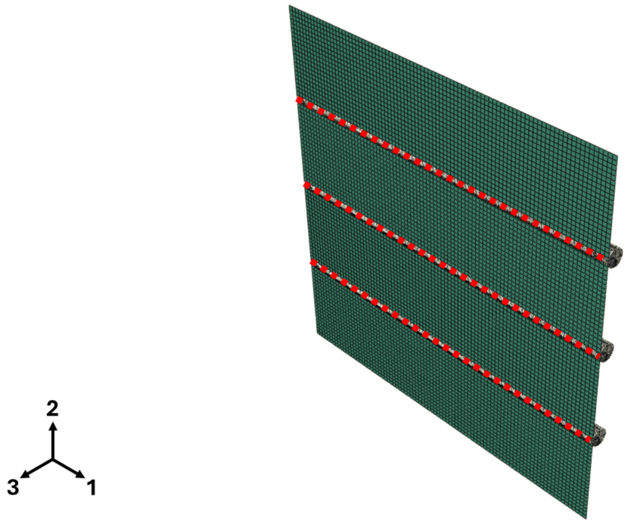

Figure 3.3: The lines of nodes subject to the TIE constraint are highlighted in red.

Stiffened panel: tubes configurations

Due to different models that are investigated, a systematic classification is needed. The configurations investigated in this study are firstly categorized by the number of inflatable reinforcing beams: each panel can be reinforced by either one or three tubes, and is respectively labeled as `1T` or `3T`.

Both possibilities are further categorized by the orientation of the reinforcing beams: the tubes are either aligned with Direction 1, placed perpendicularly with respect to Direction 1 or placed diagonally at a ±45° angle. Each configuration is referred to with the orientation angle value: `0`, `90`, `45` or `-45`. For example, the single-tube configuration with the tube aligned with Direction 1 is called `1T 0`.

The models used in the `1T 0`, `3T 0`, `1T 90` and `3T 90` configurations are shown in Figure 3.4. The `90` configurations are obtained from `0` model rotated by 90° around Direction 3. In the single-tube configuration, the beam is placed on the symmetry axis of the panel and spans through the whole width. In the three-tubes configuration, two additional and identical tubes are placed halfway between the edges and the central tube, distancing 110 mm from each other. The length of every tube in these cases is $l = 440$ mm.

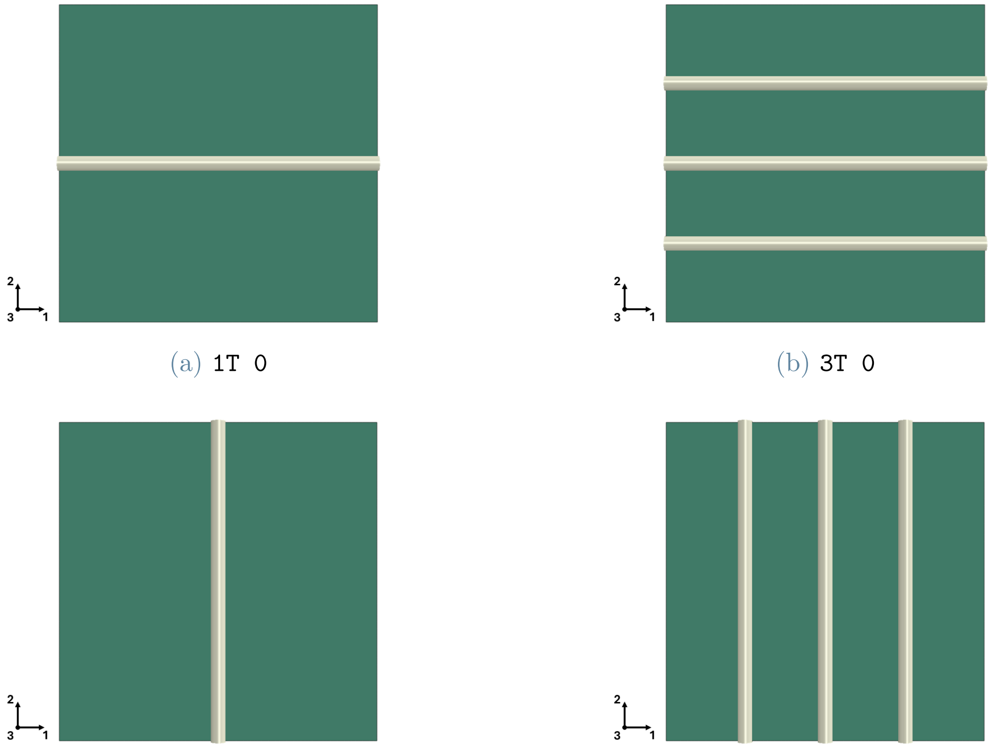

(a) `1T 0` (b) `3T 0` (c) `1T 90` (d) `3T 90`

Figure 3.4: Models used for `0` and `90` configurations.

The `1T 45`, `3T 45`, `1T -45` and `3T -45` configurations, shown in Figure 3.5, place the beam diagonally on the panel. The `-45` model is obtained from a 90° rotation around Direction 3 of the `45` model. In the `1T 45` and `1T -45` configurations the tube runs along the panel diagonal, while in the `3T 45` and `3T -45` configurations two additional shorter elements are placed halfway between the diagonal and the corners of the panel. The length of tubes in this case is different from the `3T 0` model: the shorter tubes are 311 mm long, while the middle tube is 622 mm long.

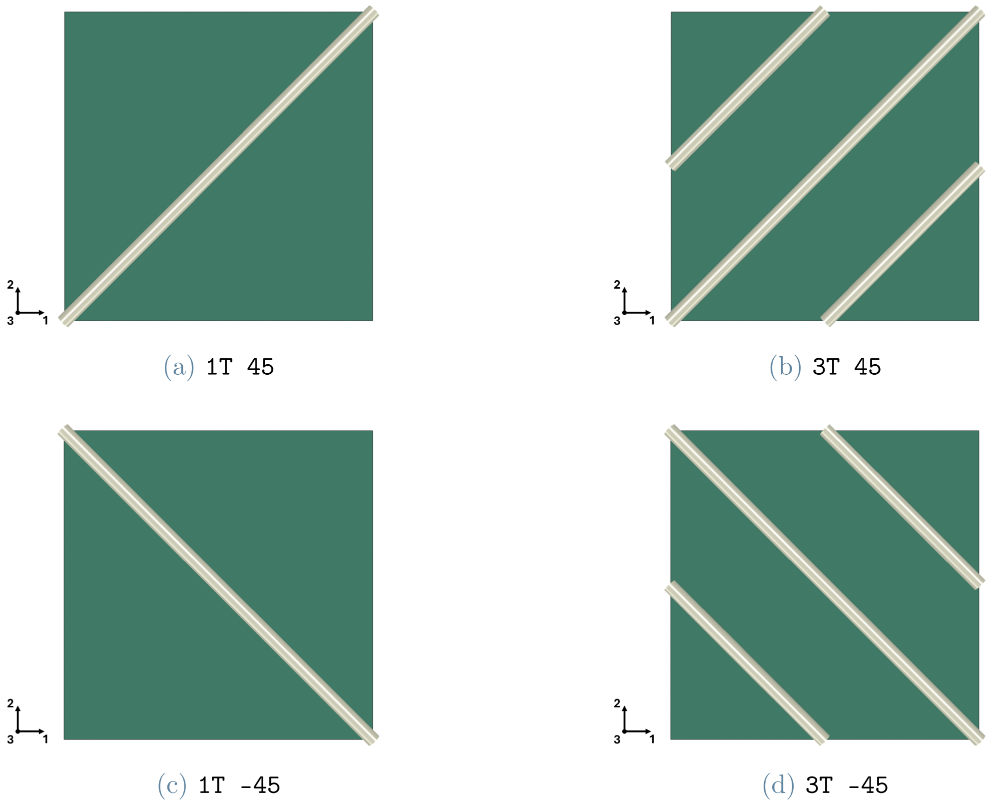

Figure 3.5: Models used for 45 and -45 configurations.

3.2. Load Cases and Boundary Conditions

The goal of the study is to evaluate the all-around behavior of each stiffened panel, therefore each configuration is analyzed to compression and shear loads. The computations employ Dynamic Implicit Quasi-Static analyses. Each analysis is divided into two main steps:

- Step 1 or **Inflation Step**. During this step the tube, or tubes, are inflated to the pre-determined pressure p_ϕ of 0.05 MPa, 0.10 MPa or 0.20 MPa.
- Step 2 or **Loading Step**. The loading process is carried out by displacement controlled analyses, beginning at the end of the Inflation Step. The inflation pressure p_ϕ is maintained constant throughout the step.

This sequence of steps is applied to every case analyzed. An additional third step, called **Deflation Step**, begins only after the end of the Loading Step for the $p_\phi = 0.20$ MPa case and deflates the beams while maintaining the boundary conditions applied in Step 2.

Inflation: Load and BCs

During the inflation step each tube is inflated to its pre-determined pressure. This step is carried out with all edges fully constrained. This choice inevitably introduces stress and deformation in the panel before the actual load step. Each subcase is tested at an inflation pressure p_ϕ of 0.05 MPa, 0.10 MPa and 0.20 MPa.

Compressive Load Cases

The compressive load case is carried through by applying a compressive displacement in Direction 1, after the tubes are inflated at the pressure of interest. The boundary conditions are applied on the edges of the panel: *Edge A* is fully constrained; *Edge B* and *Edge D* are free in Direction 1 and on *Edge C* is applied a 0.5 mm compressive displacement. The rotational degrees of freedom are constrained on all four edges. The panel without tubes is tested under the same boundary conditions. The applied compressive displacement is referred to as U_C.

The compressive load case includes three configurations: `0`, `90` and `45`. The `45` and `-45` configurations are not influenced by the direction of the compressive displacement, thus needing only one compression analysis to assess their behavior. On the other hand, the `0` and the `90` configurations produce different responses. Therefore, these configurations requires two separate analyses.

To refer to the compressive load case, the letter `C` is added to the acronym representative of the configuration investigated: `1T 0C`, `3T 0C`, `1T 90C`, `3T 90C`, `1T 45C` and `3T 45C`.

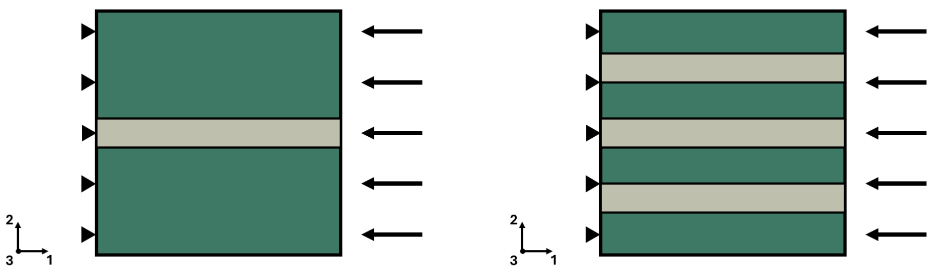

(a) `1T 0C` (b) `3T 0C`

Figure 3.6: `0` compression load case.

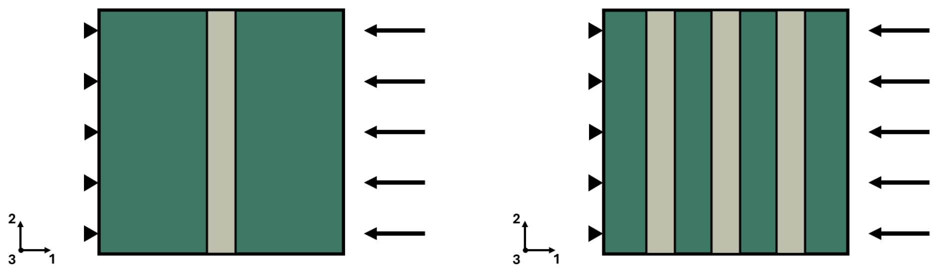

(a) `1T 90C` (b) `3T 90C`

Figure 3.7: `90` compression load case.

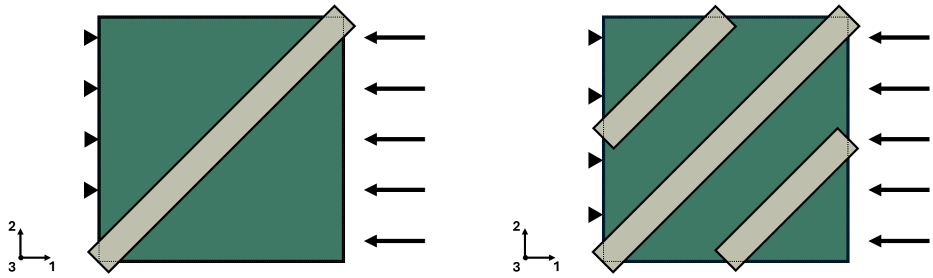

(a) `1T 45C` (b) `3T 45C`

Figure 3.8: `45` compression load case.

Shear Load Cases

All shear load cases share the same boundary conditions: *Edge A* is constrained in Direction 2 and Direction 3; *Edge B* is constrained in Direction 1 and Direction 3, on *Edge C* is applied a U2 = 0.5 mm displacement and on *Edge D* is applied a U1 = 0.5mm displacement. All rotational degrees of freedom are constrained. The controlled displacements are applied on *Edge C* and *Edge D* simultaneously. The applied shear displacement is referred to as U_S.

The configurations investigated in the shear load cases are `0`, `45` and `-45`. The response of `45` and `-45` configurations to shear loads are different, therefore they are both be tested. On the other hand, the `0` configuration is not affected by the direction of the shear load, thus not requiring the testing of the `90` models.

This load case is referred to by adding the letter `S` at the end of the acronym of the configuration of interest. Therefore, a total of six subcases are investigated: `1T 0S`, `3T 0S`, `1T 45S`, `3T 45S`, `1T -45S` and `3T -45S`.

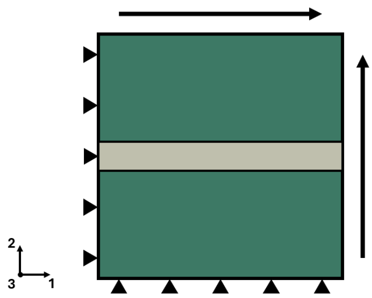

(a) `1T 0S`

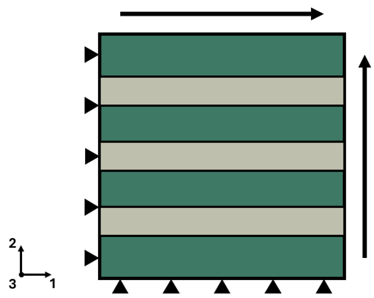

(b) `3T 0S`

Figure 3.9: `0` shear load case.

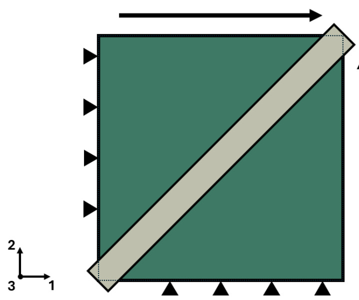

(a) `1T 45S`

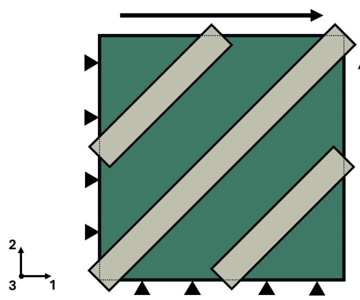

(b) `3T 45S`

Figure 3.10: `45` shear load case.

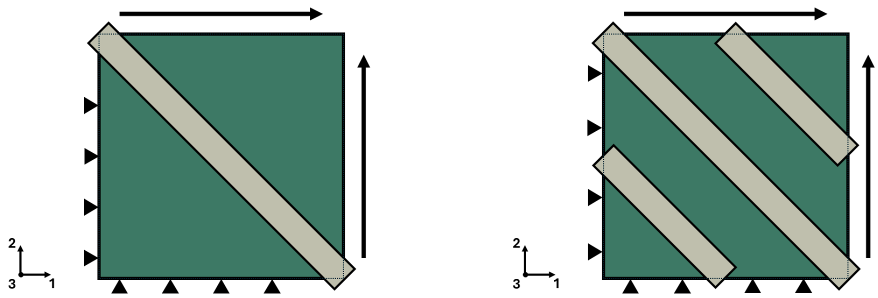

(a) 1T -45S (b) 3T -45S

Figure 3.11: -45 shear load case.

Complete list of load cases

Label	N° of tubes	Orientation angle	Load type
`1T 0C`	1	0°	Compression
`1T 90C`	1	90°	Compression
`1T 45C`	1	45°	Compression
`1T 0S`	1	0°	Shear
`1T 45S`	1	45°	Shear
`1T -45S`	1	-45°	Shear
`3T 0C`	3	0°	Compression
`3T 90C`	3	90°	Compression
`3T 45C`	3	45°	Compression
`3T 0S`	3	0°	Shear
`3T 45S`	3	45°	Shear
`3T -45S`	3	-45°	Shear

Table 3.2: Classification of load cases.

Deflation: Load and BCs

The Deflation Step, or Step 3, aims at understanding the behavior of the panel when the tubes are deflated without releasing the applied displacements. The analysis restarts from the end of Step 2, with an inflation pressure of $p_\phi = 0.20$ MPa. The applied displacements remain constant during this step. Then, the inflation pressure is gradually reduced until the tubes are completely deflated, at $p_\phi = 0.0$ MPa. Figure 3.12 shows the trend of the applied load and pressure during the deflation step.

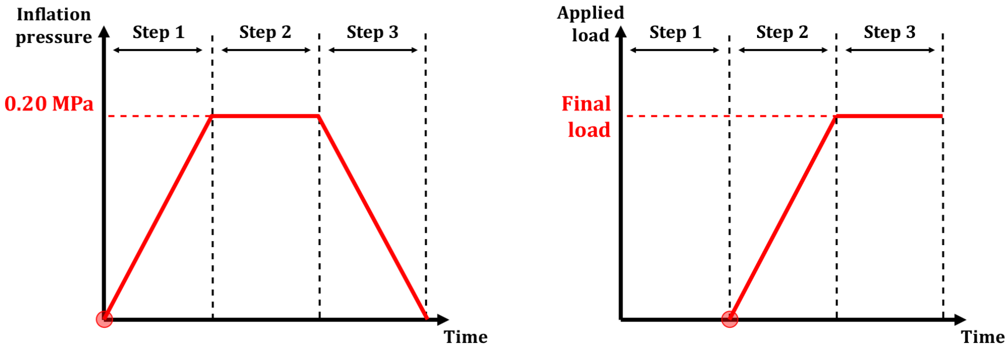

Figure 3.12: Pressure and load trends in the Deflation Step.

4 | Panel Stiffened with Inflatable Tubes: Results

In this chapter, the results of the load tests listed in Section 3.2 are presented and explained. As expected, the three-tubes configurations provide better load bearing capabilities with respect to the single-tube counterparts. The presentation of the results is divided into four sections; the first shows the effect of the inflation on the structure, the second and third separately analyze the results of the compression and shear computations, the last compares the configurations and show the advantages and downsides of each one of them.

The main output values of interest are the load in relation to the applied displacements, the effect of the inflation pressure on the load response and the buckling behavior of the panels. The compressive load is calculated as the summation of the reaction force in Direction 1 of every node in Edge A and is referred to as F_C. The shear load F_S is computed as the negative summation of the reaction force in Direction 2 of every node in Edge A.

A main phenomenon that is often cited is the "Buckling Transition", the sudden change of buckling shape experienced by the panel as the applied displacement increases. This event is pointed out and analyzed, focusing on the consequences on the load bearing capabilities of the structure and how the inflation pressure influences such phenomenon. The Deflation Step is presented for cases of particular interest and is used to investigate the load trend and the development of buckling transition as the pressure decreases at a fixed applied displacement.

4.1. Inflation Process: Results and Discussion

The analyses of the inflation process of the tubes and how it affects the panel itself are here reported. Every edge of the panel is subjected to an encastre constraint during this step. This choice is taken to ensure the same initial position of the edges in every case.

On the other hand, the constrained panel deforms under the effect inflated beam. This deformation introduces a pre-load in the panel and is reported in Table 4.1: the values relative to the compression cases refer to F_C, while those relative to shear cases refer to F_S.

	Pre-Load Values [N]					
p_ϕ [MPa]	`1T 0C`	`1T 90C`	`1T 45C`	`3T 0C`	`3T 90C`	`3T 45C`
0.05	1.98	0	1.10	6.04	0	2.50
0.10	3.50	0	0.70	11.1	0	3.42
0.20	5.00	0	-4.17	17.8	0	0.86
p_ϕ [MPa]	`1T 0S`	`1T 45S`	`1T -45S`	`3T 0S`	`3T 45S`	`3T -45S`
0.05	0	-0.83	0.83	0	-2.21	2.21
0.10	0	-1.93	1.93	0	-4.68	4.68
0.20	0	-4.65	4.65	0	-10.2	10.2

Table 4.1: Pre-loads generated by the Inflation Step.

4.2. Compression Analyses: Results and Discussion

This paragraph presents the behavior of the panels reinforced with inflatable elements, in different tube layouts, under compressive loads. As reported, the `0` configurations provide improvements in the load response of the structure, while the `90` and `45` are underwhelming.

4.2.1. Compression: `1T 0C` and `3T 0C`

The `0` provides excellent results in terms of load bearing capability. The `1T 0C` case is used to explain in detail several characteristics of the behavior of the inflatable stiffened panel, like the development of the buckling shape, the buckling transition and the interaction between tube and panel. Most of these features are present in other configurations as well.

`1T 0C`

The results from the first configuration investigated, `1T 0C`, already show the potential of inflatable beams as reinforcing elements in panels.

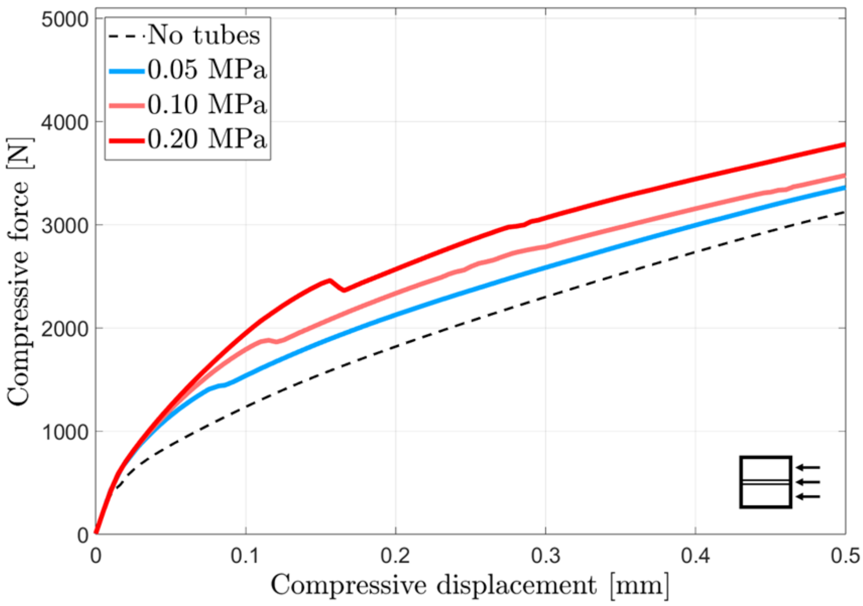

Figure 4.1: `1T 0C`: Load trends.

Figure 4.1 shows the load trend of the stiffened panels with respect to the applied displacement. The increase in load bearing capabilities is clearly related to the inflation pressure. The load trend can be divided into three main stages: a first linear stage, a second stage where local buckling starts gradually developing, and a third stage, happening after a sudden change of buckling shape. Linear behavior is visible at the beginning. The panel without tubes quickly veers off it and its stiffness drops, as it undergoes buckling. Looking at the panels with inflatable elements during this phase, the inflatable tubes do not increase the stiffness of the structure, but they do extend the span of the linear behavior. The panels with inflatable tubes begin to develop local buckles that grow in size as the compressive displacement is applied. During this phase,the inflation pressure actually plays a role in the behavior of the panel: the loss of stiffness caused by the development of local buckling is lower at higher pressures, meaning that a higher inflation pressure can guarantee better load bearing capabilities. Also, with higher inflation pressures, the sudden change of buckling shape, which characterizes the beginning of the third stage, is delayed. Figure 4.2 reports three stages of the developing of local buckling of the inflatable stiffened panel at $p_\phi = 0.20$ MPa.

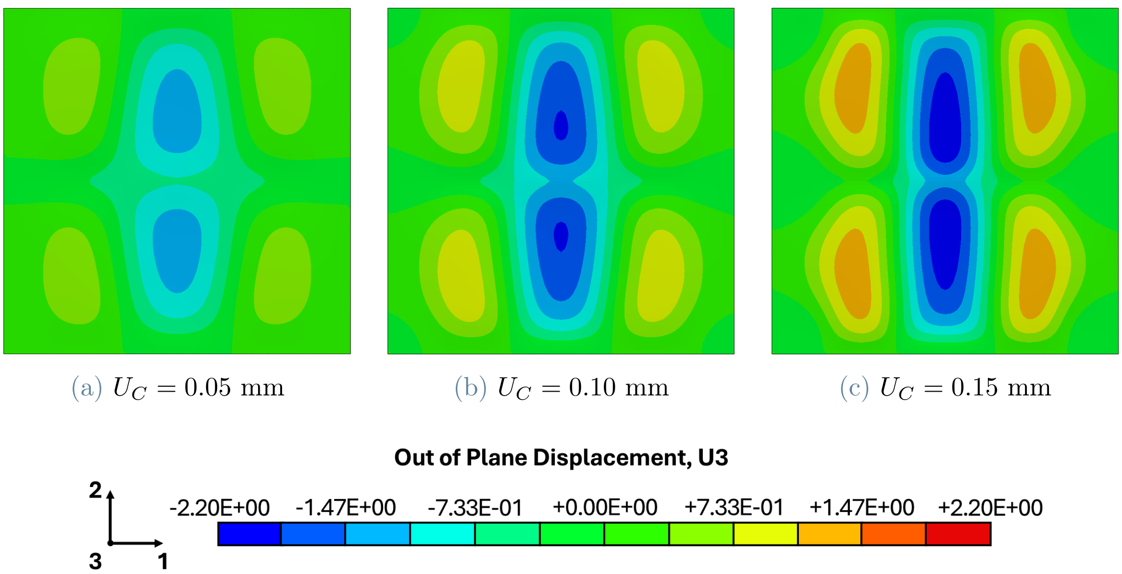

Figure 4.2: Local buckling development at $p_\phi = 0.20$ MPa.

During the third stage the improvements in load bearing capabilities that grew during the local buckling phase begin to stall and the stiffness of the panel starts reducing. The beginning of this stage, which corresponds to a sudden buckling transition, is usually marked by slight drop in the load trend that becomes more apparent as the inflation pressure increases. Such correlation, between buckling transition and loss of performance, is present in every other case investigated.

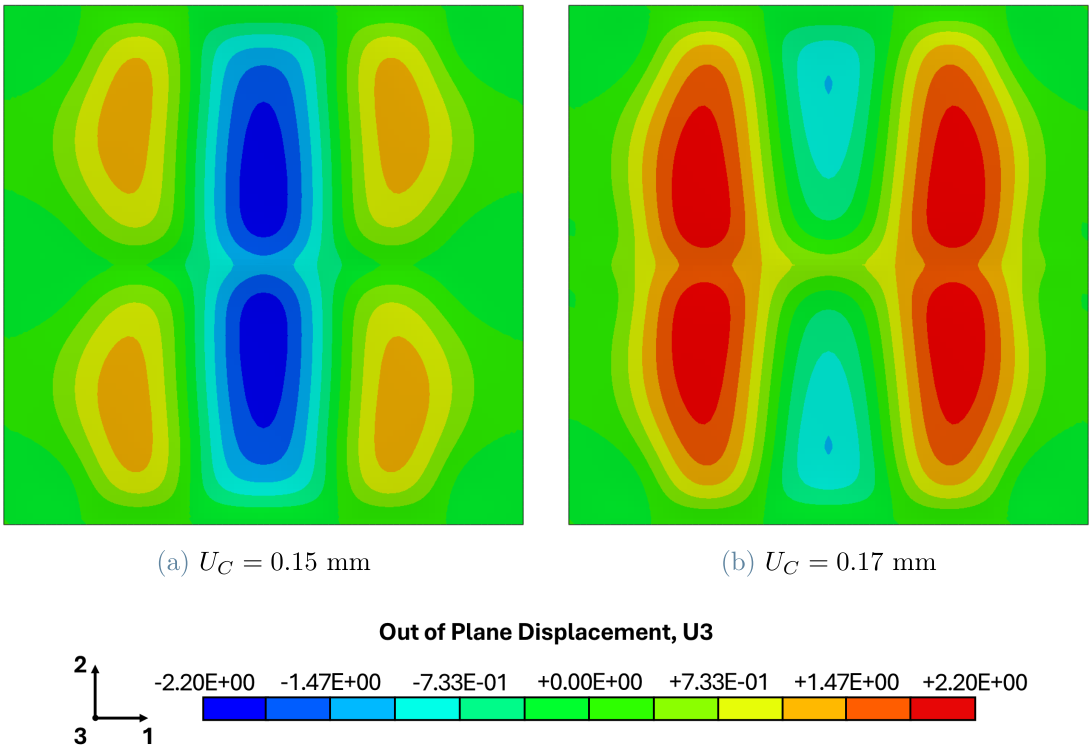

Figure 4.3: Buckling transition of `1T 0C` at $p_\phi = 0.20$ MPa.

An example of buckling transition is showcased in Figure 4.3. The figure shows the out of plane displacement U3 of the panel. The case taken into account is `1T 0C`, with beams inflated at $p_\phi = 0.20$ MPa. The two images are taken at $U_C = 0.15$ mm and $U_C = 0.17$ mm respectively and present widely different deformation patterns. Since the load trend shows a small drop around $U_C = 0.16$ mm, the correlation with the buckling transition is confirmed.
Looking at the deformation patterns, before the transition, the panel presents one main buckle partially taking over the reinforcing tube and four small, local buckles towards the corners. After the transition, such small buckles merge into two larger bumps while the central buckle almost disappears. It is also noticeable that, after the transition, the out of plane displacement produced by the buckles affects the area surrounding the tube to a larger degree.

The accurate values of the load are shown in Table 4.2, whose goal is to present the improvements in the load bearing capabilities at different stages of the loading process. Overall, the beneficial effects of the tubes gradually fade towards the end of the application of the compressive displacement. The peak in performance of the stiffened panels is found at the beginning of the compression process, when the panel is still developing local buckling and has not reached large buckling deformations yet. For example, when $U_C = 0.1$ mm the tube inflated at $p_\phi = 0.20$ MPa is able to provide a 61% load increase with respect to the model without tubes. Such improvement, however, decreases to 21% by the end of the loading process.

	U_C [mm]	0.1	0.2	0.3	0.4	0.5
No tubes	F_C [N]	1210	1801	2283	2721	3123
$p_\phi = 0.05$ [MPa]	F_C [N]	1547	2134	2593	3013	3360
	ΔF_C [N]	337	333	310	292	237
	% Increase	27.9	18.5	13.6	10.7	7.6
$p_\phi = 0.10$ [MPa]	F_C [N]	1790	2334	2785	3154	3477
	ΔF_C [N]	580	533	502	433	354
	% Increase	47.9	29.6	22.0	15.9	11.3
$p_\phi = 0.20$ [MPa]	F_C [N]	1948	2567	3065	3443	3778
	ΔF_C [N]	738	766	782	722	655
	% Increase	61.0	42.5	34.3	26.5	21.0

Table 4.2: `1T 0C`: Compressive load values.

Figure 4.4 shows the out of plane displacement of the panel along the center line, where it is tied to the tube, at different inflation pressures and at the end of the Loading Step. Although the maximum out of plane displacement is similar among all cases; at higher pressures only one of the four buckles reaches this peak, while the remaining three are less prominent. The buckling shape of the $p_\phi = 0.10$ MPa and $p_\phi = 0.20$ MPa cases may seem different at first, however the distribution of the buckles is similar, but shifted by one halfwave. In both cases, the largest buckle presents similar magnitude, while the three remaining are significantly smaller for $p_\phi = 0.20$ MPa.

In the panel with inflatable elements, the interaction between the tube and the panel is more complicated: the buckles of the panel can deform the cross section of the tubes, by sinking into the membrane fabric or by rising away from it. The buckling mode of the panel is not totally transferred to the beam, as only the surface in contact with the panel is forced to follow the same deformation pattern. The portion of the beam not facing the panel may not be globally affected by the panel buckling mode, but some local effects are still present. Figure 4.5 shows the influence of the panel on the beam inflated at $p_\phi = 0.20$ MPa. When the buckle is in the positive out of plane displacement, the

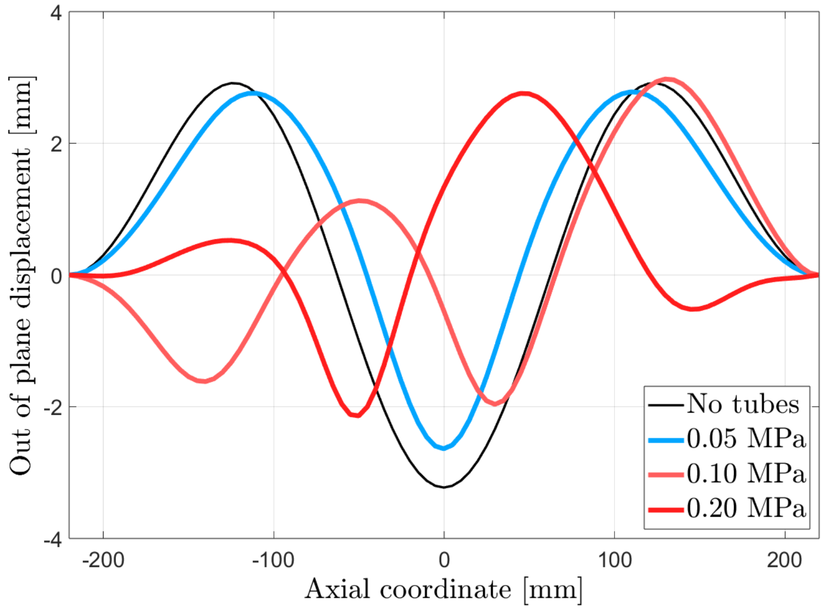

Figure 4.4: `1T 0C`: Displacements along the center line.

lower surface of the beam gets compressed, which can cause local wrinkling. On the other hand, when the buckle sinks into the tube, the lower surface is further tensioned. Due to this interaction, using analytical beam formulations to model the stiffeners could not accurately depict the behavior of the inflatable stiffened panel.

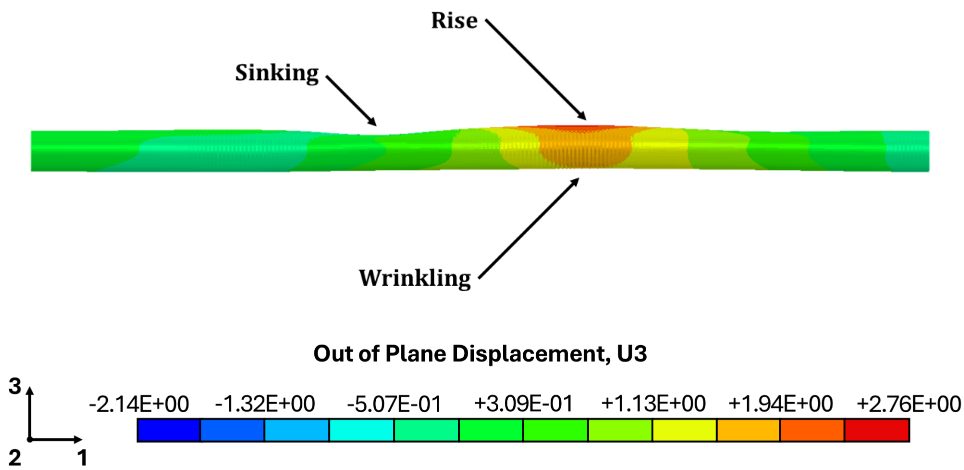

Figure 4.5: Beam deformation

The inflatable tube was deflated at the end of the $p_\phi = 0.20$ MPa test to check the influence of the inflation pressure on the panel at a fixed displacement $U_C = 0.50$ mm. Figure 4.6 shows the load response of the panel as the pressure is diminished and represents with an

'X' the values of the load obtained at the end of the Loading Analysis, for each inflation pressure. A discrepancy is noticeable for $p_\phi = 0.05$ MPa, where the deflation load trend underperforms with respect to the results from the Loading Analysis. This discrepancy is explained by the buckling shapes providing different load responses.

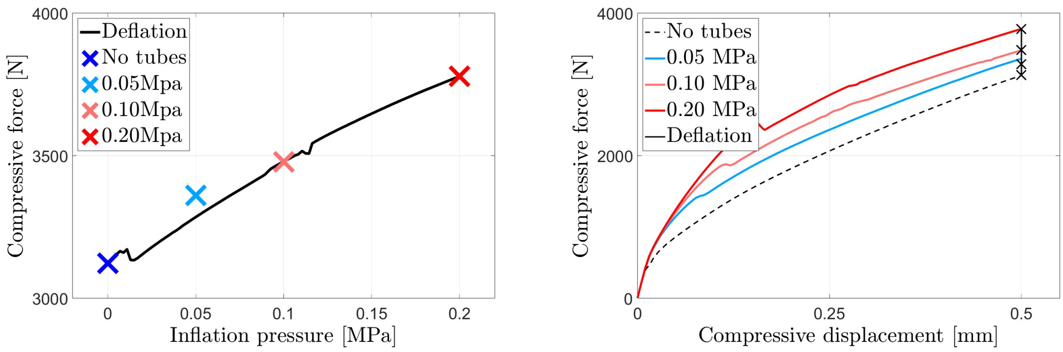

Figure 4.6: `1T 0C`: Deflation analysis.

During the Deflation Analysis the buckling mode resembles that of the $p_\phi = 0.20$ MPa test all the way down to 0.02 MPa. Figure 4.7 reports the buckling shapes at the end of each Loading Analysis and those obtained during the Deflation Analysis. The load raise towards the end of the deflation represents the shift in the deformation pattern from four to three buckles. When the pressure is constant and at $p_\phi = 0.05$ MPa, the three-buckle buckling mode naturally appears on the panel. The Deflation Analysis shows that, to obtain the same buckling shape of the $p_\phi = 0.05$ MPa Loading Analysis from an already deformed panel, it is necessary to deflate the beams almost completely and it is not enough to stop at 0.05 MPa.

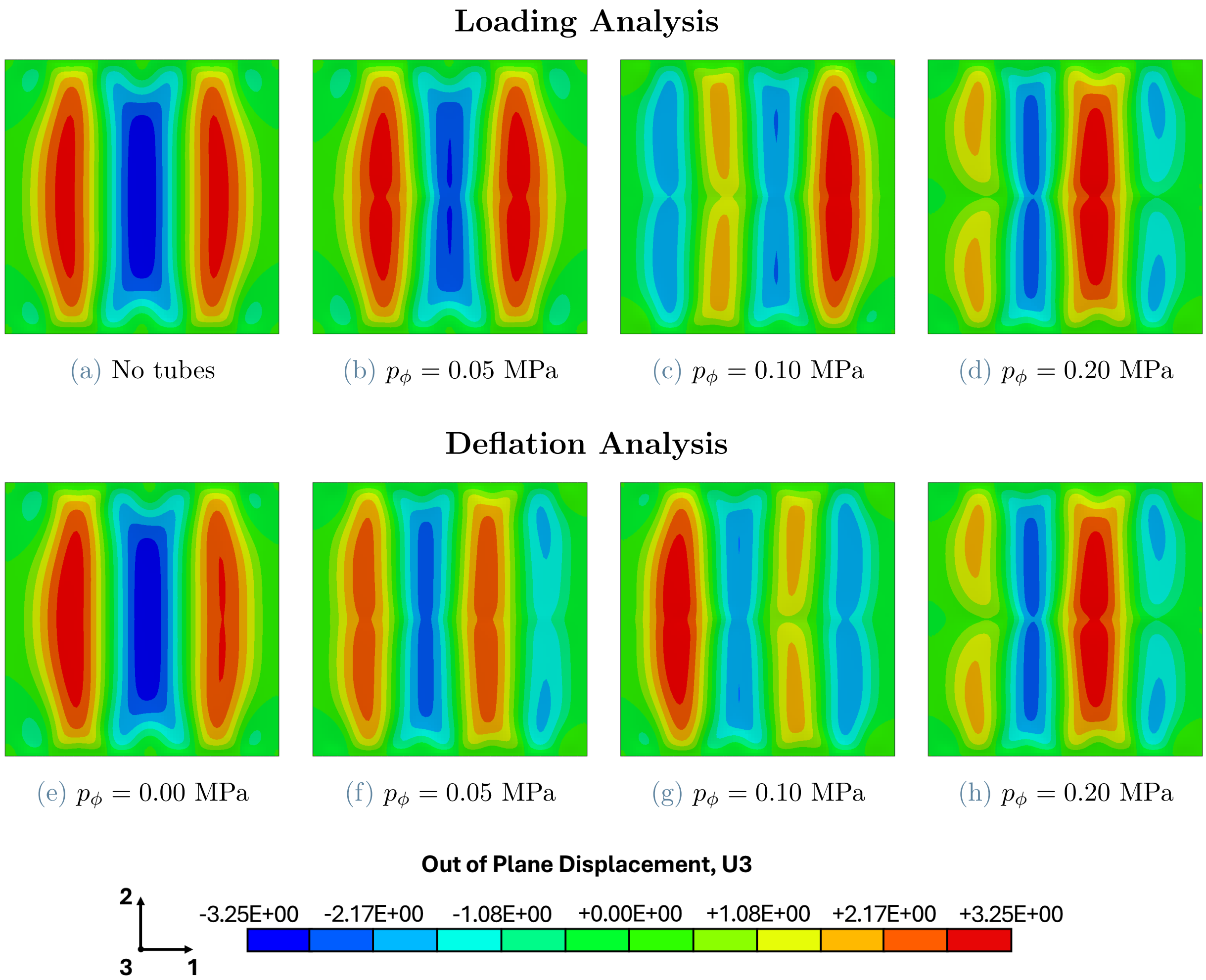

Figure 4.7: `1T 0C`: Comparison of buckling shapes between the Loading Analyses and Deflation Analysis.

`3T 0C`

The three-tubes configuration introduces more relevant improvements with respect to `1T 0C`, as shown in Figure 4.8. Firstly, the overall structure presents better load bearing capabilities with respect to the single-beam counterpart.

The linear behavior is maintained for longer and the first buckling transition is delayed with respect to `1T 0C`, at the same inflation pressures. Consequentially, the drop in stiffness during the development of local buckling happens throughout a longer span. For example, taking into account the test conducted at $p_\phi = 0.20$ MPa, the buckling transition happens at around $U_C = 0.38$ mm and $F_C = 4600$N, while in `1T 0C` at about $U_C = 0.16$ mm and $F_C = 2450$N.

Overall, when the tubes are inflated at $p_\phi = 0.05$ MPa they suffer one buckling transition

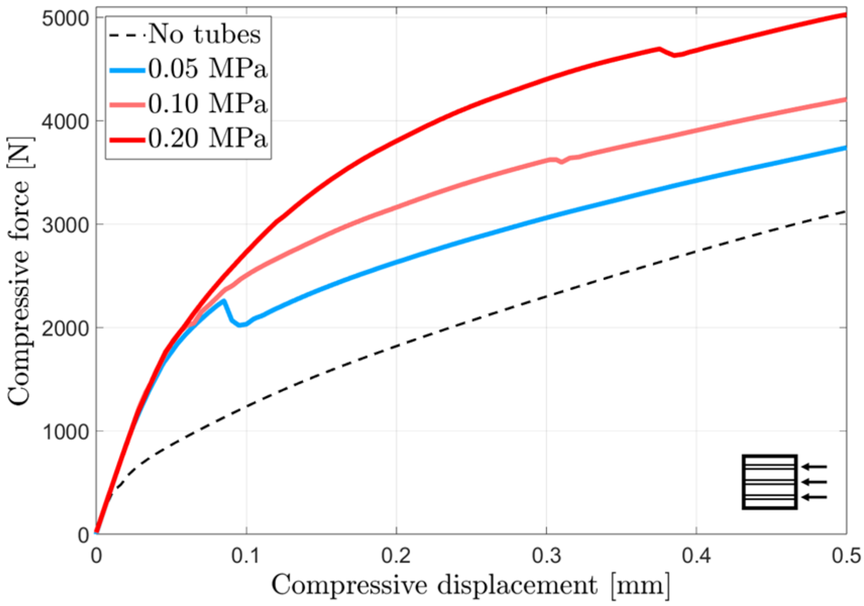

Figure 4.8: `3T 0C`: Load trends.

at an early stage of the loading process, which produces a large drop in the load trend; when $p_\phi = 0.10$ MPa, the buckling transition is delayed further producing a smaller performance drop; when $p_\phi = 0.20$ MPa the buckling transition is recorded towards the end of the Loading Step. The main effect produced by the inflation pressure is shown during the development of the first local buckles, where the higher pressure reduces the drop of stiffness caused by the buckling. Eventually, every configuration experiences a sudden change in buckling shape, which causes a drop in performance. Such deformation is delayed proportionally to the inflation pressure, making high pressure configuration stiffer.

Figure 4.9 reports the sequences of deformed shapes of the panel with inflatable tubes during the loading process. The first row refers to the panel with tubes inflated at $p_\phi = 0.05$ MPa, the second at $p_\phi = 0.20$ MPa. The Figure shows how at $p_\phi = 0.05$ MPa the deformed shape obtained after the buckling transition is maintained throughout the analysis, while at $p_\phi = 0.20$ MPa the panel develops local buckles for longer, up until $U_C = 0.30$ mm, before transitioning to a global buckling mode.

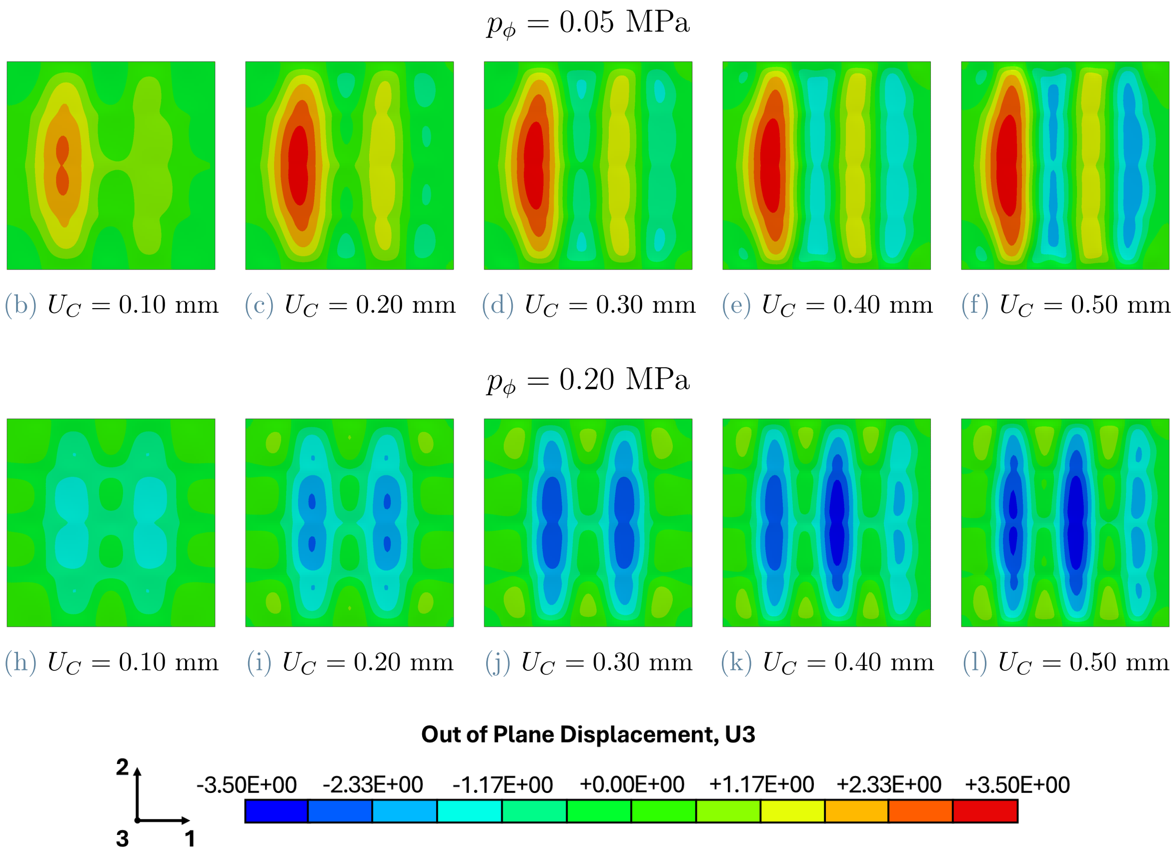

Figure 4.9: `3T 0C`: Sequence of deformed shapes at different pressure levels.

As shown in Table 4.3, both $p_\phi = 0.10$ MPa and $p_\phi = 0.20$ MPa show a positive trend in the load increase up to about halfway through the compression process, before losing in performance towards the end.

Furthermore, when $p_\phi = 0.05$ MPa, although the panel gains in stiffness only in the first instants of the loading process and then sees a constant decline in the improvements, the overall load bearing capabilities are similar to the $p_\phi = 0.20$ MPa test from `1T 0C`. Like the single-tube configuration, the peak in performance is provided during the first moments of the Loading Step. The results are more prominent however, as the load is more than doubled both when $p_\phi = 0.10$ MPa and $p_\phi = 0.20$ MPa.

	U_C [mm]	0.1	0.2	0.3	0.4	0.5
No tubes	F_C N	1210	1801	2283	2721	3123
$p_\phi = 0.05$ MPa	F_C [N]	2030	2630	3060	3420	3738
	ΔF_C [N]	820	829	777	699	615
	% Increase	67.7	46.0	34.0	25.7	19.7
$p_\phi = 0.10$ MPa	F_C [N]	2522	3180	3608	3907	4206
	ΔF_C [N]	1312	1379	1325	1186	1083
	% Increase	108.4	76.5	58.0	43.6	34.7
$p_\phi = 0.20$ MPa	F_C [N]	2728	3823	4400	4680	5026
	ΔF_C [N]	1518	2022	2117	1959	1903
	% Increase	125.4	112.3	92.7	72.0	60.9

Table 4.3: `3T 0C`: Compressive load values.

The Deflation Step of `3T 0C` validates the load values obtained during the Loading Step. Figure 4.10 shows the load trend that the structure follows during the Deflation Analysis. These values match the curve obtained from the deflation analysis. A drop in the load can be seen between $p_\phi = 0.10$ MPa and $p_\phi = 0.20$ MPa, representing a buckling transition caused by the deflation of the tubes.

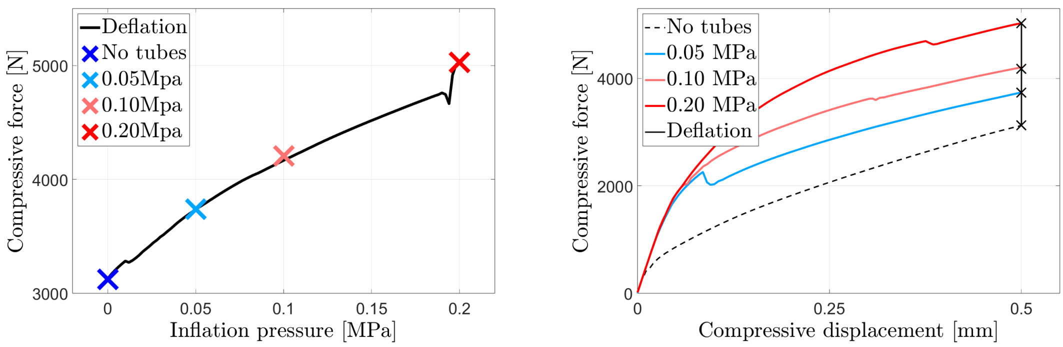

Figure 4.10: `3T 0C`: Deflation analysis.

The deformed shapes obtained at the end of the Loading Step and at the pressures of interest of the Deflation Analysis are shown in Figure 4.10. At $p_\phi = 0.10$ MPa the deformation pattern is different. This could be caused by the influence of the initial buckling mode of the Deflation Analysis, corresponding to that of the Loading Analysis at $p_\phi = 0.20$ MPa. The initial deformation shape in the Deflation Analysis is not symmetric and it maintains this feature as the pressure decreases, thus not corresponding with the symmetric deformation pattern of the $p_\phi = 0.10$ MPa case.

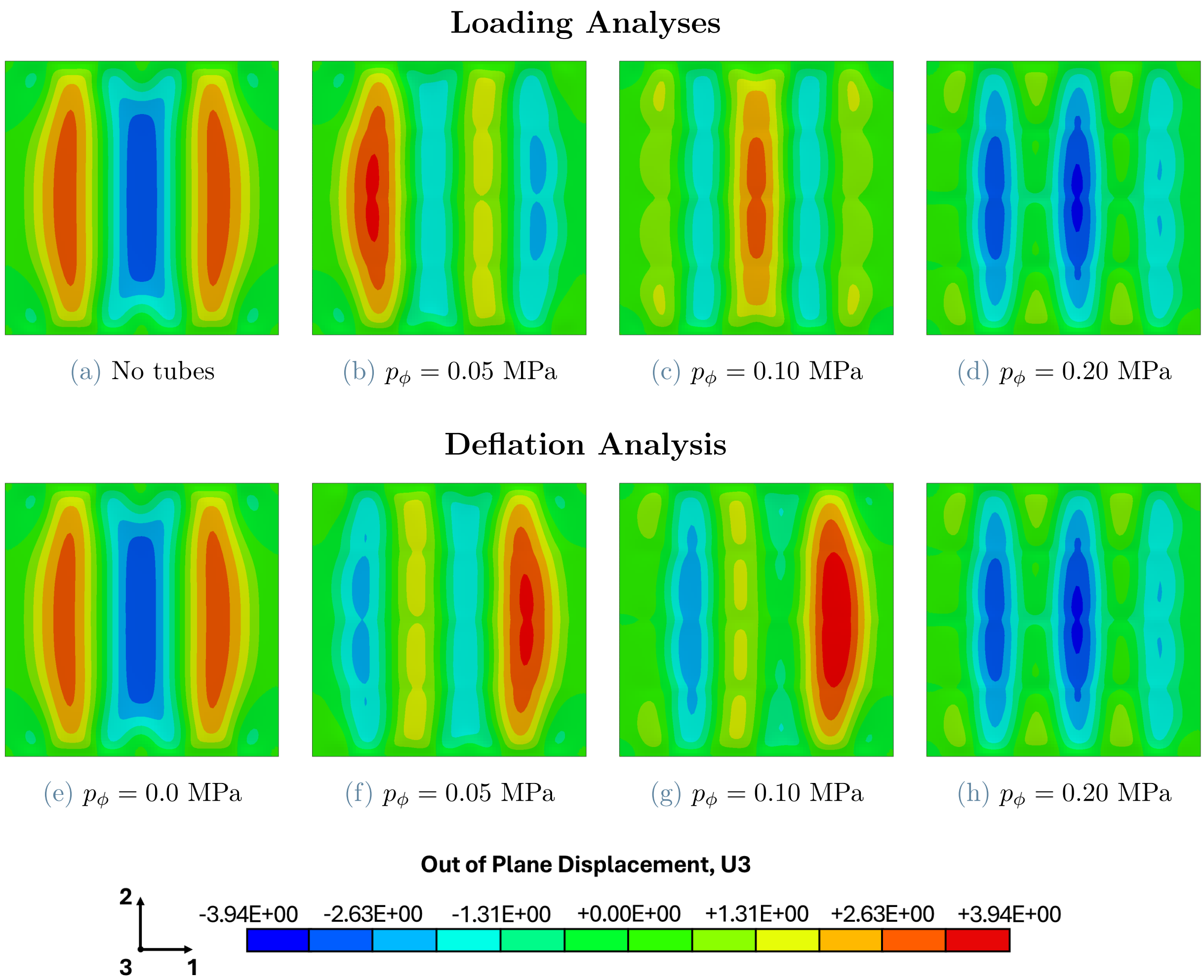

(a) No tubes (b) $p_\phi = 0.05$ MPa (c) $p_\phi = 0.10$ MPa (d) $p_\phi = 0.20$ MPa

(e) $p_\phi = 0.0$ MPa (f) $p_\phi = 0.05$ MPa (g) $p_\phi = 0.10$ MPa (h) $p_\phi = 0.20$ MPa

Figure 4.11: `3T 0C`: Comparison of buckling shapes from the Loading Analyses and Deflation Analyses.

4.2.2. Compression: `1T 90C` and `3T 90C`

While the previous compression case provided excellent results in terms of load bearing capabilities, the same cannot be said for `90C`. In this analysis, the compressive displacement is applied perpendicularly to the inflatable beams, which cannot provide any support to the panel. Both in `1T 90C` and `3T 90C`, the inflatable tubes not only do not provide any benefits, but actually reduce the load that the panel is able to support. Figure 4.12 shows the load trend of the stiffened panel in the `1T 90C` and `3T 90C` configurations. The number of inflatable beams does not influence the response of the structure, nor does the inflation pressure. By the end of the Loading Step, the performance of the panel has dropped by 30%. The loss in load bearing capability can be attributed to the higher number of buckles, which reduces the overall stiffness of the structure.

As shown in Figure 4.13, the panel is deformed by four buckles throughout the loading process. Although the direction of the buckle changes, the deformation pattern is consistent among all inflation pressures.

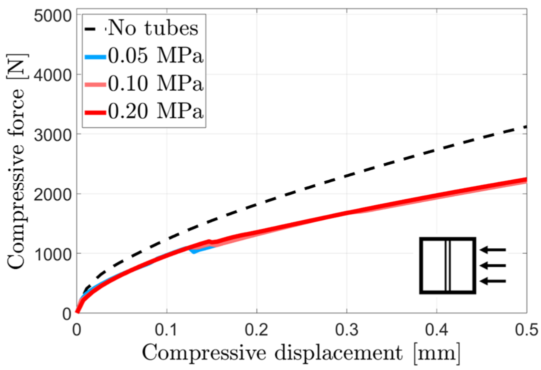

(a) `1T 0C`

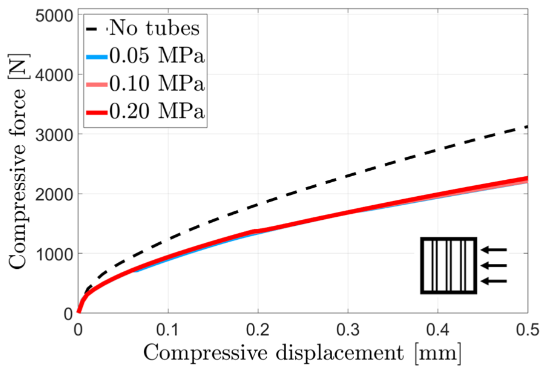

(b) `3T 0C`

Figure 4.12: `90C`: Load trends.

$p_\phi = 0.05$ MPa

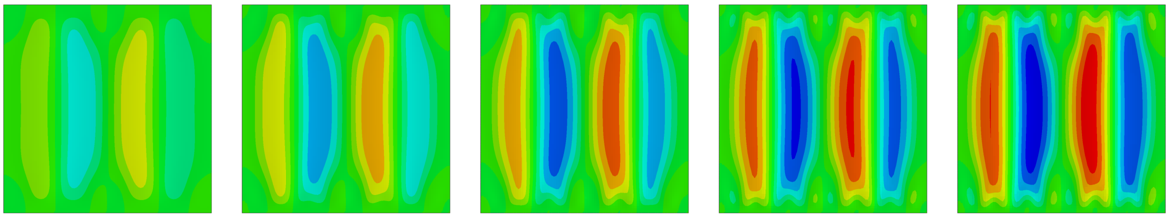

(b) $U_C = 0.10$ mm (c) $U_C = 0.20$ mm (d) $U_C = 0.30$ mm (e) $U_C = 0.40$ mm (f) $U_C = 0.50$ mm

$p_\phi = 0.20$ MPa

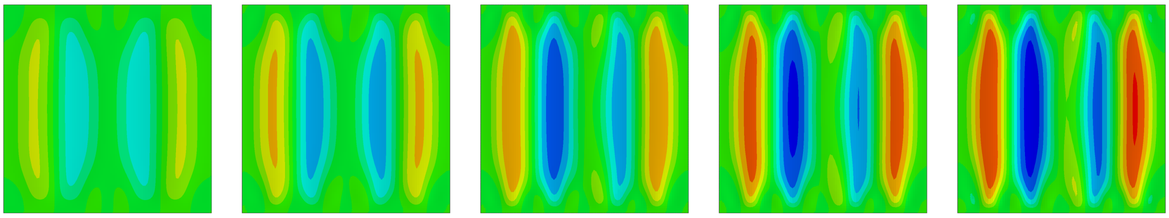

(h) $U_C = 0.10$ mm (i) $U_C = 0.20$ mm (j) $U_C = 0.30$ mm (k) $U_C = 0.40$ mm (l) $U_C = 0.50$ mm

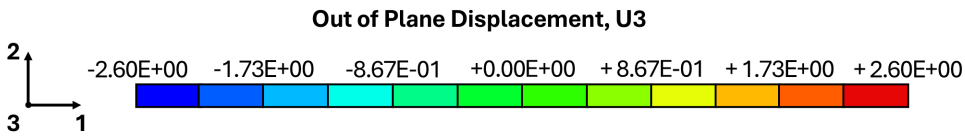

Figure 4.13: `3T 90C`: Sequence of deformed shapes at different pressure levels.

Figure 4.14 compares the out of plane displacements of the panel without tubes with `3T 90C` inflated at $p_\phi = 0.10$ MPa and shows how the inflatable tubes block the panel from forming larger buckles. Instead, they force the development of more buckles in between the tubes causing the drop in performance of the structure.

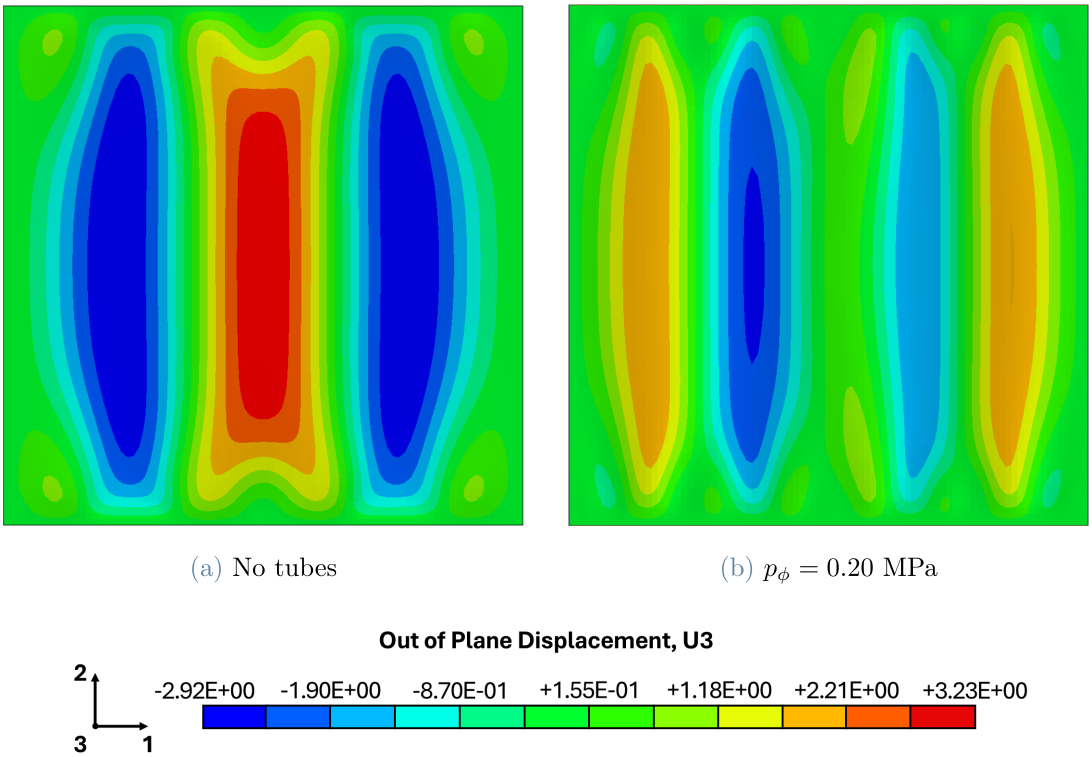

Figure 4.14: Buckling deformation of `3T 90C`

4.2.3. Compression: `1T 45C` and `3T 45C`

The `45C` compression analyses provide good results, although not at the same level as the `0C` configuration. The load response of `1T 45C` and `3T 45C` are reported in Figure 4.15. It is immediately noticeable that the three-tubes configuration does not add significant benefits with respect to the single-tube configuration. The only improvements introduced by `3T 45` can be seen at the beginning of the Loading Step, where the overall stiffness of the structure is higher. Eventually the buckling transitions cause several drops in the performance of the panels. By the end, the difference in F_C of the two configurations is no larger than 200 N at the same inflation pressure.

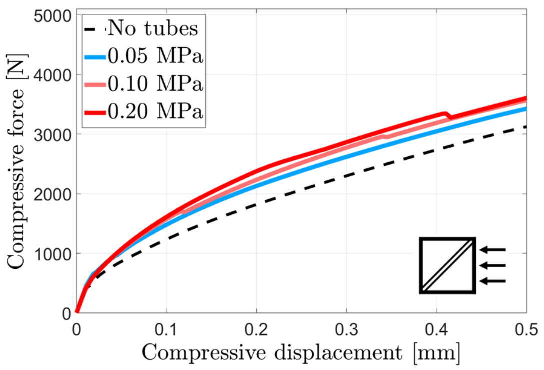

(a) `1T 45C`

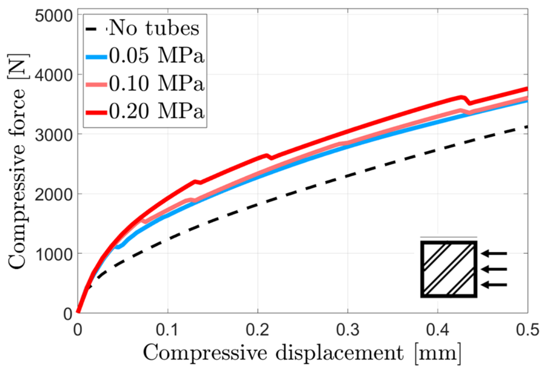

(b) `3T 45C`

Figure 4.15: `45C`: Load trends.

The deformation patterns of the panels at the end of the Loading Step, at all inflation pressures, resemble that of the counterpart without tubes, as reported in Figure 4.16. As the pressure decreases further, the magnitude of the main buckle slightly reduces. In the case at $p_\phi = 0.05$ MPa, the buckles rise in opposite direction with respect to the other results. The pattern of the deformation is however the same.

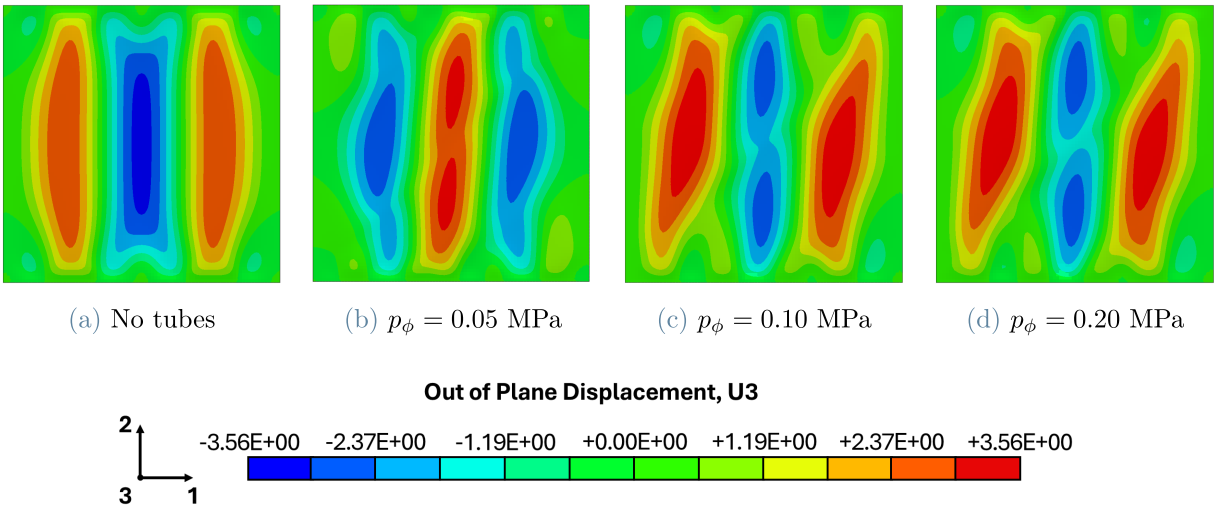

Figure 4.16: `3T 45C`: Deformed shapes.

4.3. Shear Analyses: Results and Discussion

This paragraph follows the same thread as the previous one and explains the results of the configurations under shear load.

4.3.1. Shear: `1T 0S` and `3T 0S`

The shear analyses of the `0` configurations produce mixed results. The single-tube model does not provide satisfying results, especially at higher inflation pressures; on the other hand, the `3T 0S` responds well and widely improves the load bearing capabilities of the structure.

`1T 0S`

As shown in Figure 4.17, implementing a single inflatable tube does not provide significant benefits. Although the load bearing capabilities are affected positively by the tube, the inflation pressure stops providing improvements once it reaches a certain value (which cannot be deduced by this graph, but is shown in Figure 4.18). This phenomenon can be observed in both $p_\phi = 0.10$ MPa and $p_\phi = 0.20$ MPa having overlapping load trends.

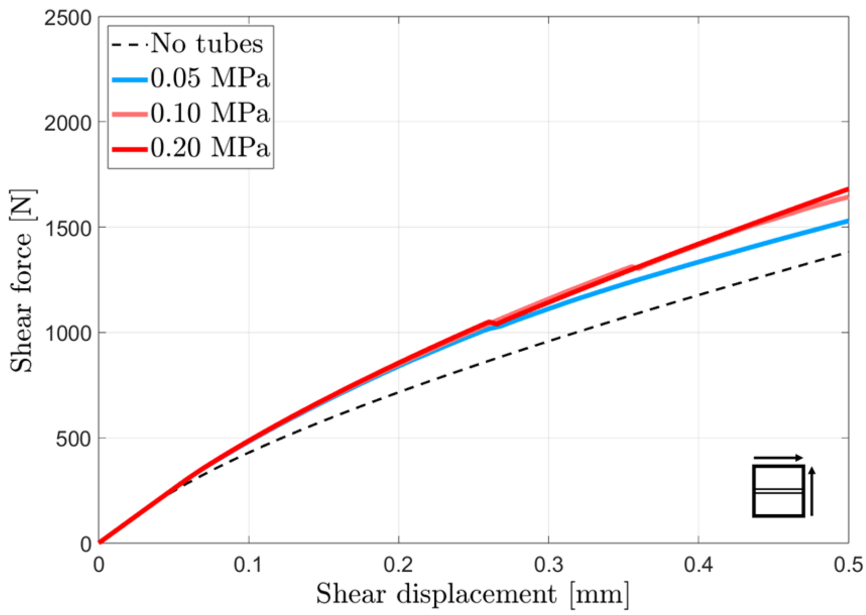

Figure 4.17: `1T 0S`: Load trends.

Figure 4.18 shows the deflation of the beam at $U_S = 0.5$mm. In the first place, the values of the load obtained from the application of the displacement match the results obtained from the deflation. Furthermore, the behavior of the tube shows an almost linear trend between $p_\phi = 0$ MPa and $p_\phi = 0.11$ MPa, and reaches a plateau after, making any increase in inflation pressure essentially useless.

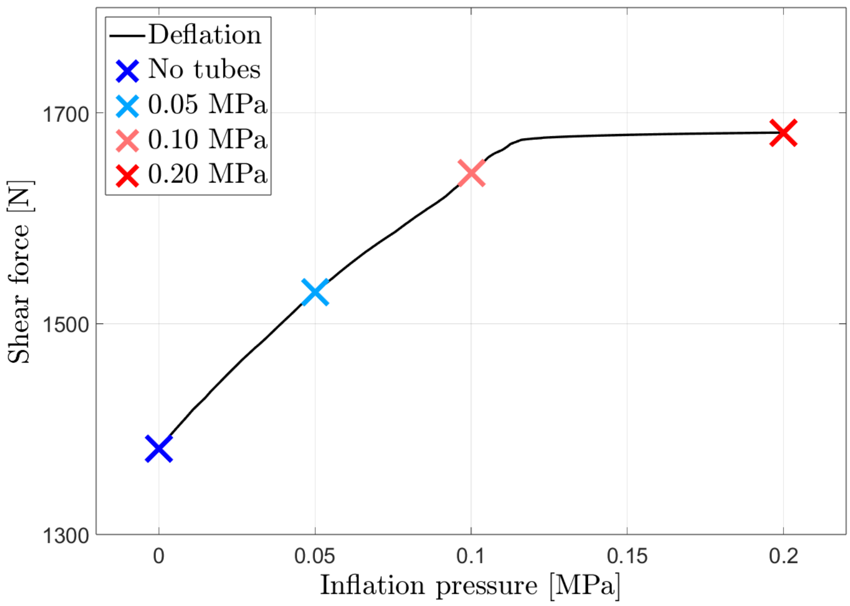

Figure 4.18: `1T 0S`: Deflation analysis.

Although the influence of inflation pressure on the load starts fading after $p_\phi = 0.10$ MPa, its effect is still relevant on the buckling shape. As shown in Figure 4.19, the inflation pressure plays a key role in maintaining the buckles localized around the beam and avoiding the development of global buckling behavior. As the pressure decreases, the central buckle becomes increasingly larger, resembling the deformed shape of the panel without tubes. Already at $p_\phi = 0.05$ MPa, the buckle has expanded over the inflatable tube, while the tube inflated at higher pressures is able to keep it split in two.

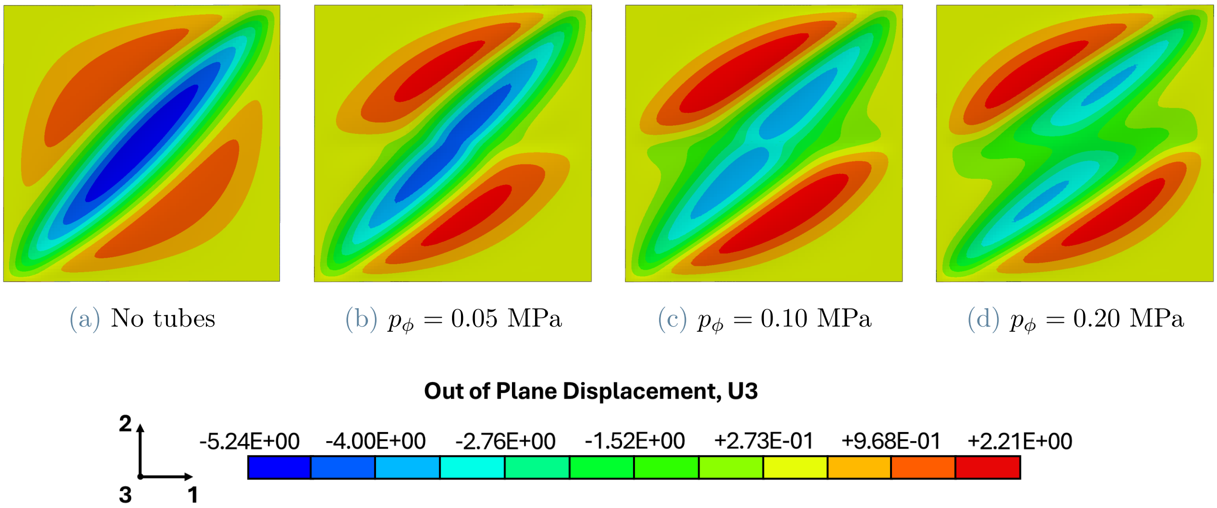

Figure 4.19: `1T 0S`: Deformed shapes.

3T 0S

The results obtained from `3T 0S` are more promising. As shown in Figure 4.20, the load trends experience greater improvements. Similarly to the compression case, the stiffened panels maintain a longer linear phase. The stiffness begins to drop as local buckling starts developing in between the inflatable tubes.

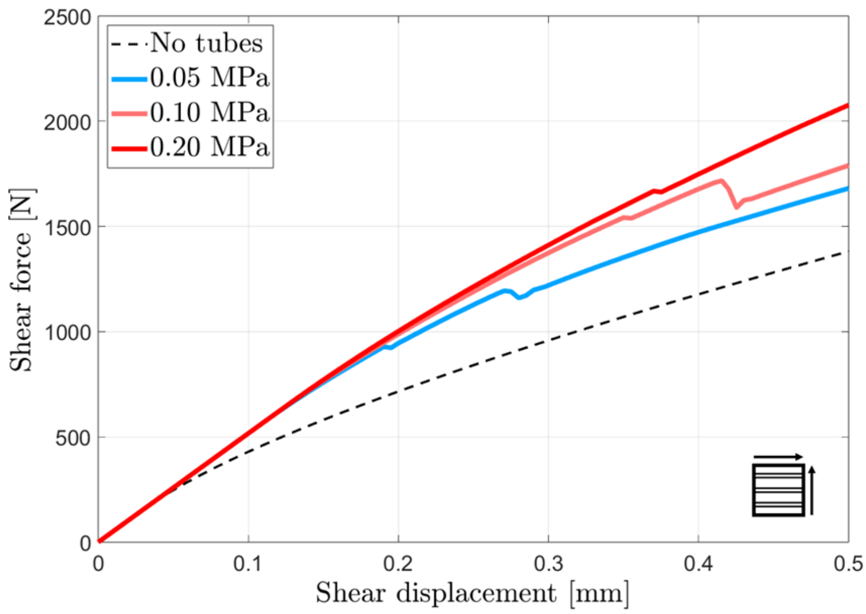

Figure 4.20: `3T 0S`: Load trends.

The development of the buckling goes through three distinct phases which can be observed from the load response of the stiffened panels. The first one, similarly to the compression case `0C`, consists of a gradual growth of the buckles in between the tubes. Eventually, one of the buckles expands over the central beam. Therefore, the buckling is not localized around the beams anymore but begins to affect a bigger portion of the structure. This buckling transition causes the load trend to drop slightly and affects all three inflation pressures, as shown Figure 4.20. As the shear displacement is applied, the buckling takes over the whole panel. This event causes a larger drop in performance and affects only the models with an inflation pressure of $p_\phi = 0.05$ MPa and $p_\phi = 0.10$ MPa. The structure inflated at $p_\phi = 0.20$ MPa does not suffer the second buckling transition by the end during the Loading Step. Figure 4.21 presents the development of the out of plane displacement on the panels with tubes inflated at $p_\phi = 0.05$ MPa and $p_\phi = 0.20$ MPa. At $p_\phi = 0.20$ MPa, the tubes are able to keep the buckles localized.

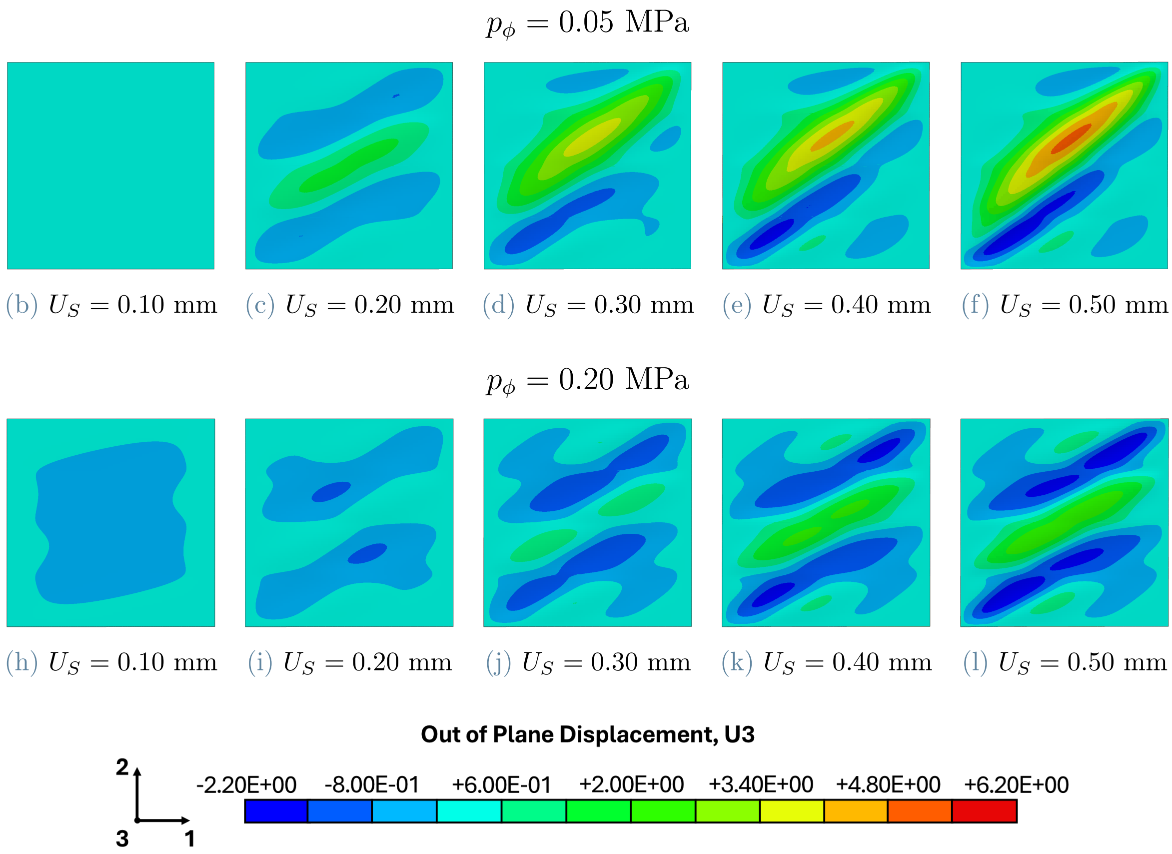

Figure 4.21: `3T 0C`: Sequence of deformed shapes at different pressure levels.

The development of the buckling shape of `3T 0S` configuration inflated at $p_\phi = 0.10$ MPa is represented in Figure 4.22. The series of images represents the three main buckling shapes experienced by the panel, by showing the out of plane displacement patterns. The first image of figure 4.22 represents the deformed shape of the panel when the applied shear displacement is $U_S = 0.34$ mm, right before the first buckling transition; during this phase, the inflatable tubes are able to maintain the buckles separated into the unsupported regions of the panel. The second image represents the deformed shape of the panel right after the first buckling transition, and shows a significant enlargement of the central buckle, which has taken over the middle beam and has assumed partially global behavior. The outer buckles are relegated to the sides of the panel and do not affect the two external tubes. As the applied shear displacement keeps increasing, buckling expands over the remaining beams. The third image of Figure 4.22 shows the deformed shape of the panel at the end of the loading process; the panel is affected by a single, large buckle and the out of plane displacements suffered a significant rise.

This chain of events is delayed by higher inflation pressures. In Figure 4.20, every drop

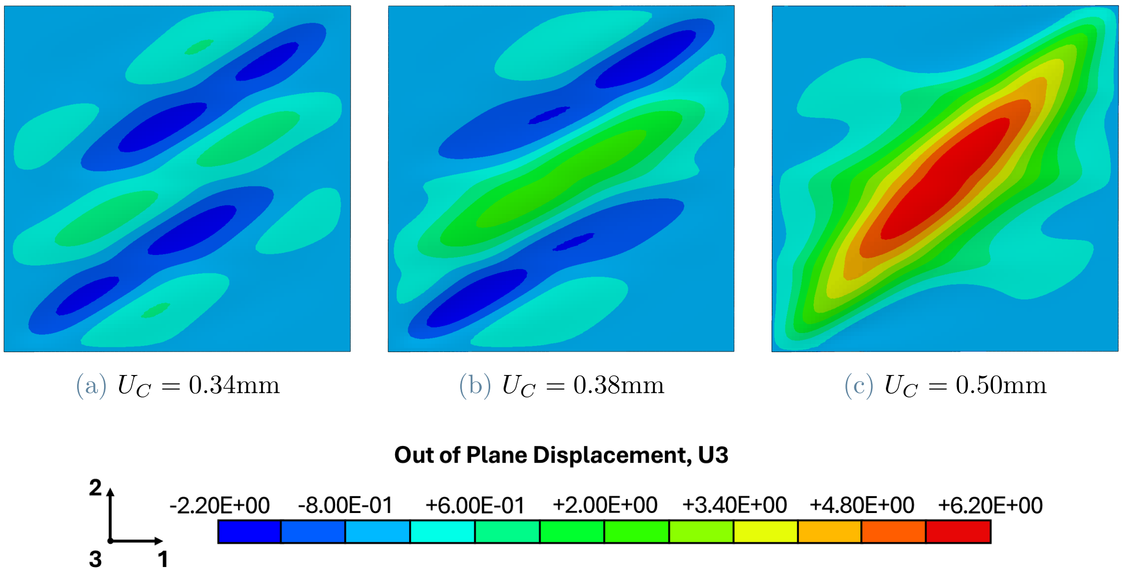

Figure 4.22: Development of buckling in `3T 0S` inflated at $p_\phi = 0.10$ MPa.

in the load can hint to a buckling shift; for $p_\phi = 0.05$ MPa and $p_\phi = 0.10$ MPa, the panels undergo two buckling transitions and, by the end of the application of the shear displacement, they are both globally affected by buckling; on the other hand, the beams inflated at $p_\phi = 0.20$ MPa are able to maintain the buckling localized.

The overall performance of the stiffened panels is reported in Table 4.4. The panels affected by two buckling transitions show a reduction in the improvements provided by the tubes towards the end of the step. For $p_\phi = 0.05$ MPa, the load increase begins to plateau towards the end. When the inflation pressure is $p_\phi = 0.10$ MPa, the globalization of the buckling behavior produces a sudden drop in performance. The best performance is obtained for $p_\phi = 0.20$ MPa: the load increase as well as the percentage increase show a consistent positive trend throughout the application of the shear displacement.

	U_S [mm]	0.1	0.2	0.3	0.4	0.5
No tubes	F_S [N]	429	716	958	1177	1382
$p_\phi = 0.05$ MPa	Load F_S [N]	517	945	1220	1473	1681
	ΔF_S [N]	88	229	262	296	299
	% Increase	20.5	32.0	27.3	25.1	21.6
$p_\phi = 0.10$ MPa	F_S [N]	517	989	1376	1678	1790
	ΔF_S [N] N	88	273	418	501	408
	% Increase	20.5	38.1	43.6	42.6	29.5
$p_\phi = 0.20$ MPa	F_S [N]	517	1002	1411	1748	2077
	ΔF_S [N]	88	286	453	571	695
	% Increase	20.5	39.9	47.3	48.5	50.3

Table 4.4: `3T 0S`: Shear load values.

The curve obtained from the Deflation Step confirms the results obtained in the previous analyses. As shown in Figure 4.23, the load values obtained at the end of the previous analyses match the trend produced by the deflation. The drop in performance, representative of a buckling transition, happens in between $p_\phi = 0.10$ MPa and $p_\phi = 0.20$ MPa, which agrees with the results obtained from the analyses presented in Figure 4.20.

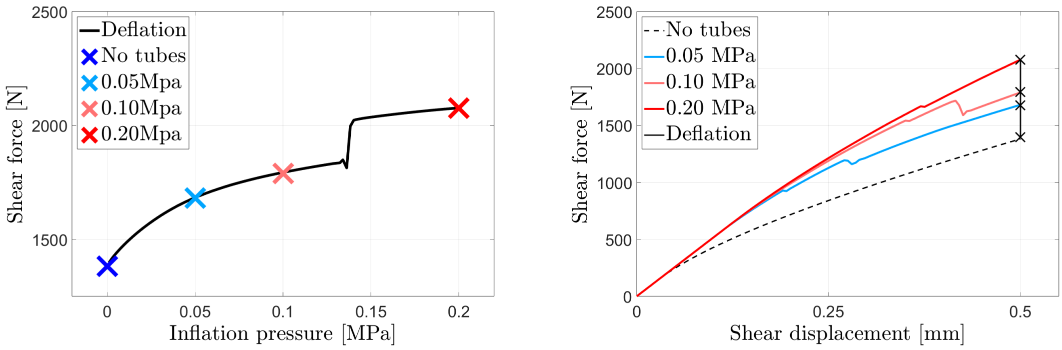

Figure 4.23: `3T 0S`: Deflation analysis.

Figure 4.24 compares the deformation patterns obtained from the Deflation Analysis and the Loading Analysis. A difference at $p_\phi = 0.05$ MPa can be noted. Similarly to the `3T 0C` case, the initial buckling mode in the Deflation Analysis may have influenced the deformation shape at $p_\phi = 0.05$ MPa, since the pattern is maintained from $p_\phi = 0.10$ MPa. In addition, both $p_\phi = 0.05$ MPa and $p_\phi = 0.10$ MPa suffered two buckling transitions. The deflation analysis is coherent with these results, since it does not produce any buckling transition between the two pressures.

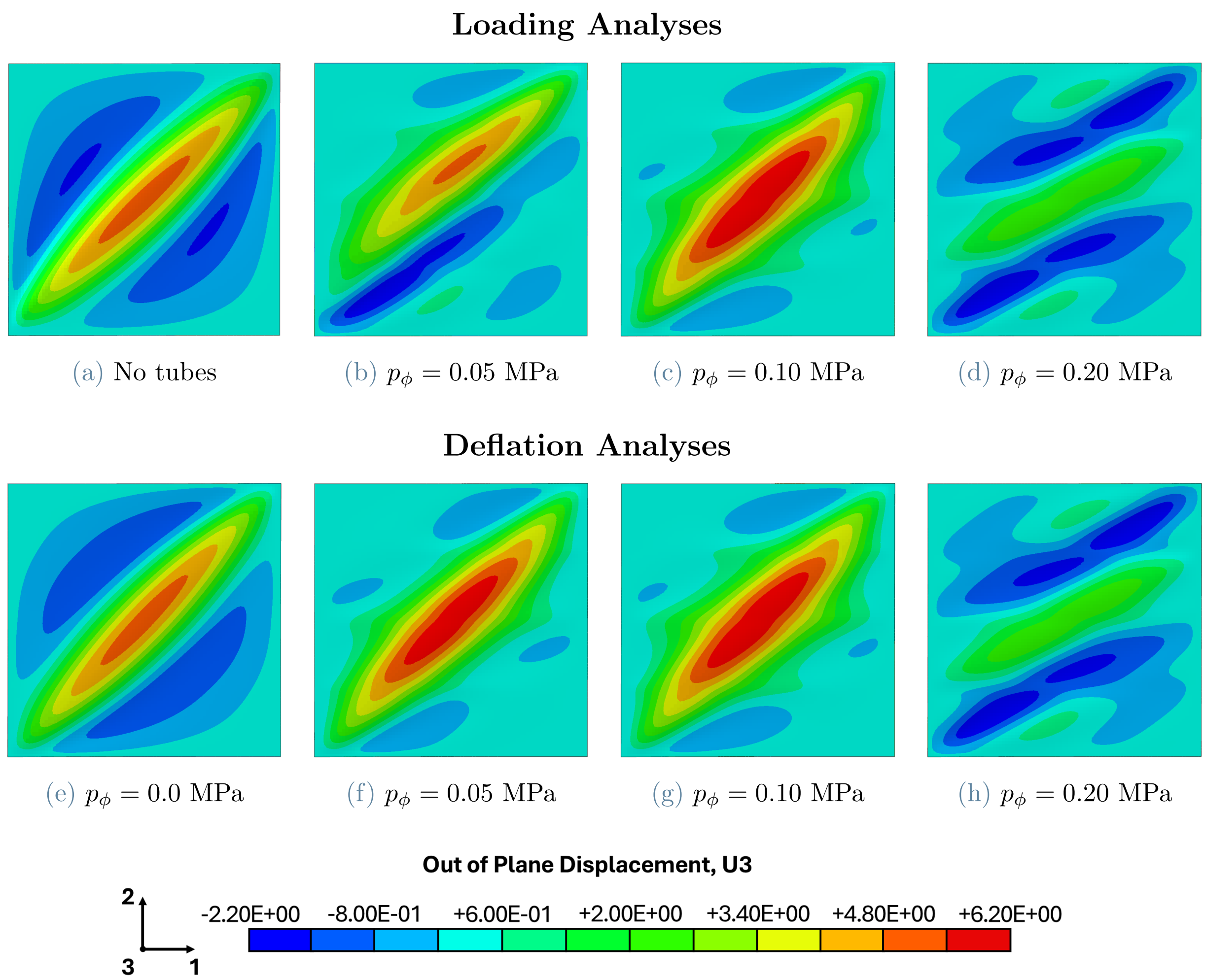

Figure 4.24: `3T OS`: Comparison of buckling shapes between the Loading Analyses and Deflation Analysis.

The Deflation Analysis also provides interesting results regarding the control of the buckling shape by adjusting the pressure. The buckling transition happening between $p_\phi = 0.10$ MPa and $p_\phi = 0.20$ MPa produces a jump of 4 mm in the out of plane displacement, the largest and most evident so far. Furthermore, due to the symmetry of the configuration, this feature would appear regardless of the direction of the shear load. The displacement along the center line of the panel, during the deflation, is shown in Figure 4.25. The jump between $p_\phi = 0.10$ MPa and $p_\phi = 0.20$ MPa is immediately noticeable. As the pressure is reduced further, the magnitude of the main buckle slightly decreases and two smaller external wrinkles begin to appear.

In conclusion, the `OS` analyses showed that the three-tubes configuration can provide a

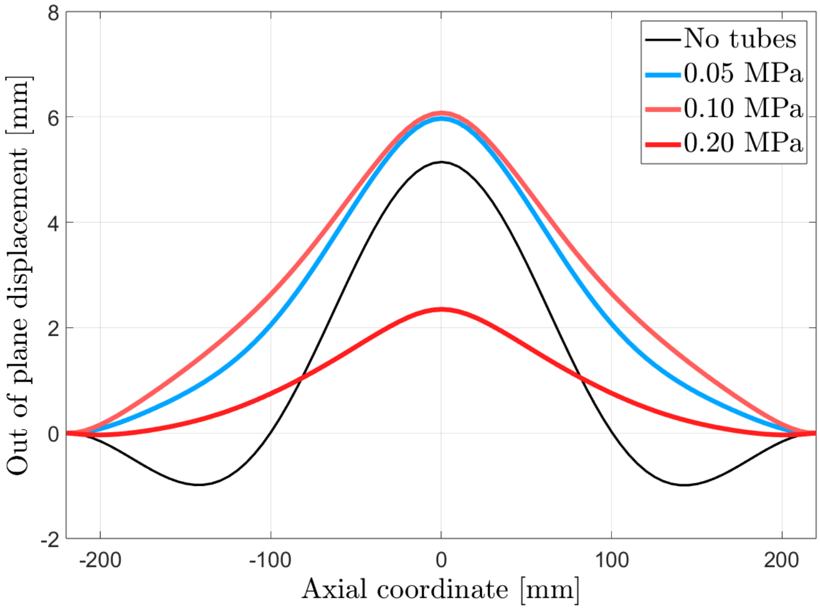

Figure 4.25: `3T 0S`: Displacements along the center line.

satisfying response to shear loads and, when inflated at high pressure, do not suffer large buckling transition. Also, by adjusting the inflation pressure, it is possible to obtain a buckling mode shift that can be implemented in future compliant mechanisms.

4.3.2. Shear: 1T 45S and 3T 45S

The 45S case is the first of the two shear load cases investigated for the models with tubes placed diagonally. In this case, the applied shear displacement acts parallel to the inflatable tubes. For this reason, both 1T 45S and 3T 45S cases do not bring any significant increase in the load bearing capabilities of the panel. Figure 4.26 shows that, except for a slight increase at the beginning of the Loading Step, the panel does not benefit from the inflatable tubes. Also, the three-tubes configuration does not provide any improvement to the structural response with respect to the single-tube configuration.

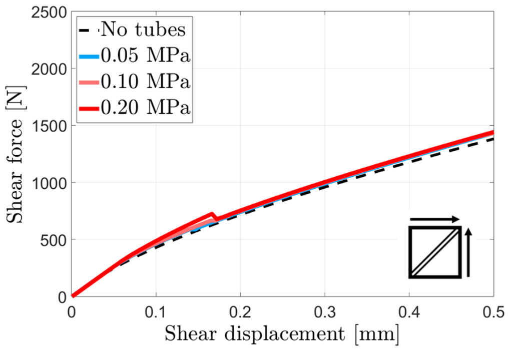

(a) 1T 45S

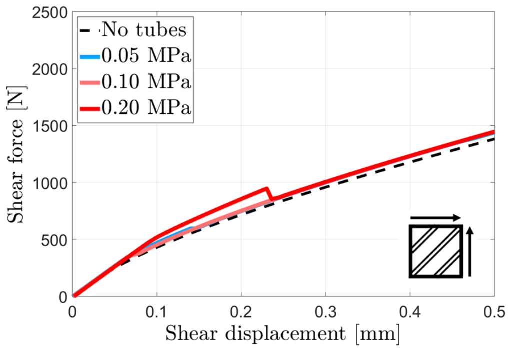

(b) 3T 45S

Figure 4.26: 45S: Load trends.

The main consequence of the inflatable elements is to split the buckling shape into two main buckles. Eventually, the tube gives in and the buckling affects the panel globally, resembling the shape of the unsupported configuration. However, such change in buckling shape is delayed as the inflation pressure increases. The only difference between the single-tube and the three-tubes configuration lies in ability of maintaining the buckling separated. As expected, the three-tubes configuration is able to delay the transition to global buckling. As shown in Figure 4.27, 3T 45S is able to maintain the buckling separated at $p_\phi = 0.10$ MPa; the single-tube configuration on the other hand has already suffered the transition to global buckling. However, this effect on the buckling behavior does not benefit in any way the load response of the panel.

1T 45S

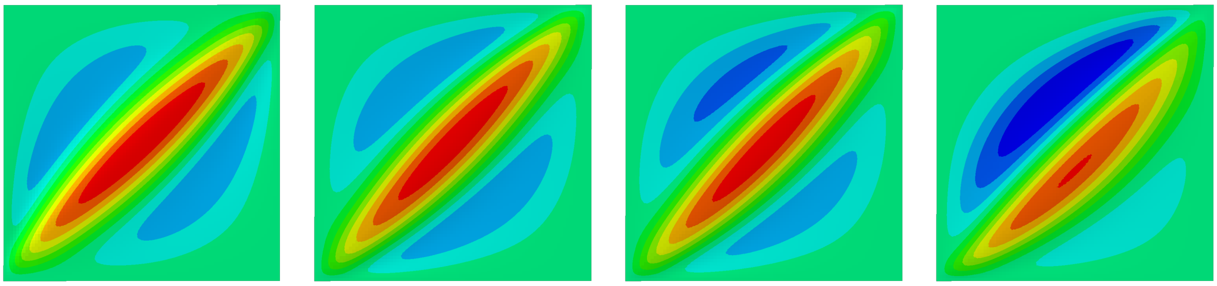

(a) No tubes (b) $p_\phi = 0.05$ MPa (c) $p_\phi = 0.10$ MPa (d) $p_\phi = 0.20$ MPa

3T 45S

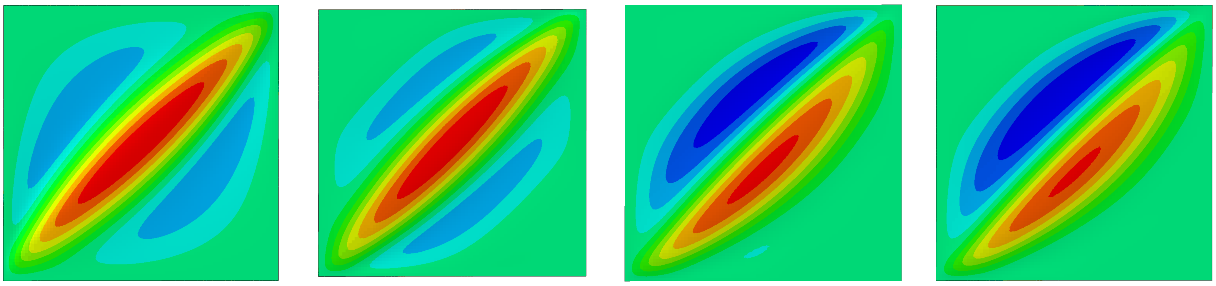

(e) No tubes (f) $p_\phi = 0.05$ MPa (g) $p_\phi = 0.10$ MPa (h) $p_\phi = 0.20$ MPa

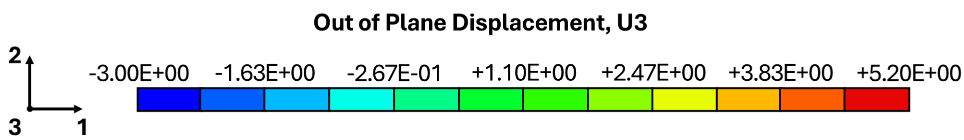

Figure 4.27: 45S: Buckling shape comparison.

4.3.3. Shear: `1T -45S` and `3T -45S`

The `-45S` cases show great potential and, overall, present the best performance amongst all shear load cases. The controlled shear displacement is applied perpendicularly to the tubes, meaning that the tubes provide the maximum support to the panel.

`1T -45S`

The load trends of `1T -45S` at the inflation pressures of interest are shown in Figure 4.28. The benefits introduced by the inflatable tube can be clearly seen; however, the structure

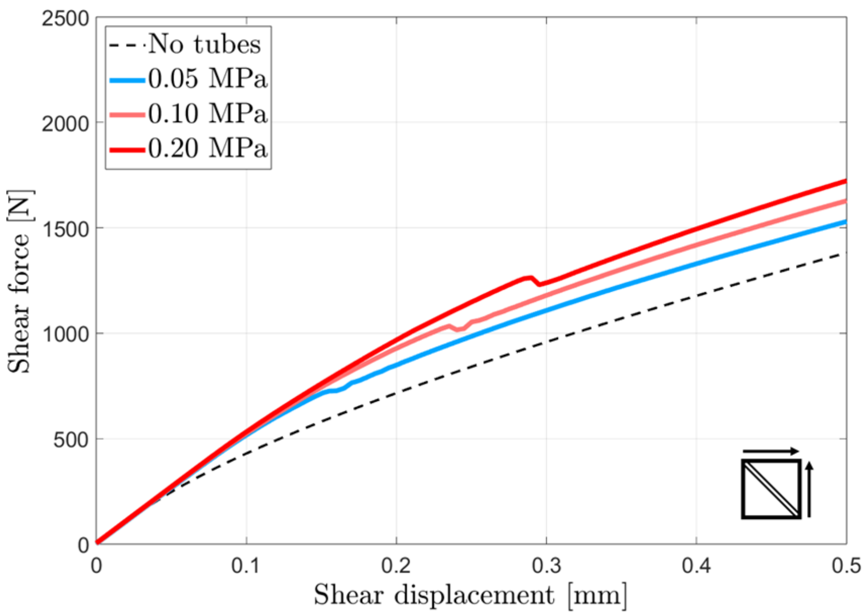

Figure 4.28: `1T -45S`: Load trends.

suffers from global buckling, regardless of the inflation pressure. The sudden buckling transition can be clearly seen in Figure 4.28, as the load trend suffers a slight drop when the buckles spread to the whole panel. Similarly to previous cases, the drop in performance is delayed as the inflation pressure grows. Unlike `1T 0S`, where the performance improvements of the panel stall at around $p_\phi = 0.10$ MPa, the inflation pressure here produces gradually increasing benefits.

Looking at the buckling shapes, shown in Figure 4.29, the deformation patterns are overall similar to the unsupported panel. The higher pressures produce a slightly larger central buckle. On the other hand, the two external buckles suffer a size reduction as the inflation pressure increases.

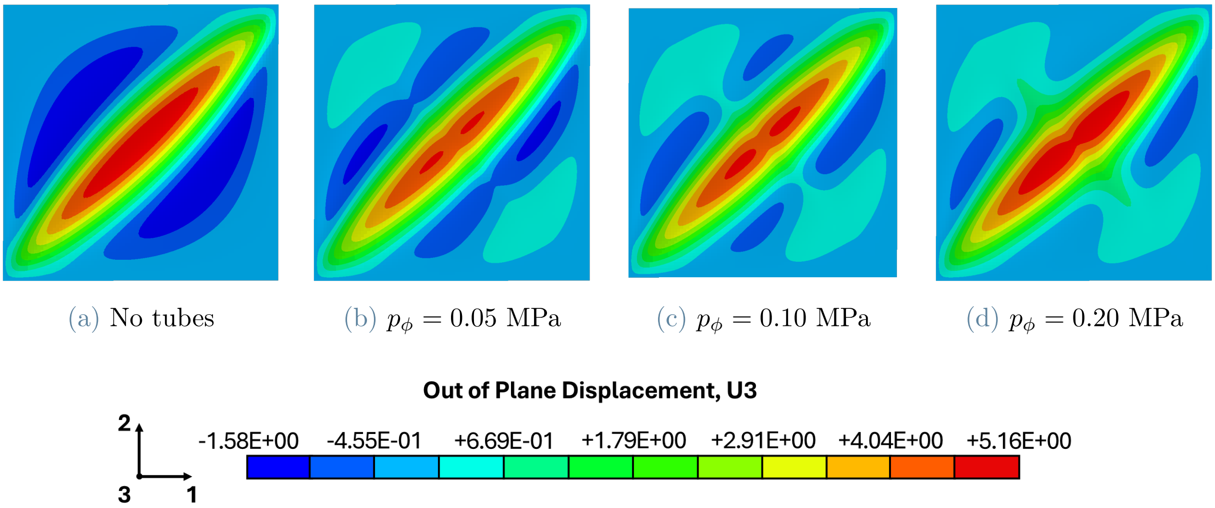

Figure 4.29: `1T -45S`: Deformed shapes.

`3T -45S`

The three-tubes configuration produces better results with respect to the single-tube counterpart, as shown in Figure 4.30. The overall stiffness of the panel increases and only when inflated at $p_\phi = 0.05$ MPa the structure undergoes a buckling transition, as shown by the drop in the load trend and subsequent oscillation. For $p_\phi = 0.10$ MPa and $p_\phi = 0.20$ MPa, the load trend is smooth, suggesting a gradual growth of the buckles without sudden changes.

The results reported in Table 4.5 show a gradual increase in the load bearing capabilities of the stiffened panels, especially at the higher pressures. When $p_\phi = 0.05$ MPa the buckling transition causes a slight reduction in the load increase, while for $p_\phi = 0.10$ MPa and $p_\phi = 0.20$ MPa, the load increase shows a positive trend throughout the test, while the percentage increase begins to diminish towards the end of the loading step.

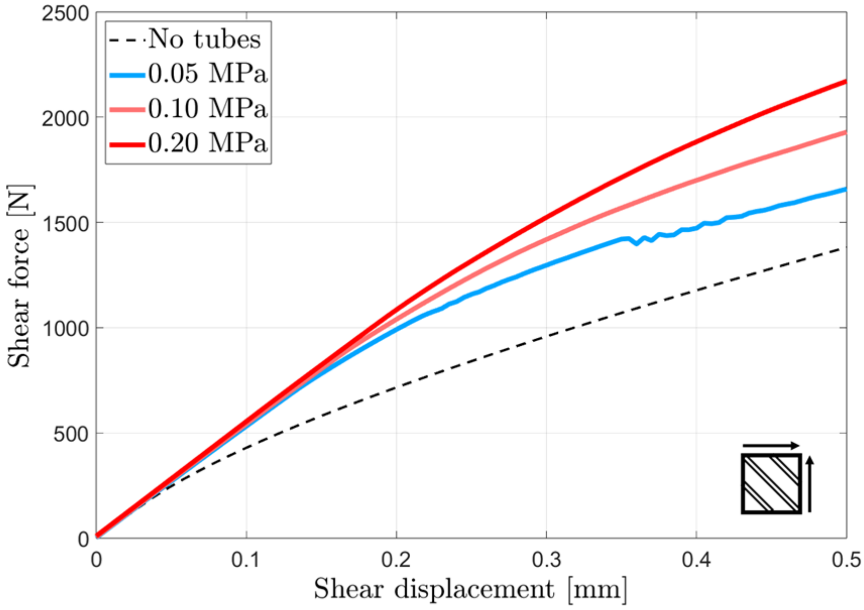

Figure 4.30: `3T -45S`: Load trends.

	Shear Disp. [mm]	0.1	0.2	0.3	0.4	0.5
No tubes	F_S [N]	429	716	958	1177	1382
$p_\phi = 0.05$ MPa	F_S [N]	532	992	1300	1473	1659
	ΔF_S [N]	103	276	342	296	277
	% Increase	24.0	38.5	35.7	25.1	20.0
$p_\phi = 0.10$ MPa	F_S [N]	542	1043	1419	1700	1929
	ΔF_S [N]	113	327	461	523	547
	% Increase	26.3	45.7	48.1	44.4	39.6
$p_\phi = 0.20$ MPa	F_S [N]	554	1085	1524	1883	2171
	ΔF_S [N]	125	369	566	706	789
	% Increase	29.1	51.5	59.1	60.0	57.1

Table 4.5: `3T -45S`: Shear load values.

The Deflation Analysis confirms the results obtained, as shown in Figure 4.31. A buckling transition can be noticed in between $p_\phi = 0.05$ MPa and $p_\phi = 0.10$ MPa, which is in agreement with the results obtained from the Loading Step. A slight discrepancy can be noted for $p_\phi = 0.05$ MPa, but can be attributed to the oscillation in the load trend.

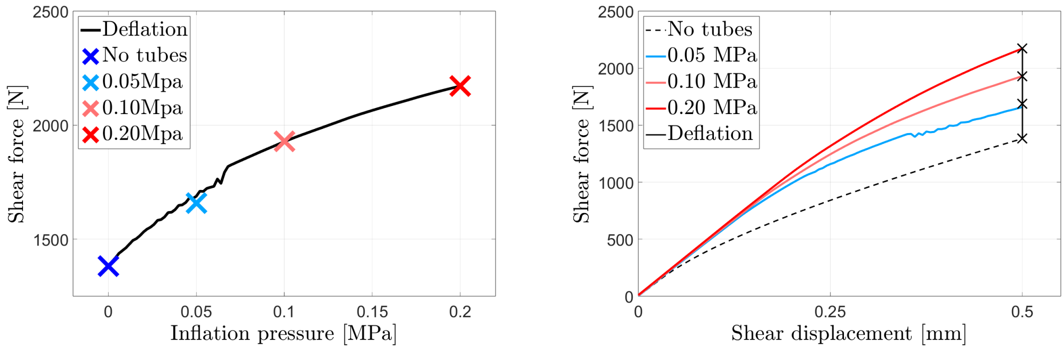

Figure 4.31: `3T -45S`: Deflation Analysis.

Figure 4.32 shows the deformed shapes of the panels obtained from both the Loading Analysis and the Deflation Analysis, at $U_S = 0.5$ mm When the tubes are inflated at higher pressures, the panel is affected by two buckles with negative U3; these buckles affects the beam less for $p_\phi = 0.20$ MPa, where a more evident separation of the bumps is noticeable. As the pressure decreases, the buckles expand over the beams but maintain a similar shape. When the pressure is $p_\phi = 0.05$ MPa, the structure has suffered a buckling transition. The deformation pattern from the Loading Analysis and the Deflation Analysis show a significant difference, as the former shows two buckles rising in opposite directions, while the latter resembles the shape of the panel without tubes. During the Deflation Analysis, the deformed shape was oscillating between different buckling states which could have caused such difference. Considering that the deformation pattern obtained in the Deflation Analysis at $p_\phi = 0.05$ MPa resembles that of the panel without tubes, it is reasonable to assume that the Deflation Analysis provides reliable results. Furthermore, the load response is matching, showing that any buckling shape discrepancy does not affect the structural response of the panel.

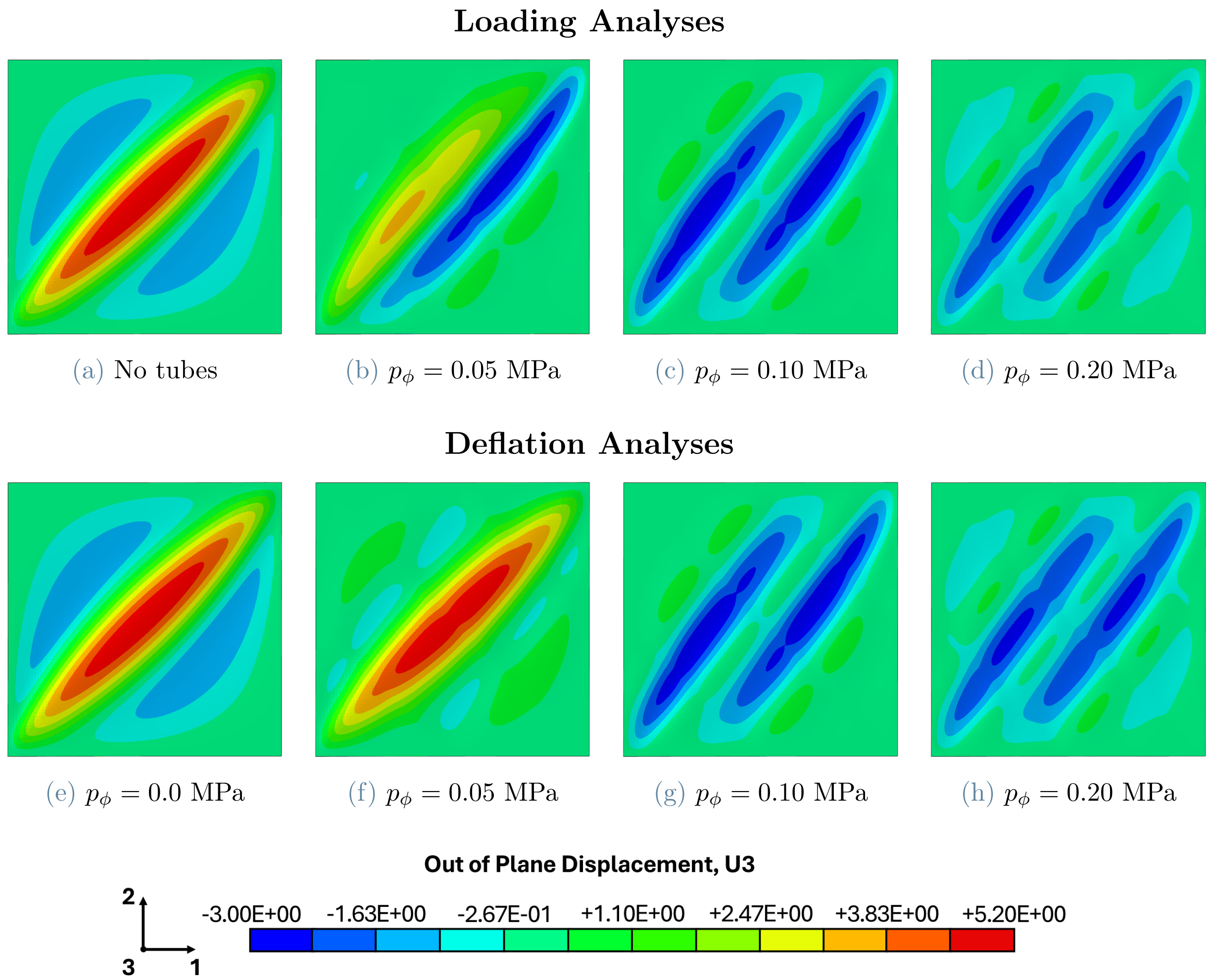

Figure 4.32: `3T -45S`: Comparison of buckling shapes between the Loading Analyses and Deflation Analysis.

This configuration is the most promising, amongst all the model investigated, to be implemented in a control system for morphing purposes. Figure 4.33 shows the out of plane displacement along the center line of the panel, at different pressures during the Deflation Analyses. By looking at the out of plane displacements, by controlling the inflation pressure it's possible to obtain a 5 mm range of motion in the center of the panel. This jump in the out of plane displacement is caused by the buckling transition happening around $p_\phi = 0.07$ MPa.

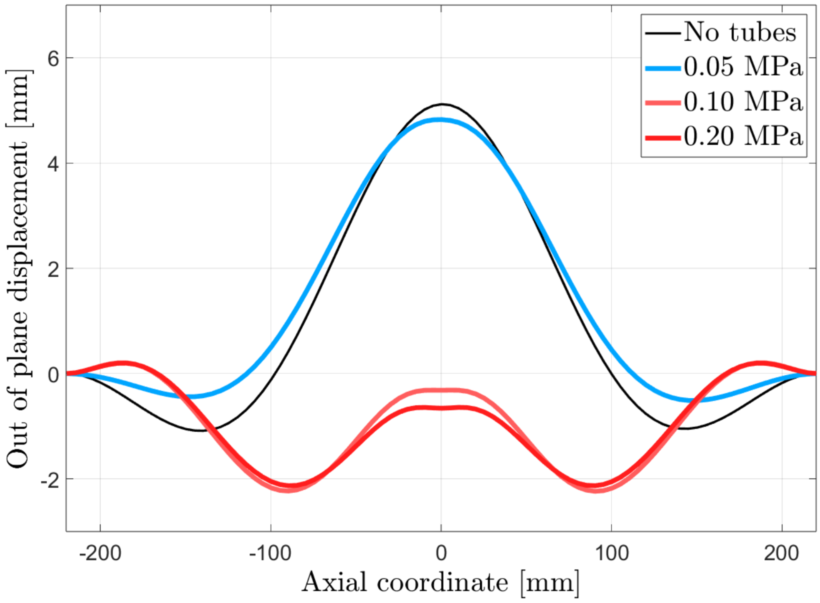

Figure 4.33: `3T -45S`: Displacements along the center line.

4.4. Comparison

The numerical computation presented in the previous sections proved that inflatable tubes could provide structural improvements when introduced as reinforcing elements in stiffened panels. Each configuration had its advantages and disadvantages. As expected, the three-tubes configurations provided the best results. The `3T 0` configuration performed better in compression however, when the same model was compressed in the opposite direction, resulting in the 90° configuration, every advantage would vanish. The configuration with diagonal tubes provided slight improvements in compression, no effect in the `45` placements, but shone in the `-45S` load case.

This paragraph compares the behavior of the compression and shear cases of the three-tubes configurations. The models investigated showed significant differences in the load response. `3T 0C` responded very well to compression in the beams' direction, but the behavior was disappointing when the compression was perpendicular to the tubes. On the other hand, `3T 45C` produced a mediocre increase in the general stiffness of the panel, without however being influenced by the load direction. The comparison between `3T 0C`, `3T 90C` and `3T 45C` is shown in Figure 4.34. The load response of `3T 45C` is massively lower than `3T 0C`: even at $p_\phi = 0.20$ MPa, the diagonal tubes model just slightly outperforms the 0° model at $p_\phi = 0.05$ MPa. The 0° and the 90° configurations are the same structure, just loaded in different directions; the poor results of `3T 90C` are surely an important downside of this beam layout but as it is later explained, the specific load scenario of `3T 90C` is not extremely common in aeronautical structures, thus advantaging the 0° and 90° model over the 45°.

At first, the shear response of the two configurations may seem similar. As shown in Figure 4.35, both `3T 0S` and `3T -45S` provided good results in terms of load bearing capability. However, although the stiffness increase was comparable, their behavior was significantly different. The slight advantage in the load response of `3T -45S` is immediately noticeable: the performance of this configuration is overall better than `3T 0S`. `3T -45S` also experienced a smoother development of the buckling and suffered fewer buckling transitions. The only buckling transition affected the model inflated at $p_\phi = 0.05$ MPa, however the event was significantly delayed with respect to the `3T 0` counterpart. For $p_\phi = 0.10$ MPa the buckles in `3T -45S` affected the tubes, but in `3T 0S` the buckling assumed global behavior. For $p_\phi = 0.20$ MPa, while in `3T 0S` a buckling transition had happened, in `3T -45S` the buckles were maintained localized.

Although these advantages in favor of `3T -45S`, two issues must be addressed. In the first place, the `3T -45S` configuration provides the best results only when loaded in one

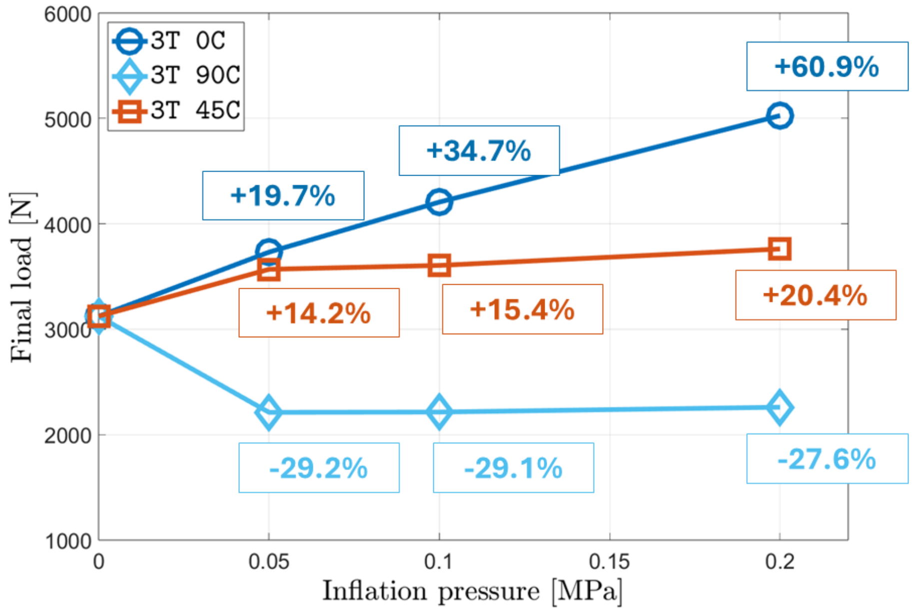

Figure 4.34: Compressive response - Comparison.

direction. If loaded in the opposite direction the improvements disappear completely, since it would essentially behave like the `3T 45S` case. The `3T 0S` case does not suffer this problem because, due to its symmetry with respect to both Direction 1 and Direction 2, its response to shear would be the same regardless of the direction of the applied displacement. Also, `3T 0C` provided significant benefits when loaded in compression, even though only in one direction.

In the perspective of employing such structures in a wing box, it must be taken into consideration that shear loads can affect the panel in both directions, when torsionally loaded for example. On the other hand, the direction of compression loads is more easily predictable as usually only the upper surface suffers big compression. The $0°$ configuration is not affected by the direction of the shear load and performs better under the ideal direction of the axial loads; thus being a preferable option in the perspective of further experimental work or more in-depth studies.

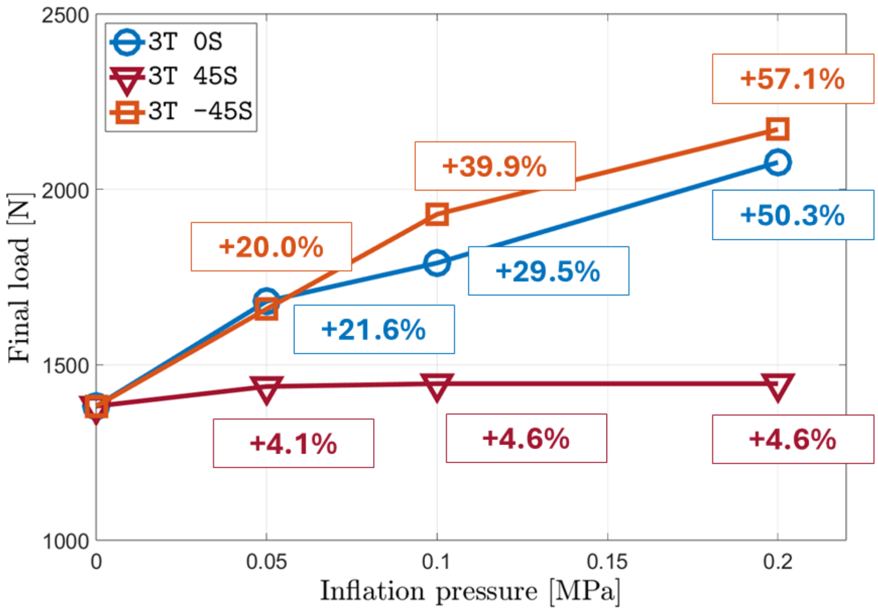

Figure 4.35: Shear response - Comparison.

5 | Pressure Modulation

The stiffening properties of inflatable tubes as reinforcing elements in panels were thoroughly discussed in the previous chapter. Inflatable structures carry the big advantage of being able to control such stiffness, by modulating the internal pressurization. The stiffness control of inflatable structures can be either active or passive. Active control requires the connection to a pneumatic system, thus allowing direct control of the pressurization of the inflatable element. Passive control is obtained by inflating and sealing the structure on the ground. The pressure differential variation with the external atmosphere, due to altitude changes, leads to stiffness modifications. There are several ways this property could be exploited. An example was already shown in Chapter 4, when the inflatable beams were deflated to verify the load response and the buckling shapes of the panels at different inflation pressures.

This chapter analyzes the effect of pressure modulation on the inflatable stiffened panel more in depth. Pressure modulation is extremely useful because it allows to control the load response of the panel and to obtain specific buckling states. For example, the pressure can vary during the loading process, allowing the panel to follow different load trends. Another example is the control of post-buckling in preloaded panels. This scenario is essentially the Deflation Analysis reported in Chapter 4, where the inflation pressure of the reinforcing inflatable tubes is modulated to control the load response and the buckling shape of the panel. The numerical computations are carried out on the same models presented in Chapter 3, on the `3T 0` configuration.

5.1. Pressure Modulation during Loading Step

The assessment of the Pressure Modulation during the Loading Step aims at understanding whether the panel can provide different structural responses while it's being loaded. The control of the load response would rely on the inflation pressure modulation. The investigation is based on numerical tests where the application of the controlled displacement is alternated to the variation of the inflation pressure. While the pressure is varying the applied displacement remains constant, and vice versa. The numerical analyses employ the `3T 0` model, presented in detail in Chapter 3. All three tubes are inflated or deflated simultaneously. The goal is to check whether varying the load response of the panel can be controlled by modulating the inflation pressure of the reinforcing tubes. Each modulation analysis is divided into six time steps, where the inflation pressure and the applied displacement are controlled. The effect of Pressure Modulation is assessed for inflatable stiffened panels loaded both in compression and shear.

Pressure Modulation during Compressive Loading

The Pressure Modulation analyses under compressive load are carried out with the same boundary conditions of the `3T 0C` configuration, presented in Section 3.2. The applied compressive displacement U_C pauses twice in order to allow the pressure modulation. When $U_C = 0.15$ mm and $U_C = 0.30$ mm, the compression of the panel momentarily stops and the pressure is changed. There are three modulation analyses:

- Modulation 1: the tubes are initially inflated at $p_\phi = 0.20$ MPa, then the compressive displacement begins to get applied on the panel. When $U_C = 0.20$ mm, the tubes are deflated down to $p_\phi = 0.10$ MPa; when $U_C = 0.40$ mm the tubes are further deflated to $p_\phi = 0.05$ MPa.
- Modulation 2: the tubes are initially inflated $p_\phi = 0.05$ MPa, then the compressive displacement begins to get applied on the panel. When $U_C = 0.20$ mm, the tubes are inflated to $p_\phi = 0.10$ MPa; when $U_C = 0.40$ mm the tubes are further inflated up to $p_\phi = 0.20$ MPa.

The compressive displacement trend is the same for both analyses. The sequence of the inflation pressure and the compressive applied displacement during the time steps is reported in Figure 5.1.

The results provide an interesting insight into the effect of the inflatable tubes on post-buckled panels. Modulation 1 is able to follow the reference load trends, while Modulation 2 underperforms. The root cause of this issue can be found in the buckling state of the panel.

The previous chapter showed that a buckling transition can be initiated in two ways: by increasing the controlled displacement on an inflatable panel whose tubes are maintained at constant pressure, or by deflating the tubes on a preloaded panel with fixed controlled displacements. However, it was not studied whether the inflatable stiffened panel could reverse its buckling state by inflating the tubes back to the initial pressure. The Pressure Modulation analyses show that the behavior of the inflatable stiffened panel varies whether

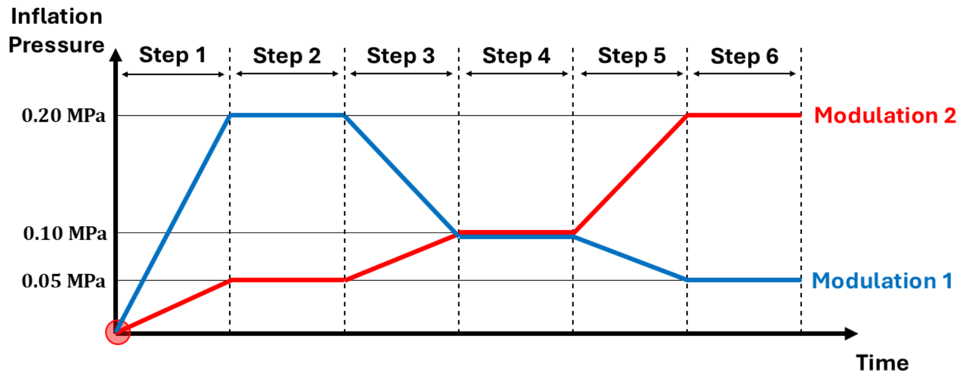

(a) Pressure sequence

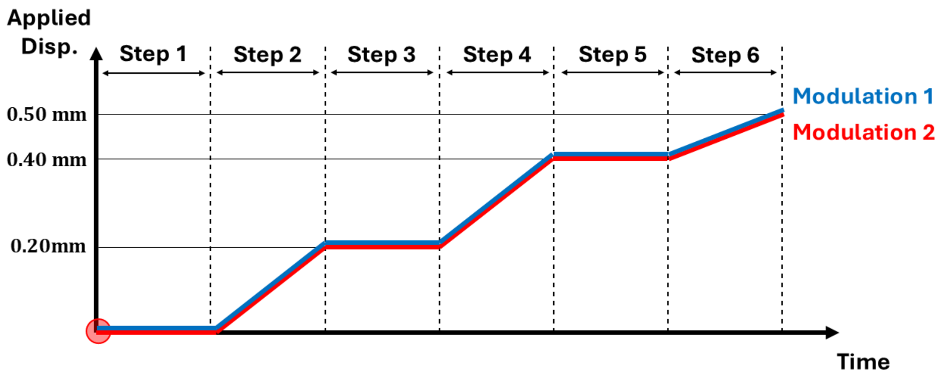

(b) Displacement sequence

Figure 5.1: Compression: modulation sequences.

the tubes are inflated or deflated, at a fixed applied displacement. Let's call state A the current buckling mode of the panel, and state B the new buckling mode of the panel obtained after a transition. When the panel is in a fixed preloaded state, the transition from state A to state B obtained through the deflation happens at a lower pressure with respect to the same transition from State B to State A obtained by inflating the tubes back. In other words, in order to transition the panel back to its previous buckling mode, the tubes must be inflated at a higher pressure.

The load trend of Modulation 1 is reported in Figure 5.2 and is compared with the load trends obtained from the `3T 0C` analyses. The highlighted points indicate the stages of the Modulation from which the deformed shapes reported in Figure 5.3 are taken. Modulation 1 is able to follow the load trends provided by the Loading Analyses. It suffers only one buckling transition, during the application of the displacement from B to C. The further reduction of inflation pressure increases the amplitude of the buckles but does not cause a change in the buckling mode.

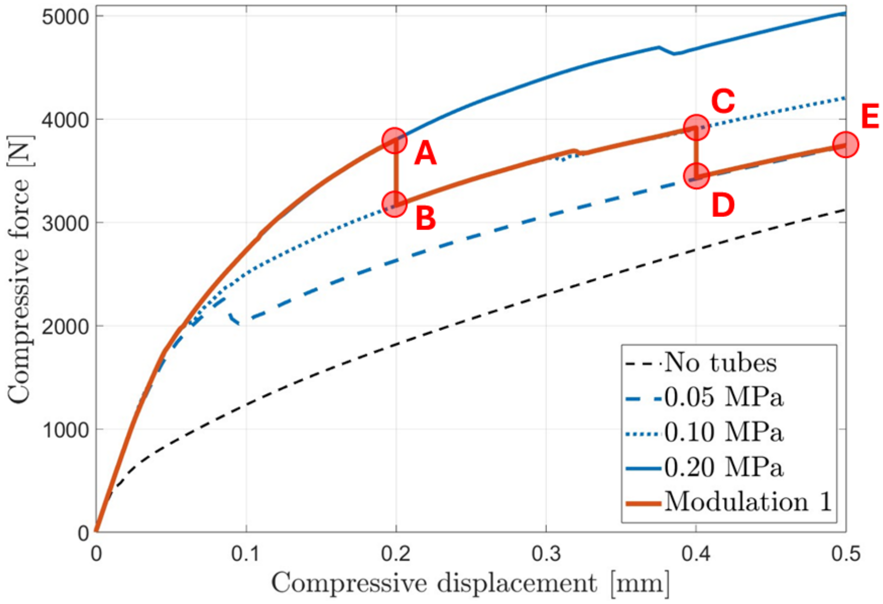

Figure 5.2: Compression: Modulation 1.

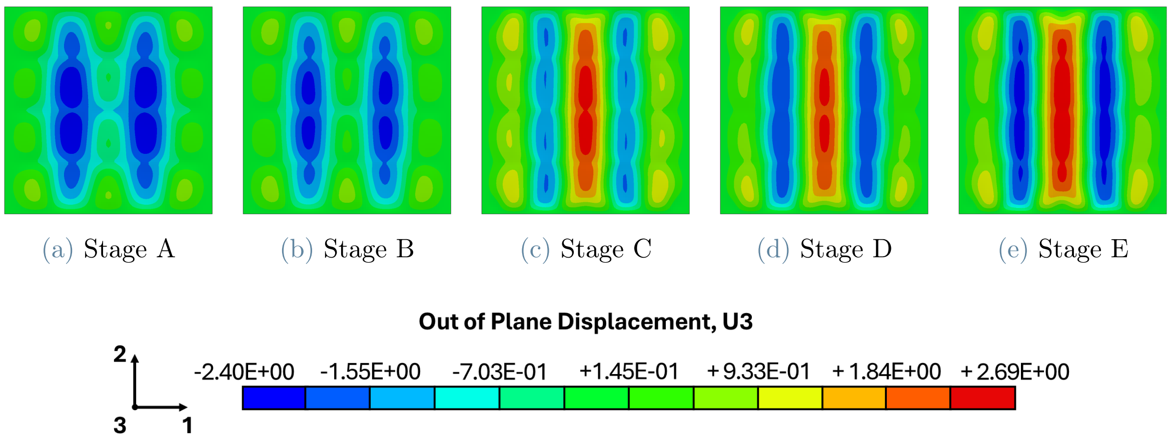

(a) Stage A (b) Stage B (c) Stage C (d) Stage D (e) Stage E

Figure 5.3: Compression: Buckling modes during Modulation 1.

The load trend of Modulation 2 is reported in Figure 5.4. The panel initially suffers a buckling transition, when inflated at $p_\phi = 0.05$ MPa. After the inflation from 0.05 MPa to 0.10 MPa, the load response of the panel is lower with respect to the reference curve at $p_\phi = 0.10$ MPa. The buckled shape of the panel in Modulation 2, between point B and C, reduces the load bearing capabilities with respect to the reference curve. The panel in Modulation 2 suffers one buckling transition but it is not able to reverse it when inflated to 0.10 MPa, where the reference panel has not transitioned yet. This difference is evened once the reference curve suffers a buckling transition itself; after this event the two analysis provide similar results. This behavior suggests that, once a buckling transition is occurred, inflating the panel to a pressure where normally would not be in a buckled state may not reverse the transition. When Modulation 2 is inflated up to 0.20 MPa, it is still not able to reach the reference load trend. Figure 5.5 presents the deformed shapes of Modulation 2 in the stages of the analysis highlighted in Figure 5.4. The deformation pattern throughout the Modulation Analysis is influenced by the buckling mode obtained after the first transition.

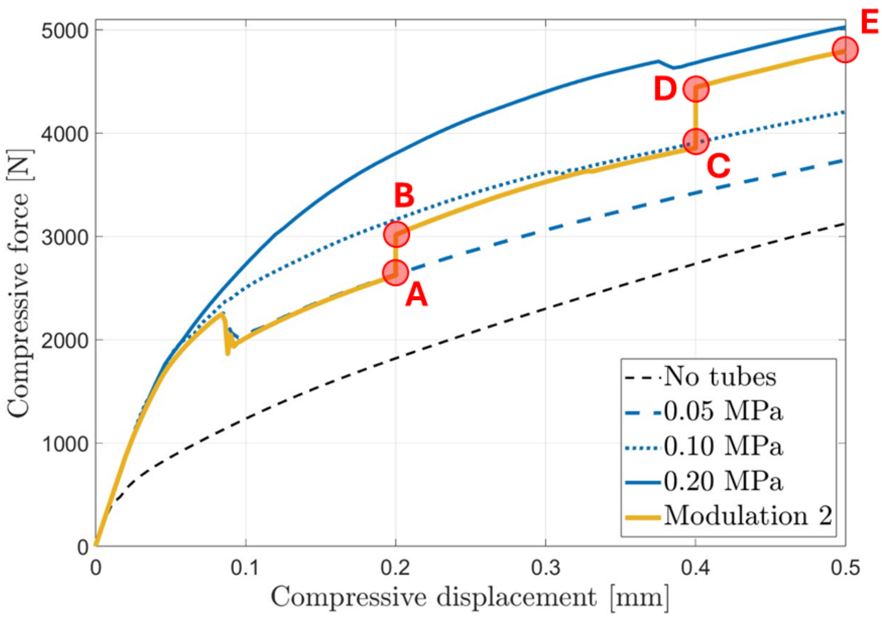

Figure 5.4: Compression: Modulation 2.

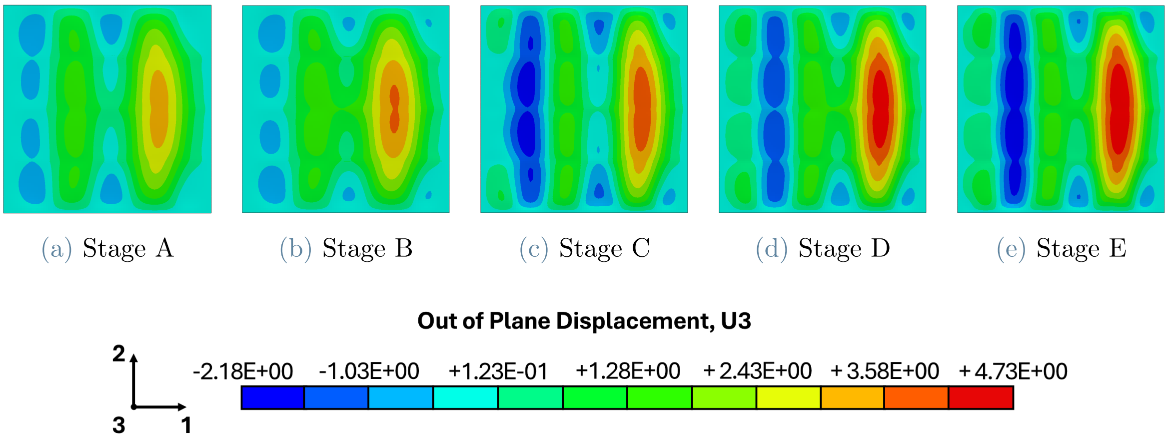

(a) Stage A (b) Stage B (c) Stage C (d) Stage D (e) Stage E

Figure 5.5: Compression: Buckling modes during Modulation 1.

Pressure Modulation during Shear Loading

The Pressure Modulation under shear loading spaces through the load trends obtained from the `3T 0S` case. The applied shear displacement reaches a value of $U_S = 0.5$ mm, but pauses twice to allow the change of pressure. The reference load responses for the `3T 0S` tests are not significantly influenced by the inflation pressure at the beginning of the Loading Step, as was shown in Figure 4.20. In order to verify the effects of the pressure modulation, any inflation or deflation is carried out towards the end of the loading process, when $U_S = 0.3$ mm and $U_S = 0.45$ mm. There are two Pressure Modulation Analyses, still divided into six time steps; the applied displacement and pressure sequence of each modulation is reported in Figure 5.6.

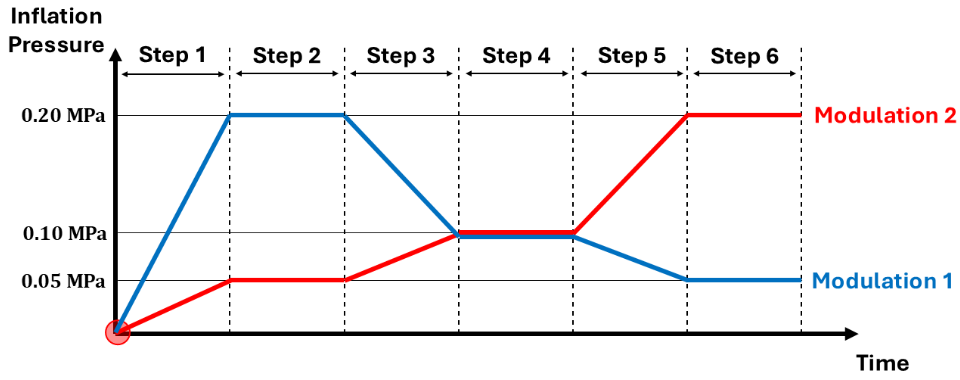

(a) Pressure sequence

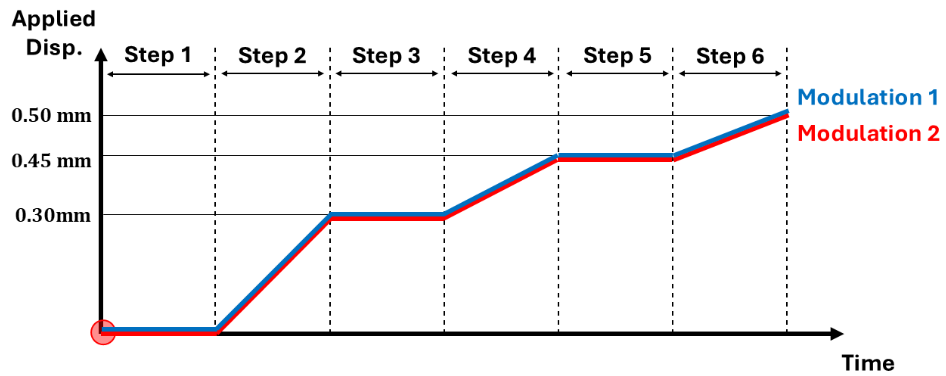

(b) Displacement sequence

Figure 5.6: Shear: modulation sequences.

The Modulation Analyses under shear loading show similar results to the compression cases. The load trend of Modulation 1 is reported in Figure 5.7. The panel is able to follow the load trend of the reference curves obtained from the `3T OS` Loading Analyses. The deformed shapes of the panel during Modulation 1, in the stages highlighted in Figure 5.7, are reported in Figure 5.8.

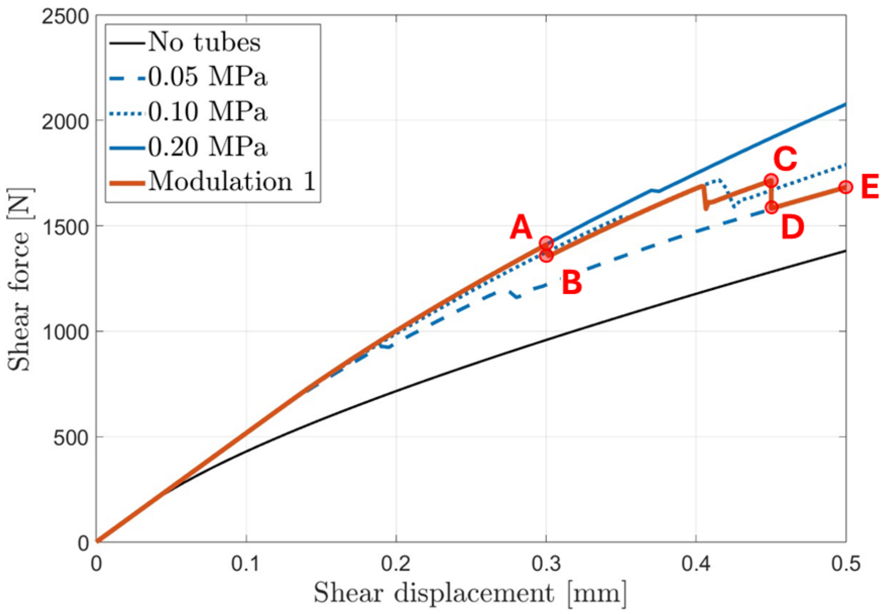

Figure 5.7: Shear: Modulation 1.

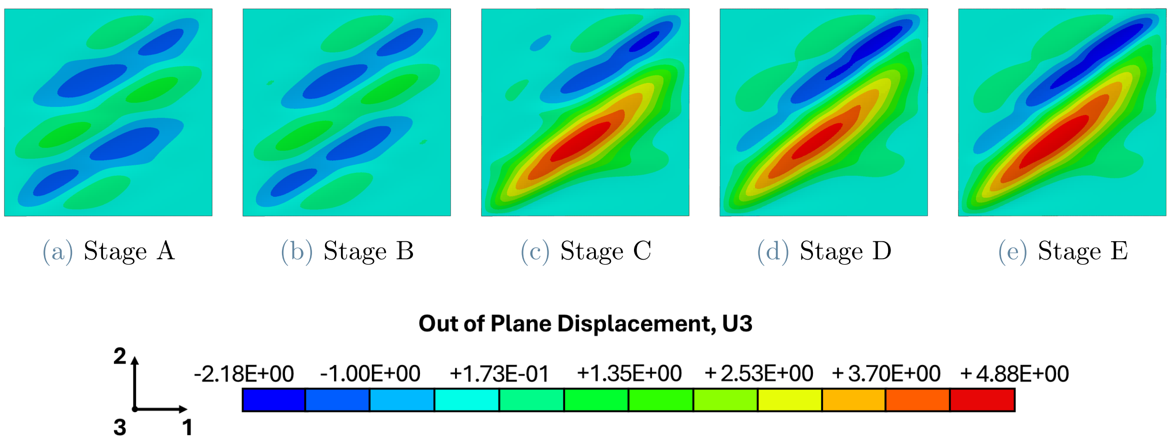

(a) Stage A (b) Stage B (c) Stage C (d) Stage D (e) Stage E

Figure 5.8: Shear: Buckling modes during Modulation 1.

The load trend of Modulation 2 is shown in Figure 5.9. After the inflation at $U_S =$ 0.30 mm, the panel in Modulation 2 presents a worse load response with respect to the reference curve. At this stage of the Modulation Analysis, the panel has suffered two buckling transitions and the increase in pressure to 0.10 MPa is not able to reverse them, thus reducing its load bearing capabilities. The reference panel inflated at $p_\phi = 0.10$ MPa has yet to transition and presents a better load response. After the inflation at $U_S =$ 0.45 mm, from 0.10 MPa to 0.20 MPa, the panel in the Modulation Analysis is not able to match the reference curve. The sequence of deformed shapes of the panel during Modulation 2 is reported in Figure 5.10. Unlike Modulation 1, where in Stage A and B the buckles were localized around the tubes, here the panel deformation pattern obtained from the initial buckling transition is maintained throughout the analysis.

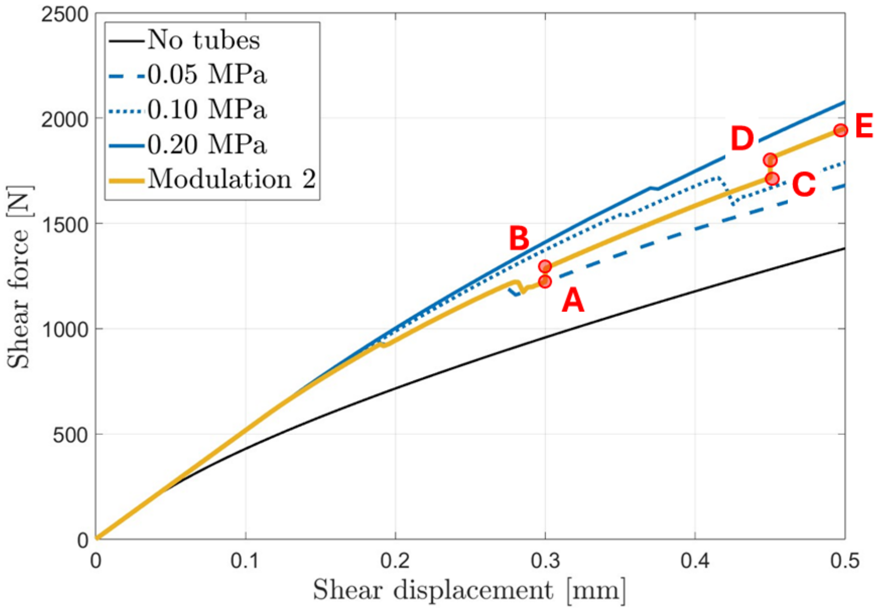

Figure 5.9: Shear: Modulation 2.

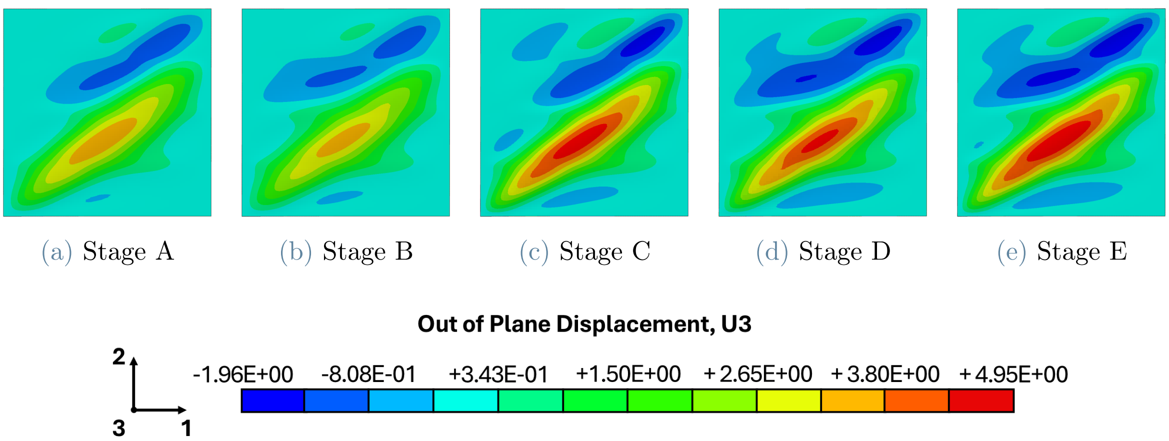

(a) Stage A (b) Stage B (c) Stage C (d) Stage D (e) Stage E

Figure 5.10: Shear: Buckling modes during Modulation 2.

5.2. Partial Pressure Modulation (PPM)

The previous section investigated the effect of the pressure modulation during the loading process by acting on all three tubes simultaneously. Now, the analyses focus on the behavior of the stiffened panel when only one or two tubes are totally deflated, while the remaining are kept at constant pressure. The load on the panel is kept constant during the Partial Pressure Modulations. The Pressure Modulation analyses begin with the prestressed panel obtained from the `3T 0C` and `3T 0S` configurations, at the end of the Loading Step.

The goal of this section is to assess how the position of the deflated tubes can affect the load trend and the buckling shape of the stiffened panels. The study takes into account five Pressure Modulations, deflating the tubes in different patterns. The deflation of all three inflatable elements is one of the five cases; it was already presented in Chapter 4 but the results are reported again for the purpose of comparison. To ease the comprehension of each analysis, the tubes are numbered as shown in Figure 5.11 and each Pressure Modulation Analysis is labeled as in Table 5.1. Each label refers to the tubes deflated in the respective Pressure Modulation Analysis. The initial pressure is $p_\phi = 0.20$ MPa for all three tubes, the final pressure is $p_\phi = 0.0$ MPa for the deflated tubes.

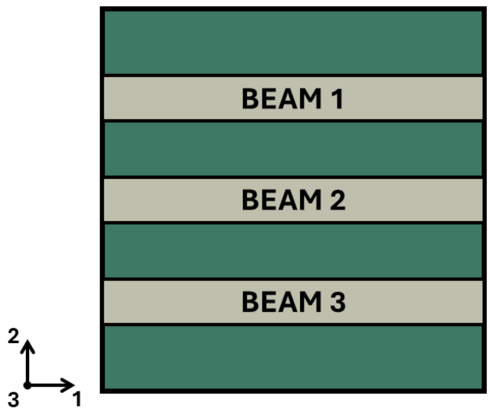

Figure 5.11: Pressure and applied displacement sequence.

The five Pressure Modulation analyses are conducted both for compression and shear preloaded panels. The preloaded state of the panel is obtained from the end of the loading step of the `3T 0C` and `3T 0S` load case at $p_\phi = 0.20$ MPa, for compression and shear

Label	Deflated beam
`PM-1`	Beam 1
`PM-2`	Beam 2
`PM-12`	Beam 1, Beam 2
`PM-13`	Beam 1, Beam 3
`PM-123`	Beam 1, Beam 2, Beam 3

Table 5.1: Pressure Modulation Cases.

respectively. For the precompressed panel, $U_C = 0.5$ mm is maintained on the structure for the entirety of the Pressure Modulation. The same is true for the computations under shear preload, where $U_S = 0.5$ mm throughout the whole process. The complete set of boundary conditions was already reported in Section 3.2.

PPM: Compressive Preload

The first results presented are the Partial Pressure Modulations on the precompressed panel at $U_C = 0.5$ mm. The load range during the deflations is wider when more tubes are deflated. An interesting property of the panels is that the load response is only affected by the number of tubes deflated, and not by their position. Figure 5.12 shows how the load trends of `PM-1` and `PM-2`, as well as `PM-12` and `PM-13` are almost completely overlapping. The buckling transitions, caused by the loss of stiffness due to the deflation, are located between $p_\phi = 0.15$ MPa and $p_\phi = 0.20$ MPa.

The buckling shape of the panels after the Pressure Modulations are shown in Figure 5.13. The deformation pattern is highly influenced from the asymmetric initial state of the panel. The `PM-1` and `PM-12` show that the buckles shifted towards the unsupported portion of the panel. In `PM-1` the wrinkles are affected by the still inflated Beam 2, while in `PM-12` they present more elongated and widespread shapes. In `PM-2`, the buckles expanded over the central area of the panel.

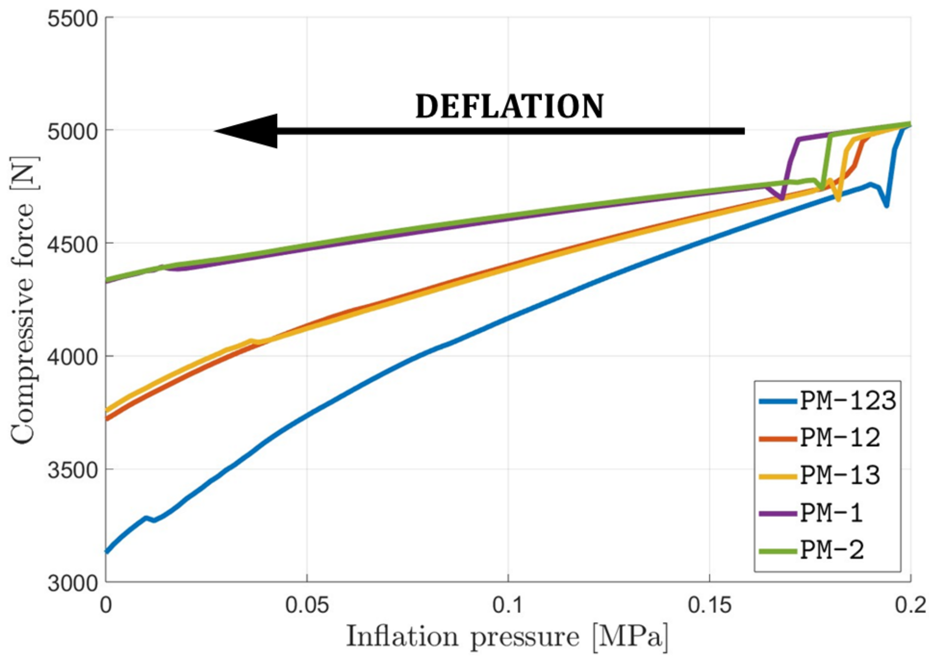

Figure 5.12: Compression: PPM results.

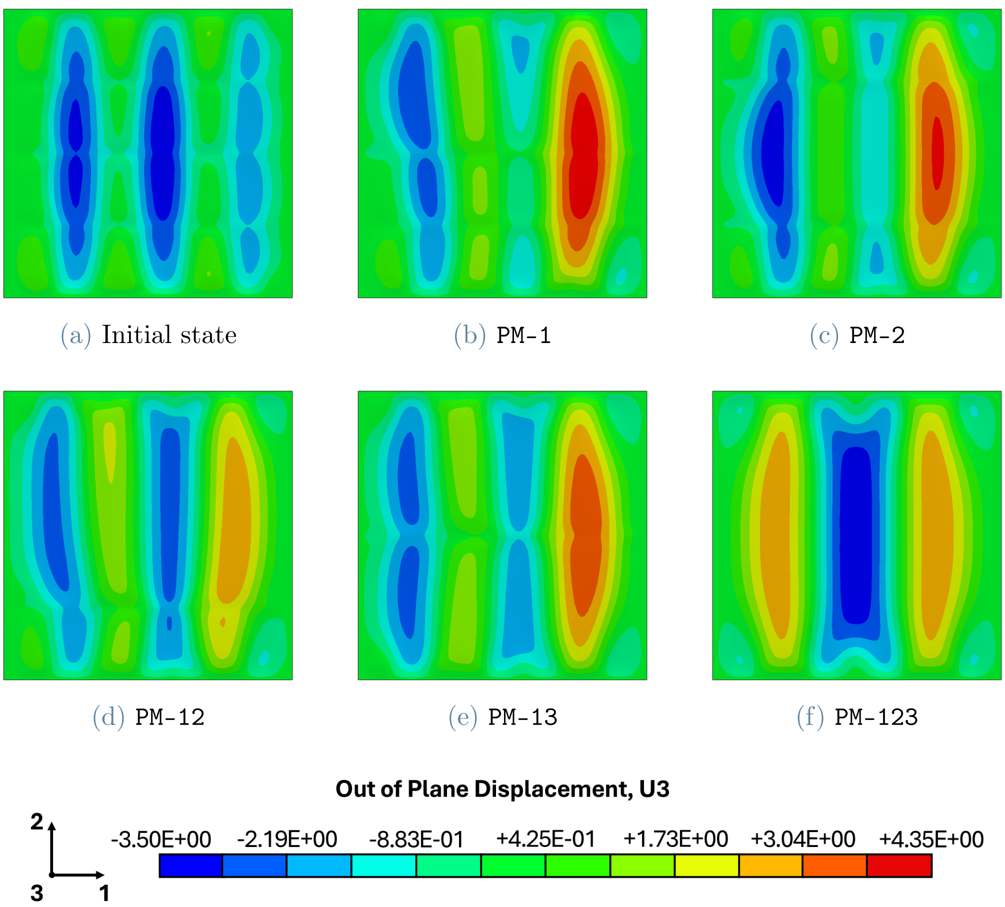

Figure 5.13: Compression: PPM deformation patterns.

The Partial Pressure Modulation `PM-13` sets the panel in the same configuration investigated in the `1T 0C` load case inflated at $p_\phi = 0.20$ MPa, presented in Section 4.2.1. The load response from the two analyses can be compared to verify the correct behavior of the panel. The compressive force at the end of `PM-13` is $F_C = 3756$ N, while the load provided by `1T 0C` is $F_C = 3777$ N. The difference is approximately 0.6%. Figure 5.14 compares the deformation pattern of the two analyses mentioned above. They both present four buckles, of which two with larger displacements. In `PM-13` the larger buckles are towards the sides, while in `1T 0C` are located in the center. The maximum out of plane displacement, both in positive and negative Direction 3, is similar.

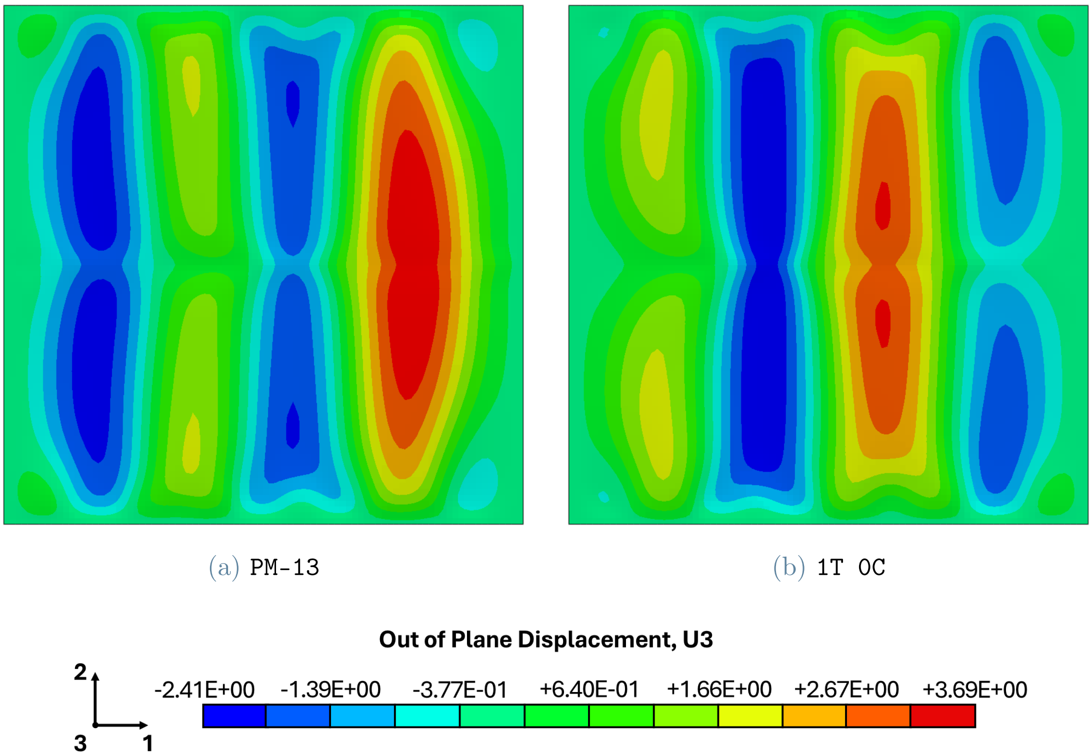

Figure 5.14: Comparison between PPM and single-tube loading analysis.

PPM: Shear Preload

The load response of the Partial Pressure Modulations under shear preload is shown in Figure 5.15. At the end of the deflation, when the pressure is $p_\phi = 0.0$ MPa, the percentage difference in load values between `B12` and `B13` is 0.21%, while for `B1` and `B2` is 1.42%. The load trends are not overlapping anymore, like in the precompressed panel, but the final shear force is the same. This means that, regardless of the load trend followed during the deflation, the load bearing capabilities at the end of the analyses are influenced by the amount of elements deflated, but not by the position of those tubes.

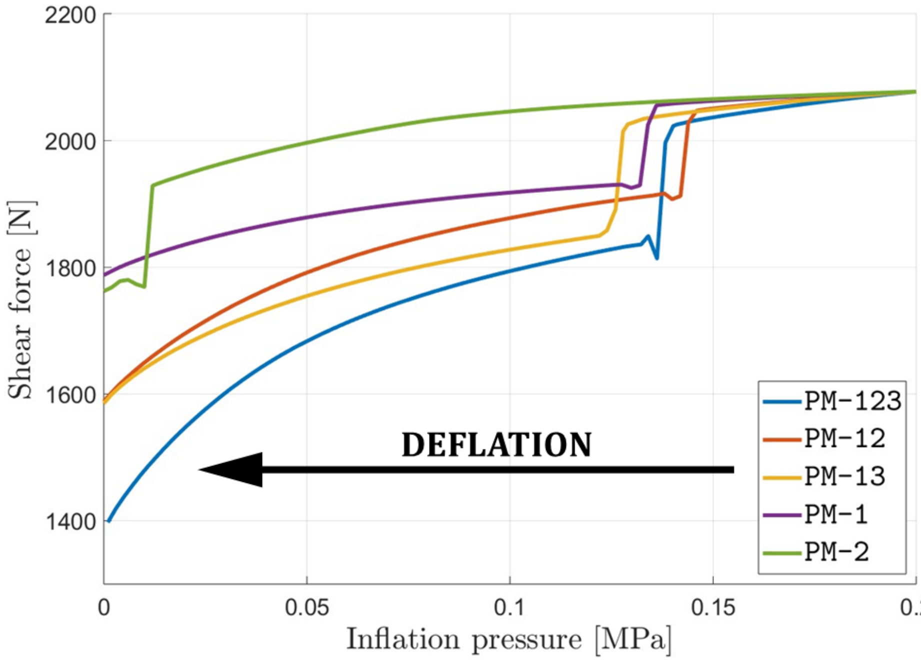

Figure 5.15: Shear: PPM results.

The buckling shape of `PM-1` and `PM-12` is of particular interest, because by deflating the tubes on the sides of the panel it is possible to induce buckling in that area. The deformation patterns at the end of deflation `PM-1` and `PM-12` are shown in Figure 5.16. Both `PM-1` and `PM-12` are affected by a large buckle with positive U3; in `PM-1` the effect of Beam 2 is visible because it maintains the remain buckles isolated. In `PM-12`, a second large buckle affects the portion of the panel where the tubes are deflated. Beam 3 is still able to create a slight separation in this second buckle.

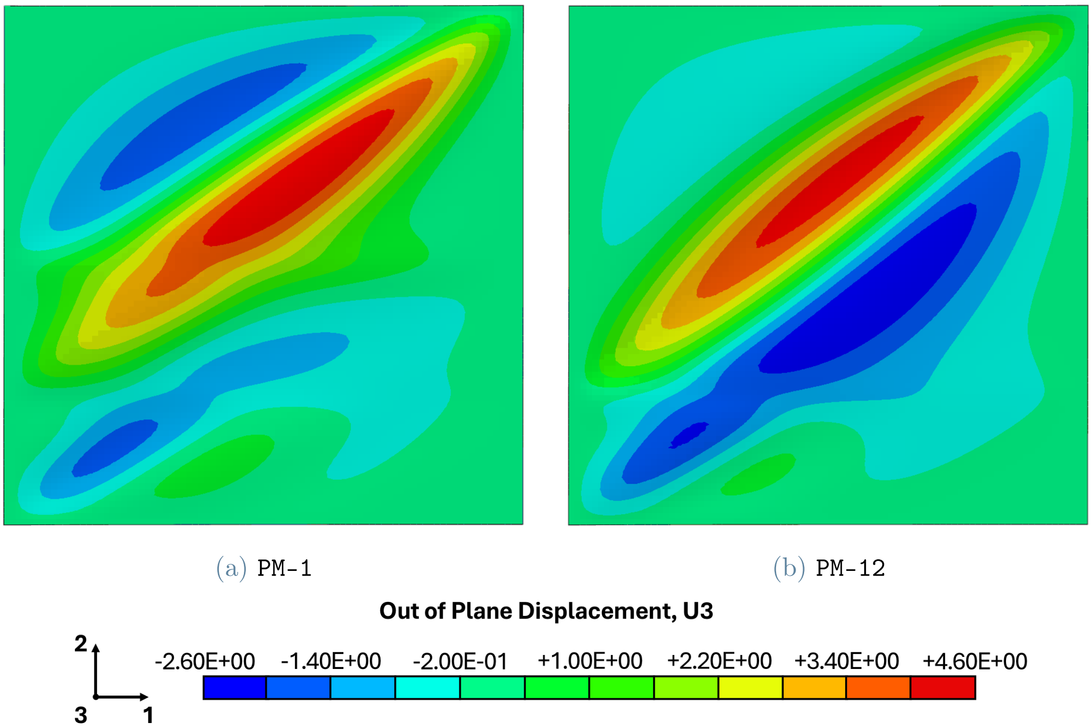

Figure 5.16: Deformation pattern after B1 and B12 deflation.

6 | Adaptive Flap with Post-Buckled Precompressed Inflatable Actuator

The previous chapters presented the structural improvements that inflatable tubes can introduce as reinforcing elements in panels. The out of plane displacement of the panel could be controlled and, in the best-case scenario, a total deflation of the tubes provided a 5 mm displacement. Inflatable tubes can be implemented in a more flexible design to obtain large displacements.

A Post-Buckled Precompressed (PBP) actuator is a type of actuator that exploits the buckling of a plate to obtain large deformations. The design of a PBP actuator was already presented by Vos et al. [36] and consists of a plate constrained on one side to the wing box and on the other side to the tip of the surfaces of an adaptive flap. The flap surfaces are stretched when connected to the PBP actuator, thus providing a compressive preload on the plate. The actuator is controlled through its buckling, which deforms the flexible flap surfaces. The buckling of the actuator could be initiated by controlling just a fraction of the buckling load, since most of the force is provided by the flap surfaces compressing the device. The design presented by Vos et al. [36] employs a piezoelectric element to deliver the extra compressive load required to initiate the buckling of the plate.

A numerical study on a Post-Buckled Precompressed Inflatable (PBP-I) actuator is here presented. The PBP-I actuator, instead of employing a piezoelectric element to control the buckling response of the panel, is controlled by the inflation and deflation of inflatable tubes. The actuator can be implemented in an adaptive flap, whose surfaces provides a precompression. By increasing the pressure of the inflatable tubes, the panel is compressed and buckles, deploying the flap.

6.1. Flap and PBP-I Actuator: Modeling

In this section, a PBP-I actuator is modeled and implemented in an adaptive flap. The model is composed of two main elements: the actuator consisting of a composite panel stiffened with inflatable tubes, and the flap surfaces made of pre-stretched rubber sheets. The design of the flap and its working mechanism resemble that presented by Vos et al. [36] but differs in the activation method: instead of employing a piezoelectric element, the buckling is initiated by compressing the actuator through the inflation of the tubes. When the tubes are inflated, they produce a compressive stress state on the panel which, amplified by the compressive force provided by the stretched skin, results in the buckling of the actuator.

6.1.1. PBP-I Actuator: Geometry

The actuator is a composite plate reinforced by three inflatable tubes for half of its length. The tubes, which are all on the same side of the panel, do not extend further to avoid contact with the upper surface when the flap is activated. Two of the three tubes are placed on the edges of the panel, while the third along the center line.

Each tube is 350 mm long, the radius is 10 mm and the thickness is 1 mm. The choice of the tube material can influence the behavior of the actuator. Using a stiff fabric reduces the tube deformation, thus not transferring enough displacement to the panel to initiate the buckling. On the other hand, using a fabric that is too flexible can reduce the overall stiffness of the actuator, expand too much and touch the flap surfaces or break due to the stress at higher pressures. For this reason, the choice of the material of the tube is changed from previous analyses. There are several materials suitable for this application, mainly elastomeric polymers like polyurethane (PU), thermoplastic polyurethane (TPU), reinforced composite rubbers and flexible polyvinyl chloride (PVC). The Young modulus and Poisson ratio can vary between materials and manufacturers: the Young modulus in elastomeric polymers can range from few MPa up to thousands [18, 40], TPUs can reach up to 90 MPa [41], composite rubber is dependent on the lay-up and reinforcement materials and can go from 10 MPa up to hundreds [42–44]. The material properties, reported in Table 6.1, are chosen between the range of values presented.

The second element of the PBP-I actuator is a 100 mm wide and 700 mm long composite plate. The plate is divided into two sections, called front plate and back plate: the front plate is the section that buckles as a result of the pressurization of the tubes. The front plate is reinforced by the tubes and is composed of 16 IM7-8552 plies, with a total

Material properties	
Thickness, h	1 mm
Young Modulus, E	100 MPa
Poisson's Ratio, ν	0.3
Density, ρ	1×10^{-6} kg/mm^3

Table 6.1: Material properties of the tube.

thickness of 2 mm. The ply lay-up of this part of the plate is $[0/90]_{4S}$. To transfer the rotation to the trailing edge, the back plate must be as rigid as possible; for this reason, the thickness is increased to 5 mm using 40 IM7-8552 plies, in a $[0/90]_{10S}$ lay-up. The geometry of the PBP-I actuator is reported in Figure 6.1.

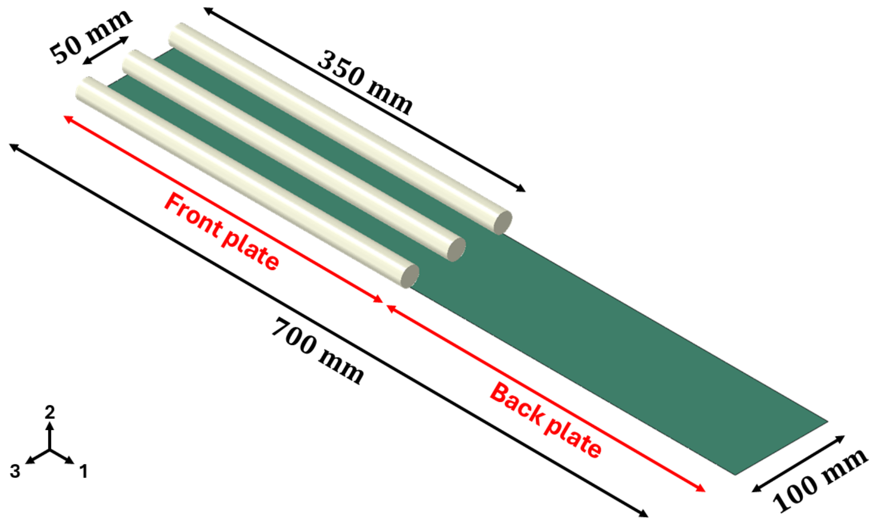

Figure 6.1: Geometry of the PBP-I actuator.

Flap Surfaces: Geometry

The flap surfaces are modeled as rectangular sheets made of a highly flexible rubber, whose material properties match those of commercially available products. Rubber materials have non-linear material properties; however, below 50% elongation the behavior of rubber can be approximated as linear. Since the strain does not overcome this limit, the material is modeled as linear [45]. The material properties used for the flap surfaces is reported in Table 6.2 and are coherent with the values of flexible elastomers [18].

The upper surface is 0.25 mm thick, and its initial length is 633 mm; the stretched length

Material properties	
Upper surface thickness, t_U	0.25 mm
Lower surface thickness, t_L	2 mm
Young Modulus, E	10 MPa
Poisson's Ratio, ν	0.45
Density, ρ	1×10^{-6} kg/mm^3

Table 6.2: Material properties of the flap surfaces.

is 708.6 mm, imposing a 11.9% pre-strain. The lower surface is 2 mm thick, the initial length is 613 mm and the final length is 700.1 mm, the applied pre-strain is 14.3 %. The process to obtain the pre-strain values is thoroughly explained in Section 6.2. In Figure 6.2, the stretched skins are shown in red, while the undeformed skins are overlayed. When the surfaces are stretched, their front edges are vertically aligned and distancing 120 mm from each other. The width matches that of the actuator, at 100 mm. The thickness values were picked from commercially available rubber sheets [21, 44, 46]. The lower skin is responsible for providing most of the compressive force, while the upper skin has the function to provide stability along the vertical axis.

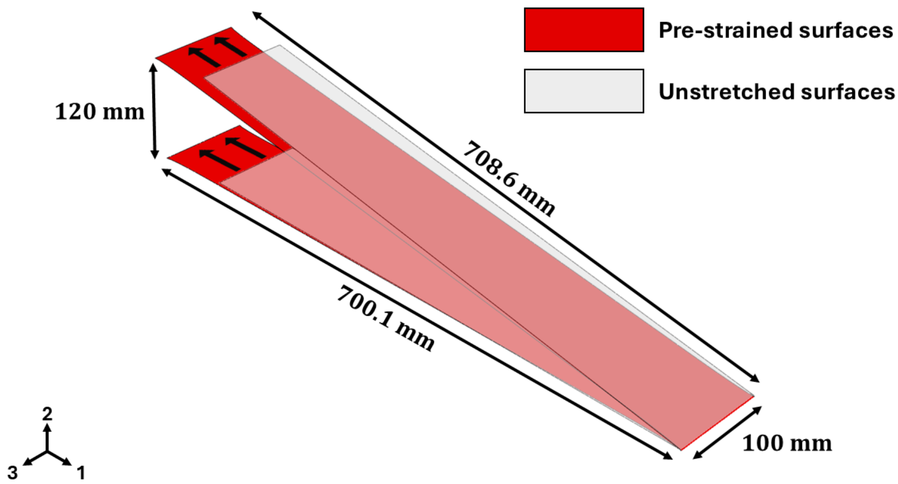

Figure 6.2: Geometry of the pre-stretched flap surfaces.

6.1.2. Adaptive Flap: Geometry

The flap is obtained by connecting the rubber skins and the actuator at the trailing edge. After the pre-stretch, the front edges of the flap surfaces are vertically aligned with the root of the PBP-I actuator. The flap is asymmetric and the camber angle at the trailing edge is 4.9°; however, by rotating the configuration around Direction 3 it's possible to obtain any camber angle desired. This trailing edge angle is obtained by placing the upper and lower surfaces front edges 110 mm above and 10 mm below the actuator root, respectively. The tubes on the actuator are facing the upper surface. The actuator is put closer to the lower skin to maximize the space available to the tubes before they touch the upper skin during the deployment of the flap. The features described are represented in Figure 6.3, which shows the side view of the flap.

The flap functions between $p_\phi = 0.10$ MPa and $p_\phi = 0.50$ MPa. The tubes are never totally deflated to maintain their stiffening effect on the thinner front plate even when the flap is deactivated. The actuator is compressed by the pre-stretched flap surfaces. When the tubes are inflated, the panel is further compressed causing the actuator to buckle.

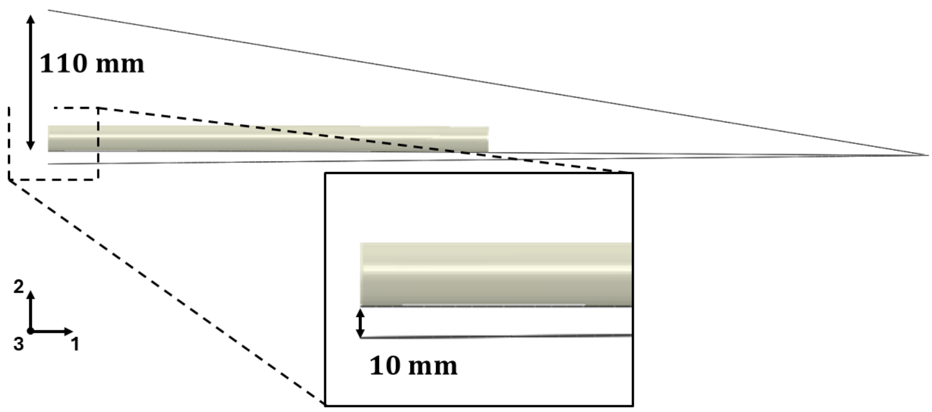

Figure 6.3: Side view of the flap model.

Adaptive Flap: Finite Element Model

The tubes and the front plate of the actuator panel are connected with a TIE constraint. The extremities of the tubes are coupled with their own reference points and behave as rigid surfaces, as reported in Section 2.3. The actuator is constrained on one edge with an encastre boundary condition, which is applied both on the panel edge and on the tubes' extremities. After the pre-stretch, the front edges of the rubber surfaces are constrained with an encastre boundary condition as well. This boundary condition does not affect the ability to rotate of the flap surfaces since they are made of a highly flexible material. The opposite edges are both connected together and with the free edge of the actuator with a TIE constraint. The tubes use M3D4R membrane elements and the mesh size is $l_{el} = 1$ mm; the plate and the flap surfaces use S4R shell elements with a mesh size of $l_{el} = 5$ mm. Figure 6.4 shows the finite element model of the flap after the pre-stretch, the boundary conditions and the tie constraint. The pressurization of the tube is provided with the Fluid Cavity Interaction.

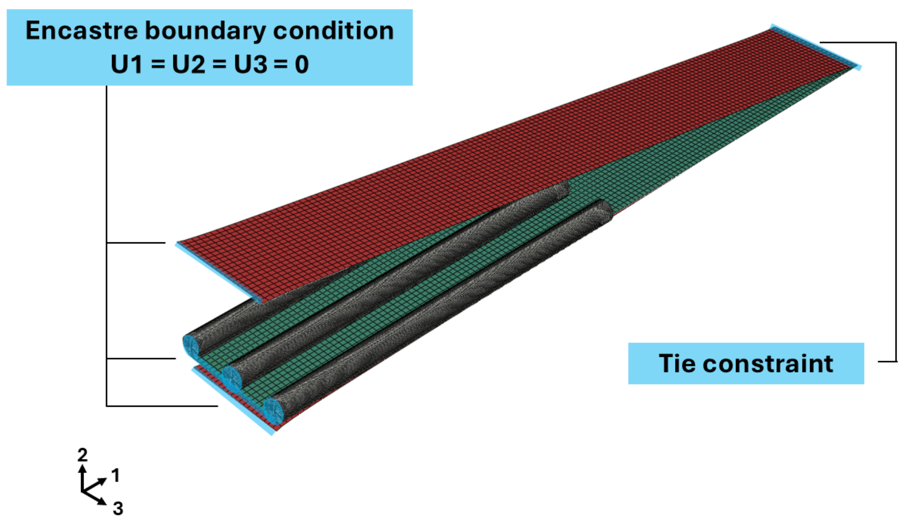

Figure 6.4: FE model of the flap.

The analysis is divided into four steps: Step 1 and Step 2 are preliminary steps and are necessary to inflate the tubes and stretch the skins. During Step 1 the actuator is inflated to $p_\phi = 0.10$ MPa. This step employs an Implicit Dynamic Quasi Static analysis. The remaining steps employ non-linear static analysis to avoid oscillations in the flap. In Step 2 the skins are stretched to impose a compressive load on the actuator. The vertical coordinates of the front edges of the surfaces are kept constant during the stretching process, while are horizontally translated into place. The pre-stretch is obtained by applying a 75 mm horizontal displacement on the upper surface, and a 87 mm horizontal displacement on the lower surface, as shown in Figure 6.5. After the pre-stretch, the front edges of the skins are constrained in every degree of freedom.

Step 3 and 4 are the actual testing steps: in Step 3 the beam is inflated to $p_\phi = 0.50$ MPa and in Step 4 is deflated back to $p_\phi = 0.10$ MPa. The only controlled variable in Step 3

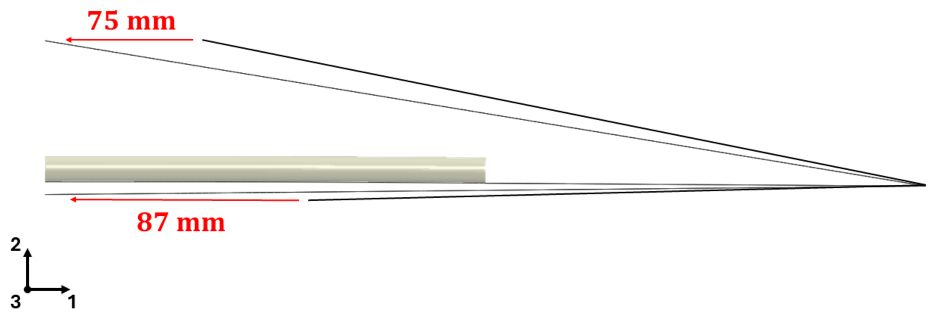

Figure 6.5: Skin pre-stretch.

and 4 is the internal pressure of the tubes. The goal is to verify that the response of the flap is the same both when it's deployed and retracted. The output value of interest is the relation between the inflation pressure and the trailing edge angle.

6.2. Semi-Analytical Model for Pre-Strain Prediction

The pre-stretch of the upper and lower surfaces is key to guarantee the correct functioning of the flap: over-stretching the skins would crush the actuator, taking away any control influence; on the other hand, under-stretching the skin would not provide enough pre-compression to even activate the flap in the first place. The compression generated by the skin must also be balanced, since any excessive force in one of the two directions would create an uncontrollable response.

For this reason, a semi-analytical model is developed to find the pre-stretch of the upper and lower flap surfaces that would guarantee the correct functioning of the flap. To do so, the equilibrium of the forces on the trailing edge at the initial and final configuration is computed. The initial configuration corresponds with the deactivated flap, which maintains a 0° trailing edge angle. The final configuration is the activated flap, the goal is to obtain a 10° trailing edge angle.

The forces in the equilibrium equations are obtained through the finite element analyses of the single components of the flap. To model the response of the flap skins, a non-linear finite element analysis of a rubber plate is conducted to obtain the force-strain behavior of the two surfaces. The actuator is tested, in both the initial and final configurations, by constraining the vertical displacement and recording the load response by varying the horizontal position of the trailing edge.

In total, there are four equations to be solved: the horizontal and vertical equilibrium for both configurations. The terms of the equations relative to the initial configuration are referred to with the index i, while those referring to the final configuration with the index f. The total number of variables is also four:

- The initial length of the upper surface $l_{U,0}$ and lower surface $l_{L,0}$.
- The horizontal position of the trailing edge in the initial and final configuration, $x_{TE,i}$ and $x_{TE,f}$.

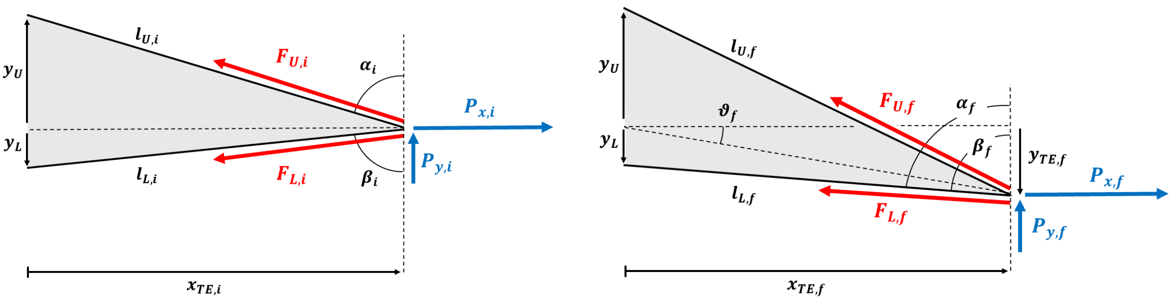

(a) Initial configuration (b) Final configuration

Figure 6.6: Equilibrium on the trailing edge.

Figure 6.6 reports the geometric parameters and the forces employed in the equilibrium equations. The four equilibrium equations obtained from the force distribution on the trailing edges are reported in Equation 6.1:

$$
\begin{cases}
P_{x,i} - F_{U,i}\sin\alpha_i - F_{L,i}\sin\beta_i = 0 \\
P_{y,i} + F_{U,i}\cos\alpha_i - F_{U,i}\cos\beta_i = 0 \\
P_{x,f} - F_{U,f}\sin\alpha_f - F_{L,f}\sin\beta_f = 0 \\
P_{y,f} + F_{U,f}\cos\alpha_f + F_{U,f}\cos\beta_f = 0
\end{cases}
\tag{6.1}
$$

Before solving the system, it is necessary to assess the dependency of each term on the variables.

Geometric terms

The vertical position of the front edges of the flap surfaces is fixed:

$$y_U = 110 \text{ mm}$$
$$y_L = 10 \text{ mm}$$

The vertical displacement of the trailing edge is also a fixed parameter. In the initial configuration $y_{TE,i} = 0$ mm, since the trailing edge angle is set at 0°. The final vertical displacement of the trailing edge can be obtained from the final trailing edge angle, set at $\theta_{TE,f} = 10°$:

$$y_{TE,f} = 700 \text{ mm} \times \sin\theta_{TE,f} = 123 \text{ mm}$$

Theoretically, the value of $y_{TE,f}$ would be dependent on $x_{TE,f}$; however, since the displacements along the horizontal direction is not large enough to produce significant variations of $\theta_{TE,f}$, the value of 700 mm is used. This value represents the horizontal length of the flap when the tubes are not inflated and the skins are not stretched.

The angles α and β are function of the horizontal position of the trailing edge and can be defined as:

$$\alpha_i(x_{TE,i}) = \arctan\left(\frac{x_{TE,i}}{y_U}\right)$$
$$\beta_i(x_{TE,i}) = \arctan\left(\frac{x_{TE,i}}{y_L}\right)$$
$$\alpha_f(x_{TE,f}) = \arctan\left(\frac{x_{TE,f}}{y_U + y_{TE,f}}\right)$$
$$\beta_f(x_{TE,f}) = \arctan\left(\frac{x_{TE,f}}{y_{TE,f} - y_L}\right)$$

The length of the surfaces after the pre-stretch is represented by the variables $l_{U,i}$, $l_{L,i}$, $l_{U,f}$ and $l_{L,f}$. These values are also dependent on $x_{TE,i}$ and $x_{TE,f}$:

$$l_{U,i}(x_{TE,i}) = \frac{x_{TE,i}}{\sin\alpha_i(x_{TE,i})}$$
$$l_{L,i}(x_{TE,i}) = \frac{x_{TE,i}}{\sin\beta_i(x_{TE,i})}$$
$$l_{U,f}(x_{TE,f}) = \frac{x_{TE,f}}{\sin\alpha_f(x_{TE,f})}$$
$$l_{L,f}(x_{TE,f}) = \frac{x_{TE,f}}{\sin\beta_f(x_{TE,f})}$$

Forces generated by the flap surfaces

The loads applied by the rubber surfaces on the trailing edge can be found by studying the non-linear response of a rubber plate to an axial load. The rubber plate is stretched up to 50% strain. The analysis is conducted with one end totally constrained, while the other is constrained in every direction except the axial one. The deformed shape of the rubber plate is shown in Figure 6.7.

Figure 6.7: Skin test.

The force obtained is then normalized with respect to the width and the thickness of the tested plate. The force-strain relationship, shown in Figure 6.8, of the upper and lower surfaces is defined by multiplying the values of the normalized force obtained in the axial test with the thickness and width values of each skin.

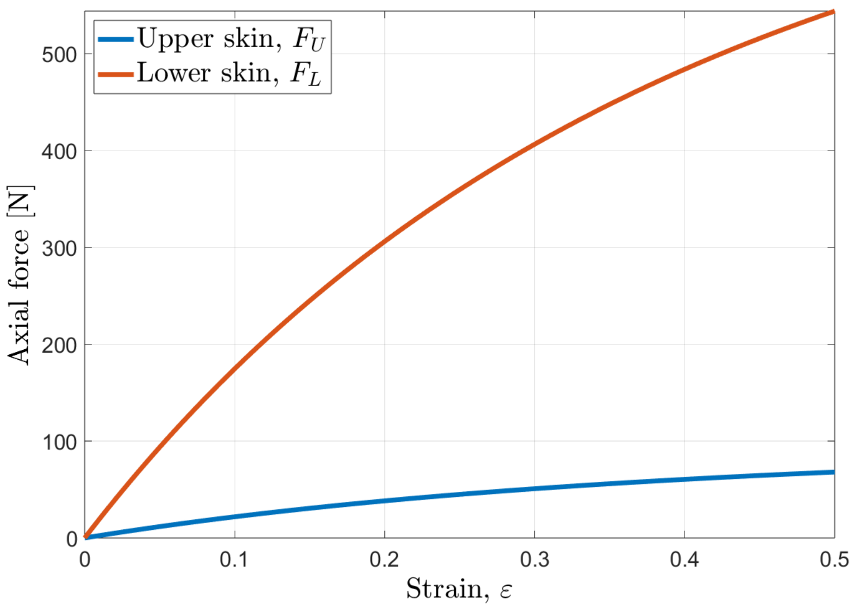

Figure 6.8: Upper and lower surface force-strain relation.

The strain of the flap surfaces is function both of the initial length values $l_{U,0}$ and $l_{L,0}$, and the stretched length values $l_{U,i}$, $l_{L,i}$, $l_{U,f}$ and $l_{L,f}$. These last terms are function of the primary variables $x_{TE,i}$ and $x_{TE,f}$, therefore the strain values are function both of the horizontal coordinate of the trailing edge and the initial length of the surfaces:

$$\begin{aligned}
\varepsilon_{U,i}(x_{TE,i}, l_{U,0}) &= \frac{l_{U,i} - l_{U,0}}{l_{U,0}} \\
\varepsilon_{L,i}(x_{TE,i}, l_{L,0}) &= \frac{l_{L,i} - l_{L,0}}{l_{L,0}} \\
\varepsilon_{U,f}(x_{TE,f}, l_{U,0}) &= \frac{l_{U,f} - l_{U,0}}{l_{U,0}} \\
\varepsilon_{L,f}(x_{TE,f}, l_{L,0}) &= \frac{l_{L,f} - l_{L,0}}{l_{L,0}}
\end{aligned}$$

Consequentially, this dependency is transferred to the forces imposed by the flap surfaces on the trailing edge:

$$\begin{aligned}
F_{U,i} &= F_{U,i}(x_{TE,i}, l_{U,0}) \\
F_{L,i} &= F_{L,i}(x_{TE,i}, l_{L,0}) \\
F_{U,f} &= F_{U,f}(x_{TE,f}, l_{U,0}) \\
F_{L,f} &= F_{L,f}(x_{TE,f}, l_{L,0})
\end{aligned}$$

Forces generated by the actuator

The values of the forces generated by the actuator are obtained from two numerical analyses conducted on the actuator alone. The two analyses are conducted by constraining vertically the trailing edge and studying the load response of the actuator as the horizontal coordinate changes. The horizontal position of the trailing edge cannot be known a priori, since it's a result of the mutual interaction of the actuator and the flap surfaces. For this reason, the load response of the actuator with respect to x_{TE} must be studied. As could be expected, the forces generated by the actuator are dependent only on the trailing edge horizontal position. The setup of the actuator analyses is shown in Figure 6.9.

The first analysis constrains the trailing edge at $y_{TE,i} = 0$ mm. Firstly, the tubes on the actuator are inflated at $p_\phi = 0.10$ MPa; during the inflation $x_{TE,i}$ is kept unconstrained and reaches the unloaded equilibrium position. The trailing edge is then compressed along the horizontal direction and the load response is recorded and shown in Figure 6.10.

The second analysis constrains the trailing edge at $y_{TE,f} = 123$ mm and is representative of the fully deployed flap. The tubes on the actuator are inflated at $p_\phi = 0.50$ MPa, then the actuator is deflected to $y_{TE,f} = 123$ mm. The horizontal position of the trailing edge is kept unconstrained and reaches the unloaded equilibrium position at the end of the

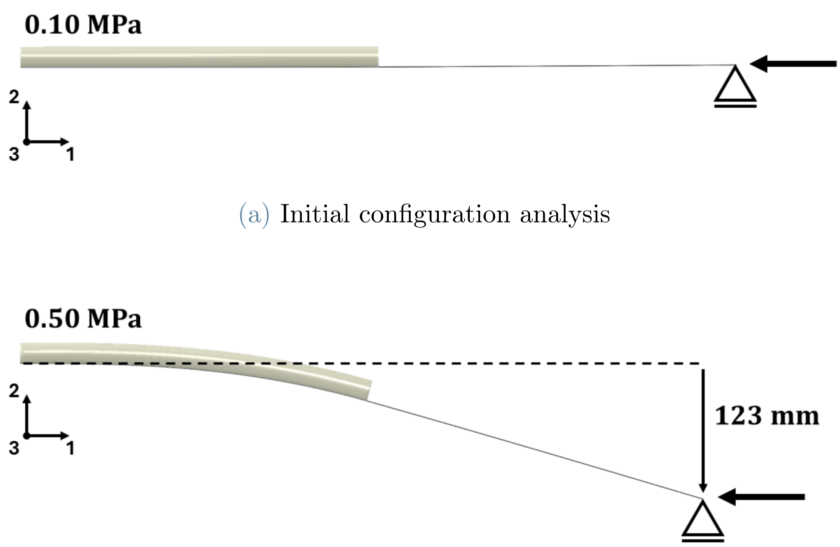

(a) Initial configuration analysis

(b) Final configuration analysis

Figure 6.9: Actuator analyses setup.

deflection. The trailing edge is then compressed along the horizontal direction and the load response is recorded and shown in Figure 6.11.

By using these relationships, the force imposed by the actuator on the trailing edge can be written as function of x_{TE}:

$$
\begin{aligned}
P_{x,i} &= P_{x,i}(x_{TE,i}) \\
P_{y,i} &= P_{y,i}(x_{TE,i}) \\
P_{x,f} &= P_{x,f}(x_{TE,f}) \\
P_{y,f} &= P_{y,f}(x_{TE,f})
\end{aligned}
$$

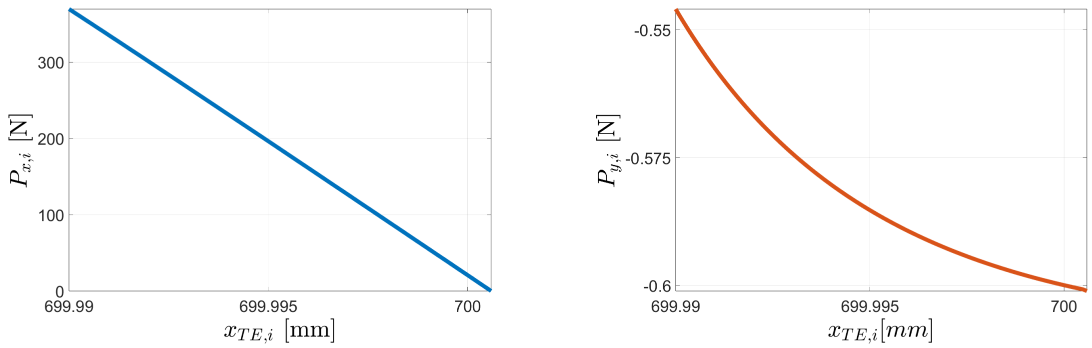

Figure 6.10: Actuator forces for the deactivated flap.

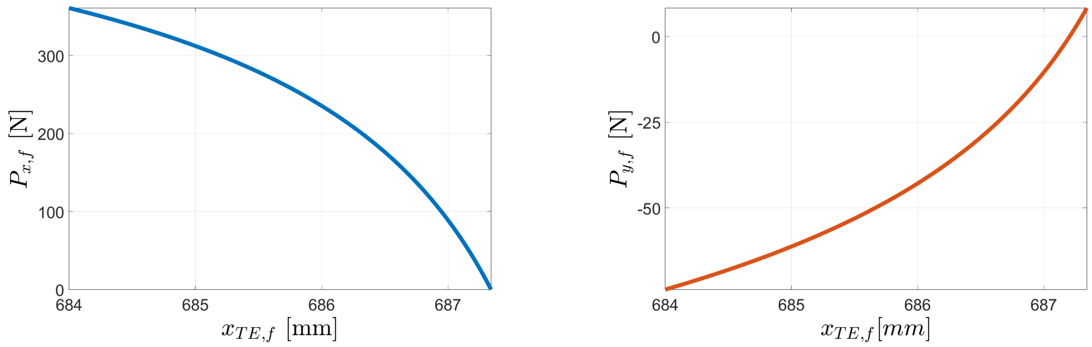

Figure 6.11: Actuator forces for the deployed flap.

Solution of the equilibrium and pre-strain values

Once the dependency of each term of Equation 6.1 is defined, it's possible to finally solve the system shown in Equation 6.2.

$$\begin{cases} P_{x,i}(x_{TE,i}) - F_{U,i}(x_{TE,i}, l_{U,0}) \sin \alpha_i(x_{TE,i}) - F_{L,i}(x_{TE,i}, l_{U,0}) \sin \beta_i(x_{TE,i}) = 0 \\ P_{y,i}(x_{TE,i}) + F_{U,i}(x_{TE,i}, l_{U,0}) \cos \alpha_i(x_{TE,i}) - F_{U,i}(x_{TE,i}, l_{U,0}) \cos \beta_i(x_{TE,i}) = 0 \\ P_{x,f}(x_{TE,f}) - F_{U,f}(x_{TE,f}, l_{U,0}) \sin \alpha_f(x_{TE,f}) - F_{L,f}(x_{TE,f}, l_{U,0}) \sin \beta_f(x_{TE,f}) = 0 \\ P_{y,f}(x_{TE,f}) + F_{U,f}(x_{TE,f}, l_{U,0}) \cos \alpha_f(x_{TE,f}) + F_{U,f}(x_{TE,f}, l_{U,0}) \cos \beta_f(x_{TE,f}) = 0 \end{cases} \tag{6.2}$$

Due to the non-linearity of the system and the force values obtained from finite element computations, the system must be solved numerically. The unstretched lengths of the upper and lower flap surfaces are reported in Equation 6.3 and 6.4:

$$l_{U,0} = 613 \text{ mm} \tag{6.3}$$

$$l_{L,0} = 633 \text{ mm} \tag{6.4}$$

The pre-strain applied on the upper and lower surface, corresponding to the strain in the initial configuration, can be therefore obtained:

$$\varepsilon_{U,i} = 0.119 \tag{6.5}$$

$$\varepsilon_{L,i} = 0.143 \tag{6.6}$$

6.3. Adaptive Flap with PBP-I Actuator: Results

The results from the flap analysis confirm the semi-analytical model. At $p_\phi = 0.10$MPa, the trailing edge angle is 0.27° with a vertical tip displacement of $y_{TE,i} = 3.3$ mm; when the flap is fully deployed the trailing edge angle is 9.95° and $y_{TE,i} = 122.8$ mm. The behavior of the flap with respect to the inflation pressure of the tubes is reported in Figure 6.12. The flap follows the same trend during both deployment and retraction. The dependence of the trailing edge angle on the inflation pressure can be linearly interpolated:

$$\theta_{TE} = 24.19 \frac{\text{deg}}{\text{MPa}} \times p_\phi - 1.78 \, \text{deg}, \qquad p_\phi \in [0.10 \text{ MPa}, 0.50 \text{ MPa}] \tag{6.7}$$

The behavior of the flap could be studied in a wider range of configurations: the flap could be deflected upwards by reducing the pressure further than 0.10 MPa, or obtain larger trailing edge angles by varying the pre-stretch of the rubber surfaces. However, they may lead to internal contact between the actuator and the flap surfaces, producing unpredictable behaviors. For this reason, the behavior of the flap was investigated in a safe range, where the actuator is always distanced from the rubber surfaces.

Figure 6.13 shows the deformed shape of the flap at different levels of inflation pressure. The main deformation of the actuator is located in the front section of plate. The rear plate is maintained undeformed, as it was designed to behave.

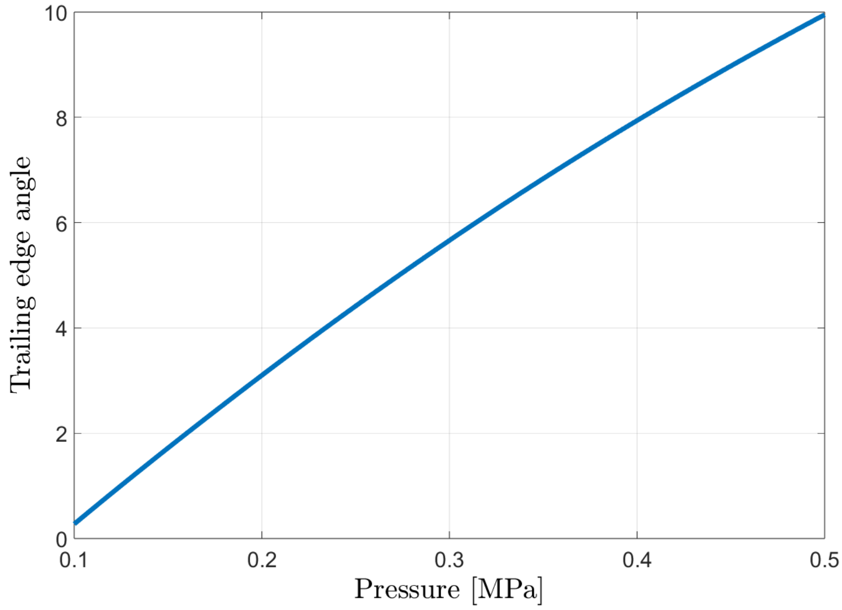

Figure 6.12: Trailing edge angle with respect to pressure.

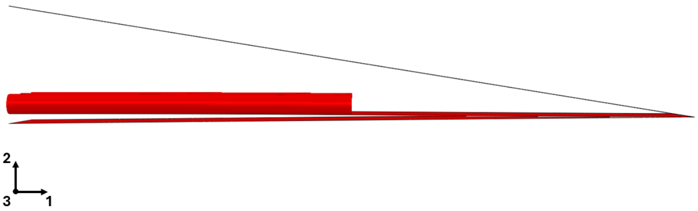

(a) $p_\phi = 0.10$ MPa

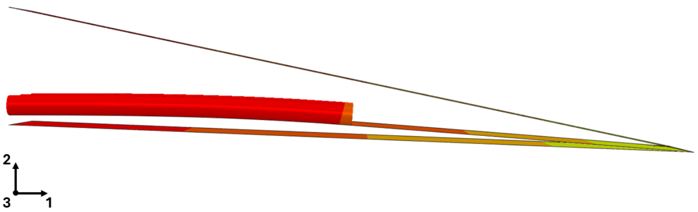

(b) $p_\phi = 0.20$ MPa

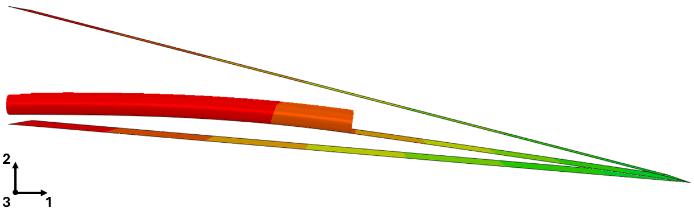

(c) $p_\phi = 0.30$ MPa

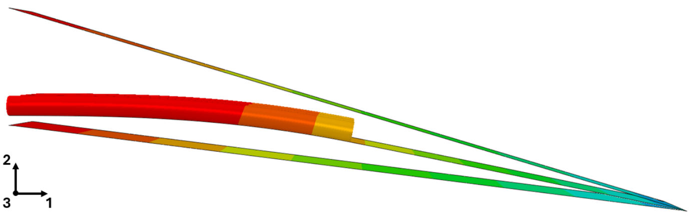

(d) $p_\phi = 0.40$ MPa

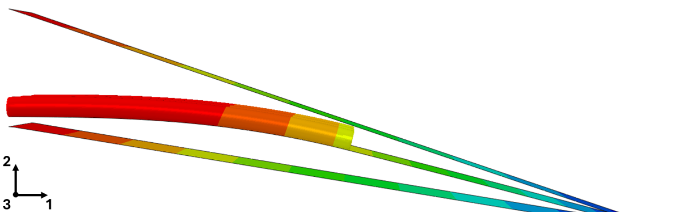

(e) $p_\phi = 0.50$ MPa

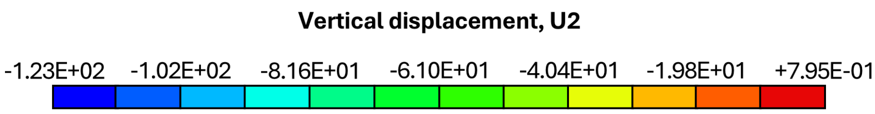

Figure 6.13: Flap deformation.

7 | Conclusions and Future Developments

The scope of this work was to provide a preliminary study on the effectiveness of inflatable tubes as reinforcing elements of panels. An inflatable tube was modeled and validated first. By employing the fluid cavity interaction provided by ABAQUS to achieve the pressurization, the tube was inflated, tested and compared to the reference analytical formulation [16]. The results of the validation were in agreement with the reference values.

The inflatable tube was then implemented in a composite panel in different configurations which varied in the number of tubes, either one or three, and the orientation angle of the tubes, either 0° or 45° with respect to the center line. The study employed finite element computations to assess the load response of the panel with inflatable elements to compression and shear. The inflatable stiffened panels were tested at three inflation pressures p_ϕ: 0.05 MPa, 0.10 MPa, 0.20 MPa. The compression and shear load cases included both possible load directions, in order to assess the all-around behavior of the stiffened panel: the 0° configuration was tested also at 90° and the 45° configuration was tested at -45°. The influence of the pressure on the load response was evident: a higher inflation pressure increased the stiffness of the structure. Apart from the configurations where the tubes layout was ineffective to counteract the applied load, the stiffness of the panel increased with the internal pressure and the number of the tubes.

The best compressive structural response was provided by the three-tube configuration at 0°, inflated at $p_\phi = 0.20$ MPa. At the end of the loading step, the load response of the panel was $F_C = 5026$ N, providing a 1900 N increment with respect to the panel without tubes. However, the best relative performance of the inflatable stiffened panel was found at the beginning of the loading step, around $U_C = 0.1$ mm: although the magnitude of the forces was lower, the inflatable stiffened panel delivered a 125.4% increase in load bearing capabilities. The same configuration also performed well under shear, providing a 50% increase in the load response. On the other hand, when compressed at 90°, the performance of the panel dropped by 27.6%.

The 45° layout provided mediocre results in compression and a small increase in load bearing capabilities was recorded. When the shear displacement was applied, the tubes did not provide any improvement to the load response. This was due to the shear load being aligned with the inflatable elements. However, the same load applied in the opposite direction provided the best shear response, with an increase in stiffness of roughly 60%.

The control of the load response was successfully tested by modulating the pressure inside the tubes. The panel was able to switch between different load trends by adjusting the inflation pressure. The buckling shape could be controlled as well, but the range of motion was small, being no larger than 5 mm in the best-case scenario.

A possible approach to morphing application was presented by developing a numerical model of an adaptive flap controlled by the pressure inside inflatable tubes. Three tubes were implemented on a Post-Buckled Precompressed Inflatable (PBP-I) actuator, which can control the trailing edge angle of the flap by modulating the inflation pressure. The actuator is compressed by the pre-strained rubber flap surfaces and buckles when the tubes are inflated. The main challenge was the prediction of the pre-stretch of the flap surfaces, since overestimating or underestimating this value could jeopardize the functioning of the flap itself. For this reason, a semi-analytical model was developed. The goal values were a 0° trailing edge angle at $p_\phi = 0.10$ MPa and 10° at $p_\phi = 0.50$ MPa. The numerical analysis on the flap with the pre-strain obtained from the semi-analytical model provided a 0.27° trailing edge angle at $p_\phi = 0.10$ MPa and a 9.95° angle at $p_\phi = 0.50$ MPa. This model provided a clear example of the potential of inflatable tubes in morphing applications and future research on this topic is necessary to fully exploit their beneficial properties.

Bibliography

[1] D. Moorhouse, B. Sanders, M. von Spakovsky, and J. Butt. Benefits and design challenges of adaptive structures for morphing aircraft. *The Aeronautical Journal*, 3012:157–162, 2006.

[2] S. Barbarino, O. Bilgen, R. M. Ajaj, M. I. Friswell, and D. J. Inman. A review of morphing aircraft. *Journal of Intelligent Material Systems and Structures*, 22:823–877, 2011.

[3] H.F. Parker. The parker variable camber wing. *National Advisory Committee for Aeronautics*, 77, 1920.

[4] R.K. Page. Aircraft with variable-sweep wings: A discussion outlining the advantages and disadvantages of variable-sweep aircraft and the principal features of three possible types: a trainer, a strike fighter and a supersonic transport. *Aircraft Engineering*, 37:295–299, 1920.

[5] Master Sgt. Robert W. Valenca. U.s. air force photo, 2004. `https://en.wikipedia.org/wiki/Rockwell_B-1_Lancer#/media/File:A_B-1_Lancer_performs_a_fly-by_during_a_firepower_demonstration.jpg` [Accessed: 2026-02-20].

[6] S. Ameduri and A. Concilio. Morphing wings review: aims, challenges, and current open issues of a technology. *Journal of Mechanical Engineering Science*, 237(18):4112–4130, 2023.

[7] M. N. Mowla, D. Asadi, T. Durhasan, and M. Amoozgar J. R. Jafari. Recent advancements in morphing applications: Architecture, artificial intelligence integration, challenges, and future trends - a comprehensive survey. *Aerospace Science and Technology*, 161, 2025.

[8] J. Sun, Q. Guan, Y. Liu, and J. Leng. Morphing aircraft based on smart materials and structures: A state-of-the-art review. *Journal of Intelligent Material Systems and Structures*, 27(17):2289–2312, 2016.

[9] S. Sathyamoorthy, S. Raja, and A. J. Stanley. Piezoelectric based adaptive wing for flow control. *Journal of Aerospace Sciences and Technologies*, 58(4):305–312, 2006.

[10] T. Yokozeki and A. Sugiura. Piezoelectric based adaptive wing for flow control. *Journal of Aircraft*, 51:1023–1029, 2014.

[11] A. C. Henry, G. Molinari, J.R. Rivas-Padilla, and A. F. Arrieta. Smart morphing wing: Optimization of distributed piezoelectric actuation. *AIAA Journal*, 57(6):2384–2393, 2019.

[12] A. De Gasperi. Study on the actuation aspects for a morphing aileron using an energy–based design approach. *Actuators*, 185(11), 2022.

[13] X. Li, L. Sun, Y. Pan, and X. Guo. Honeycomb structure filling morphing wing trailing edge: Design strategy, deformation feedback, and active control. *Programmable Materials*, 2(2):1–14, 2024.

[14] C. Wielgosz and J.-C. Thomas. Deflections of inflatable fabric panels at high pressure. *Thin-Walled Structures*, 40:523–536, 2002.

[15] J.-C. Thomas and C. Wielgosz. Deflections of highly inflated fabric tubes. *Thin-Walled Structures*, 42:1049–1066, 2004.

[16] A. Le Van and C. Wielgosz. Bending and buckling of inflatable beams: Some new theoretical results. *Thin-Walled Structures*, 43:1166–1187, 2005.

[17] C. Wielgosz, E. Leflaive, J.-F. Dubé, and J.-C. Thomas. Behaviour of inflated fabric beams at medium pressures. In *Proceedings of the Twelve International Conference on Composite Material. I.C.C.M. 12*, 1999.

[18] N. Mandlekar, M. Joshi, and B. S. Butola. A review on specialty elastomers based potential inflatable structures and applications. *Advanced Industrial and Engineering Polymer Research*, 5:33–45, 2022.

[19] J.-C Thomas and A. Bloch. Non linear behaviour of an inflatable beam and limit states. *Procedia Engineering*, 155:398–406, 2016.

[20] C. G. Malm, W. G. Davids, M. L. Peterson, and A. W. Turner. Experimental characterization and finite element analysis of inflated fabric beams. *Construction and Building Materials*, 23:2027–2034, 2009.

[21] D. A. Litteken. Inflatable technology: using flexible materials to make large structures. *Proc. of SPIE*, 10966(1096603), 2019.

[22] S.L. Veldman and C. A. J. R. Vermeeren. Inflatable structures in aerospace engineering - an overview. In *European Conference on Spacecraft Structures, Materials and Mechanical Testin g, Proceedings of the conference held 29 November - 1 December, 2000 at ESTEC, Noordwijk, The Netherlands*, 2000.

[23] A. Babuscia, B. Corbin, M. Knapp, R. Jensen-Clem, M. Van de Loo, and S. Seager. Inflatable antenna for cubesats: Motivation for development and antenna design. *Acta Astronautica*, 91:322–332, 2013.

[24] NASA, 1996. `https://en.wikipedia.org/wiki/Inflatable_Antenna_Experiment#/media/File:Inflatable_Antenna_Experiment.jpg` [Accessed: 2026-02-20].

[25] Boxuan Xu, Haishen Wang, Wu Jiang, Xianzhi Zeng, and Peng Pan. Study on axial compression behavior of thin-walled pressurized steel pipe column. *Engineering Structures*, 351(122038), 2026.

[26] J. M. Rotter. Elephant's foot buckling in pressurized cylindrical shells. *Stahlbau*, 75:742–747, 2006.

[27] R. Vos and R. Barrett. Pressure adaptive honeycomb: A novel concept for morphing aircraft structures. In *27th Congress of International Council of the Aeronautical Sciences*, 2010.

[28] M. Cremaschi. Investigation of a variable pressure controlled sandwich panel. Master's thesis, Politecnico di Milano, 2023.

[29] Chuen-Yuan Chia. *Nonlinear Analysis of Plates.* McGraw-Hill International Book Company, 1980.

[30] L. Li and P. Bettess. Buckling of stiffened plates and design of stiffeners. *Internation Journal of Pressure Vessels and Piping*, 74:177–187, 1997.

[31] C. Bisagni. Numerical analysis and experimental correlation of composite shell buckling and post-buckling. *Composites: Part B*, 31:655–667, 2000.

[32] C. Bisagni and Potito Cordisco. Post-buckling and collapse experiments of stiffened composite cylindrical shells subjected to axial loading and torque. *Composite Structures*, 73:138–149, 2000.

[33] R. D. Young, C. A. Rose, and J. H. Starnes Jr. Skin, stringer, and fastener loads in buckled fuselage panels. Technical Report 1326, AIAA, 2001.

[34] NeedsGlasses, 2000. `https://en.wikipedia.org/wiki/Buckling#/media/File:B52-buckling.jpg` [Accessed: 2026-02-20].

[35] S. R Thompson and J. Loughlan. The control of the post-buckling response in thin composite plates using smart technology. *Thin-Walled Structures*, 36:231–263, 2000.

[36] R. Vos, R. Barrett, R. de Breuker, and P. Tiso. Post-buckled precompressed elements: a new class of control actuators for morphing wing uavs. *Smart Material Structures*, 16:919–926, 2007.

[37] S. Daynes, S.J. Nall, P.M. Weaver, K.D. Potter, P. Margaris, and P.H. Mellor. On a bistable flap for an airfoil. In *50th AIAA/ASME/ASCE/AHS/ASC Structures, Structural Dynamics, and Materials Conference*, 2013, 2009.

[38] J. Zhang and C. Bisagni. Buckling-driven mechanisms for twisting control in adaptive composite wings. *Aerospace Science and Technology*, 118(107006), 2021.

[39] SIMULIA. Abaqus analysis user's manual, 2016.

[40] H. M. Chandima Chathuranga Somarathna, Sudharshan N. Raman, Khairiah Haji Badri, , Azrul A. Mutalib, Damith Mohotti, and Sri Devi Ravana. Quasi-static behavior of palm-based elastomeric polyurethane: For strengthening application of structures under impulsive loadings. *Polymers*, 8(202), 2016.

[41] Changqing Fang, Rong Yang, Zisen Zhang, Xing Zhou, Wanqing Lei, Youliang Cheng, Wei Zhanga, and Dong Wangab. Effect of multi-walled carbon nanotubes on the physical properties and crystallisation of recycled pet/tpu composites. *RSC Advances*, 8:8920–8928, 2018.

[42] Alan Neville Gent. *The Pneumatic Tire*. National Highway Traffic Safety Administration, 2006.

[43] Hani Aziz Ameen. Mechanical properties of composite material using natural rubber with epoxy resin. *Eng. & Tech*, 26(2), 2008.

[44] Andrea Ruggeri. Selezione dei materiali per un robot gonfiabile per applicazioni aerospaziali: criteri e metodologie. Master's thesis, Politecnico di Torino, 2021.

[45] Zengrui Yuan, Mu-Qing Niu, Hongtu Ma, Tao Gao, Jian Zang, Yewei Zhang, and LiQun Chen. Predicting mechanical behaviors of rubber materials with artificial neural networks. *International Journal of Mechanical Sciences*, 75:742–747, 2006.

[46] K.L. Apedo, S. Ronel, E. Jacquelin, A. Bennani, and M. Massenzio. Nonlinear finite

element analysis of inflatable beams made from orthotropic woven fabric. *International Journal of Solids and Structures*, 47:2017–2033, 2010.

List of Figures

List of Tables

List of Symbols

Variable	Description	SI unit
$\boldsymbol{A}$	Amplitude of the buckle	$\times$
$\boldsymbol{E}$	Young's modulus	MPa
$\boldsymbol{F}$	Applied force in tube analytical formulation	N
$\boldsymbol{F}_C$	Compressive load	N
$\boldsymbol{F}_L$	Lower surface force	N
$\boldsymbol{F}_S$	Shear load	N
$\boldsymbol{F}_U$	Upper surface force	N
$\boldsymbol{G}$	Shear modulus	MPa
$\boldsymbol{h}$	Inflatable tube thickness (deflated)	mm
$\boldsymbol{I}_\phi$	Inflatable tube second moment of area (inflated)	mm^4
$\boldsymbol{k}$	Shear correction factor (deflated)	$\times$
$\boldsymbol{l}$	Inflatable tube length (deflated)	mm
$\boldsymbol{l}_\phi$	Inflatable tube length (inflated)	mm
$\boldsymbol{l}_{L,0}$	Lower surface unstretched length	mm
$\boldsymbol{l}_L$	Lower surface length	mm
$\boldsymbol{l}_{U,0}$	Upper surface unstretched length	mm
$\boldsymbol{l}_U$	Upper surface length	mm
$\boldsymbol{L}$	Panel length	mm
$\boldsymbol{m}$	Number of half-waves	$\times$
$\boldsymbol{N_x}$	Internal axial load	N/m
$\boldsymbol{\hat{N}_x}$	Applied axial load	N/m
$\boldsymbol{p}_\phi$	Inflation pressure	MPa
$\boldsymbol{P}$	Axial force generated by the pressurization	N
$\boldsymbol{P}_x$	Actuator horizontal force	N
$\boldsymbol{P}_y$	Actuator vertical force	N

$\boldsymbol{r}$	Inflatable tube radius (deflated)	mm
$\boldsymbol{r}_\phi$	Inflatable tube radius (inflated)	mm
$\boldsymbol{S}_\phi$	Inflatable tube cross section (inflated)	mm^2
$\boldsymbol{t}$	Panel thickness	mm
$\boldsymbol{t}_L$	Lower surface thickness	mm
$\boldsymbol{t}_{Ply}$	Ply thickness	mm
$\boldsymbol{t}_U$	Upper surface thickness	mm
$\boldsymbol{U}_C$	Applied compressive displacement	mm
$\boldsymbol{U}_S$	Applied shear displacement	mm
$\boldsymbol{V}$	Inflatable tube vertical displacement	mm
$\boldsymbol{W}$	Panel width	mm
$\boldsymbol{x}$	Generic horizontal coordinate	m
$\boldsymbol{y}$	Generic vertical coordinate	m
$\boldsymbol{x}_{TE}$	Trailing edge horizontal coordinate	mm
$\boldsymbol{y}_{TE}$	Trailing edge vertical coordinate	mm
$\boldsymbol{\alpha}$	Upper surface angle	deg
$\boldsymbol{\beta}$	Lower surface angle	deg
$\boldsymbol{\varepsilon}_U$	Upper surface strain	$\times$
$\boldsymbol{\varepsilon}_L$	Lower surface strain	$\times$
$\boldsymbol{\nu}$	Poisson ratio	$\times$
$\boldsymbol{\rho}$	Density	kg/mm^3
$\boldsymbol{\theta}$	Inflatable tube cross section angle	rad
$\boldsymbol{\theta_{TE}}$	Trailing edge angle	deg

Acknowledgements

This thesis is part of the NABUCCO project: "New Adaptive and BUCKling-driven COmposite aerospace structures". NABUCCO project is funded by the European Union (ERC Advanced Grant, project number 101053309). Views and opinions expressed are however those of the authors only and do not necessarily reflect those of the European Union or the European Research Council Executive Agency. Neither the European Union nor the granting authority can be held responsible for them.

Vorrei ringraziare la mia relatrice, la Professoressa Chiara Bisagni, per aver avuto fiducia in me e per avermi dato la possibilità di realizzare questa tesi, per la sua conoscenza, disponibilità e pazienza. Un sentito ringraziamento anche al Professor Antonio Raimondo, che mi ha affiancato durante lo sviluppo ed è sempre stato disponibile a risolvere ogni mio dubbio.

Ringrazio la mia famiglia, che mi ha spronato a seguire la mia strada e mi ha supportato in ogni mia scelta. Senza di voi non sarei arrivato fin qui.

Vorrei ringraziare anche tutti coloro che, in un modo o nell'altro, hanno fatto sì che questo percorso fosse ricco di bei momenti. Un grazie va ad Elia, Tosca, Luca e Simo: dalle superiori fino ad oggi siete sempre stati al mio fianco e, negli ultimi anni, ho condiviso con voi ogni momento di gioia e fatica. Ringrazio i miei compagni di corso Momo e Madda, unici sopravvissuti alla scrematura fatta dal tempo. Vi stimo sinceramente e sono sicuro che la nostra amicizia continuerà anche fuori le mura universitarie. Grazie al Berna e a tutti coloro con cui ho condiviso avventure alpinistiche; avete reso speciale ogni scalata. Ringrazio Marc e Teo, perché con voi ho imparato ad arrampicare e mi sono appassionato ad una disciplina che tuttora mi riempie di soddisfazione.

Ringrazio infine la mia fidanzata Marta, che da sei anni condivide con me i piaceri e le sfide della vita. Non potevo chiedere una persona migliore al mio fianco. Abbiamo iniziato l'università insieme e la concluderemo insieme; anche se in atenei diversi, il nostro percorso è sempre stato intrecciato da gioie e problemi simili. Abbiamo esplorato il mondo, imparato l'uno dall'altra e siamo diventati adulti. Condividere questi anni con te è stato un regalo prezioso, perché abbiamo costruito insieme le fondamenta del nostro futuro.

Grazie a tutti voi per aver reso indimenticabile questo percorso.